

University of Louisville

ThinkIR: The University of Louisville's Institutional Repository

Electronic Theses and Dissertations

12-2022

Anion alloying of III-V semiconductors for water splitting.

Sonia Juliana Calero-Barney
University of Louisville

Follow this and additional works at: <https://ir.library.louisville.edu/etd>

 Part of the [Other Chemical Engineering Commons](#)

Recommended Citation

Calero-Barney, Sonia Juliana, "Anion alloying of III-V semiconductors for water splitting." (2022). *Electronic Theses and Dissertations*. Paper 3994.

Retrieved from <https://ir.library.louisville.edu/etd/3994>

This Doctoral Dissertation is brought to you for free and open access by ThinkIR: The University of Louisville's Institutional Repository. It has been accepted for inclusion in Electronic Theses and Dissertations by an authorized administrator of ThinkIR: The University of Louisville's Institutional Repository. This title appears here courtesy of the author, who has retained all other copyrights. For more information, please contact thinkir@louisville.edu.

ANION ALLOYING OF III-V SEMICONDUCTORS FOR WATER SPLITTING

By

Sonia Juliana Calero-Barney

Bachelor of Science, Universidad del Valle, Cali, Colombia, 2010

Master of Science, Universidad de los Andes, Bogotá, Colombia, 2014

A Dissertation

Submitted to the Faculty of the

J.B. Speed School of Engineering of the University of Louisville

in Partial Fulfillment of the Requirements

for the Degree of

Doctor of Philosophy in Chemical Engineering

Department of Chemical Engineering

University of Louisville

Louisville, KY 40292

December 2022

ANION ALLOYING OF III-V SEMICONDUCTORS FOR WATER SPLITTING

By

Sonia Juliana Calero-Barney

Bachelor of Science, Universidad del Valle, Cali, Colombia, 2010

Master of Science, Universidad de los Andes, Bogotá, Colombia, 2014

A Dissertation Approved on

November 15, 2022

By the following Dissertation Committee

Dr. Mahendra K. Sunkara, Dissertation Director

Dr. Thomas Starr

Dr. Thad Druffel

Dr. Gautam Gupta

DEDICATION

To my beloved parents Carmen Elvira Barney Medina and Diego German Calero Llanes,
every good thing within me comes from you.

Also, to Shervin Golgiri for his invaluable support throughout these last few years.

ACKNOWLEDGEMENTS

The completion of this dissertation could not have been possible without the help of many people. First and foremost, I want to thank my advisor Dr. Mahendra Sunkara for his guidance throughout all these years, he believed in my potential from day one, and has been an inspiration and a role model of what transformational research should be.

I want to thank many of the researchers and staff of the Conn Center. Eunice Salazar for her dedicated work in helping students manage the logistics of their research, Dr. Jacek Jasinski for what he taught me about materials characterization and for the TEM images he acquired, which are included in this document. Dr. William Paxton for helping me troubleshoot the growing tools that were used in the synthesis of the studied materials, and for showing me how to become an independent experimentalist. Dr. Daniel Jaramillo-Cabanzo for paving the way of gallium nitride synthesis through Plasma-Assisted Liquid Phase Epitaxy, a technique I extensively used to obtain ternary nitride alloys.

Kudos to my former and current lab mates for all the interesting discussions about our work and the support I received from them in many ways. Special gratitude to Dr. Tomas Starr, Dr. Thad Druffel and Dr. Gautam Gupta for agreeing to be part of the evaluation committee of this dissertation. It is an honor for me to receive their objective and knowledgeable feedback about this work.

Finally, I also want to express gratitude to the entities that provided the financial support I required to complete the Ph.D. program. The Department of Chemical Engineering of the University of Louisville supported me for 2 years through a teaching assistantship and the fellowship awarded by the Conn Center for Renewable Energy

Research for the remaining of the time. I was also temporarily funded by a grant from the National Science Foundation (NSF EPSCoR).

ABSTRACT

ANION ALLOYING OF III-V SEMICONDUCTORS FOR WATER SPLITTING

Sonia Juliana Calero Barney

November 15, 2022

The challenge of solar energy conversion and storage translates into the discovery and development of semiconductor materials that can transform sunlight energy into electricity and/or high-energy-density fuels in a cost-effective way. From the solar energy conversion perspective, cation-alloyed III-V solar cells hold record-breaking energy conversion efficiencies, while anion-alloyed III-V's are particularly interesting for photoelectrochemical hydrogen generation. The major challenge for the adoption of III-V-based technologies lies in the high manufacturing costs of established synthesis techniques and the difficulty to control the composition of ternary alloys.

One of the materials investigated in this work is $\text{GaSb}_z\text{P}_{1-z}$. Thermodynamic equilibrium and steady-state kinetics modeling of a Halide Vapor Phase Epitaxy (HVPE) reactor, facilitated process mapping for the growth of $\text{GaSb}_z\text{P}_{1-z}$ free-standing films with antimony incorporation levels up to 6.7 at% and a direct band gap shift from 2.68 to ~ 2.0 eV. The Water Splitting performance of these zincblende alloys revealed a more cathodic photocurrent onset potential, and an increased charge transfer efficiency at the alloy-electrolyte interface when compared to sulfur-doped commercial gallium phosphide.

For the first time, Plasma-Assisted Vapor Liquid Phase Epitaxy (PA-VLPE) was used to grow anion-alloyed $\text{GaSb}_x\text{N}_{1-x}$ and $\text{GaBi}_y\text{N}_{1-y}$ wurtzite nanowires. Gold or Copper coated substrates (silicon, sapphire, and stainless steel) enabled high antimony and bismuth incorporation levels since the dissolution of these species into the metals was favored at high growth temperatures. The nanowires showed a direct band gap shift from 3.4 to ~ 2.0 eV in the case of 5.6 at% antimony and 8.8 at% bismuth incorporation. Photoelectrochemical spectroscopy measurements showed efficient light absorption of 620 nm photons in the case of $\text{GaSb}_{0.056}\text{N}_{0.944}$ sample. On the other hand, samples with incorporation (x, y) below 1 at%, helped to confirm the existence of a band gap reduction discontinuity at such a low alloying levels.

The most significant accomplishments of this work are the demonstration of anion substitution control in the growth of $\text{GaSb}_z\text{P}_{1-z}$ alloys through HVPE and the demonstration of visible light absorbing $\text{GaSb}_x\text{N}_{1-x}$ and $\text{GaBi}_y\text{N}_{1-y}$ nanowires grown through PA-VLPE. These results apply to the growth of other anion-alloyed III-V systems in multi-junction high-efficiency photovoltaics, power devices, and solid-state laser applications.

TABLE OF CONTENTS

| | |
|---|-----|
| DEDICATION | iii |
| ACKNOWLEDGEMENTS | iv |
| ABSTRACT | vi |
| LIST OF FIGURES..... | xi |
| 1. CHAPTER ONE..... | 1 |
| INTRODUCTION..... | 1 |
| 1.1. Overall Goal | 1 |
| 1.2. Rationale and Motivation | 1 |
| 1.3. Objectives..... | 5 |
| 1.4. Organization of this Document | 6 |
| 2. CHAPTER TWO | 8 |
| BACKGROUND..... | 8 |
| 2.1. State-of-the-Art..... | 8 |
| 2.1.1. Materials for Water Splitting | 8 |
| 2.1.2. Challenges with III-V Alloys Synthesis | 11 |
| 2.1.3. Technoeconomic Overview..... | 17 |
| 2.2. Summary | 18 |
| 3. CHAPTER THREE | 19 |
| MATERIALS AND METHODS..... | 19 |
| 3.1. Halide Vapor Phase Epitaxy (HVPE) | 19 |

| | |
|--|----|
| 3.1.1. Reactor and Synthesis Conditions | 19 |
| 3.1.2. Thermodynamic Modeling and Simulation | 20 |
| 3.2. Plasma-Assisted Vapor Liquid Phase Epitaxy (PA-VLPE) | 25 |
| 3.3. Materials Characterization Techniques | 26 |
| 3.3.1. Electrochemical Measurements | 26 |
| 3.3.2. Uv-Vis Spectroscopy..... | 27 |
| 3.3.3. X-ray Diffraction | 27 |
| 3.3.4. Scanning and Transmission Electron Microscopy | 27 |
| 3.3.5. Raman and Photoluminescence Spectroscopy | 27 |
| 4. CHAPTER FOUR | 29 |
| GaSb _z P _{1-z} THROUGH HALIDE VAPOR PHASE EPITAXY | 29 |
| 4.1. Introduction..... | 29 |
| 4.2. Thermodynamic Modeling and Simulation of HVPE-grown GaSb _z P _{1-z} Alloys | 30 |
| 4.3. GaSb _z P _{1-z} Alloys Growth and Characterization..... | 34 |
| 4.3.1. Effect of the Substrate Temperature on Antimony Incorporation and Crystalline Quality of the Films | 34 |
| 4.3.2. Optoelectronic Properties and Photoelectrochemical Performance | 36 |
| 4.4. Summary | 42 |
| 5. CHAPTER FIVE | 43 |
| DILUTE ANION ALLOYED, GaSb _x N _{1-x} AND GaBi _y N _{1-y} FILM SYNTHESIS THROUGH PLASMA ASSISTED VAPOR LIQUID PHASE EPITAXY | 43 |
| 5.1. Introduction..... | 43 |
| 5.2. Growth of GaSb _x N _{1-x} and GaBi _y N _{1-y} Films | 45 |

| | |
|---|----|
| 5.3. GaSb _x N _{1-x} and GaBi _y N _{1-y} Film Characterization | 46 |
| 5.4. Summary | 54 |
| 6. CHAPTER SIX..... | 55 |
| GaSb _x N _{1-x} AND GaBi _y N _{1-y} NANOWIRE GROWTH THROUGH METAL CATALYZED PLASMA-ASSISTED VAPOR LIQUID PHASE EPITAXY | 55 |
| 6.1. Introduction..... | 55 |
| 6.2. Metal Catalyzed GaSb _x N _{1-x} and GaBi _z N _{1-z} Nanowire Growth | 56 |
| 6.3. GaSb _x N _{1-x} and GaBi _y N _{1-y} Nanowire Characterization..... | 57 |
| 6.4. Summary | 72 |
| 7. CHAPTER SEVEN | 74 |
| CONCLUSIONS | 74 |
| 8. CHAPTER EIGHT | 76 |
| RECOMMENDATIONS..... | 76 |
| REFERENCES..... | 77 |
| CURRICULUM VITAE..... | 87 |

LIST OF FIGURES

| | |
|--|-----------|
| <i>Figure 1.1 Shockley-Queisser limit to the photo-conversion efficiency under condition AM 1.5 as a function of the band gap of the material.</i> | <i>2</i> |
| <i>Figure 1.2 Photo-electrochemical cell for Water Splitting.....</i> | <i>3</i> |
| <i>Figure 1.3 Band edge positions of III-V materials vs HER & OER potentials. (Adapted from Joe et. al.).....</i> | <i>4</i> |
| <i>Figure 3.1 Schematic of the experimental setup illustrating two zones: first zone in which precursor generation occurs at gas-solid/liquid equilibrium and second zone in which precursor composition is under steady state condition through gas and gas-solid kinetics.....</i> | <i>20</i> |
| <i>Figure 3.2 Experimental setup (gases, radio frequency plasma source and furnace).....</i> | <i>26</i> |
| <i>Figure 4.1. a. Most abundant gaseous species in zone 1 under thermodynamic equilibrium, b. Less abundant gaseous species in zone 1 under thermodynamic equilibrium, c. Most abundant gaseous species in zone 2 under steady state conditions, d. Film growth rate versus inverse temperature of the substrate.</i> | <i>30</i> |
| <i>Figure 4.2 Cross sectional SEM images of free standing GaSb_zP_{1-z} films grown at different substrate temperatures: a. 400 °C, b. 600 °C, c. 690 °C, d. 710 °C, e. 725 °C and f. X-ray spectra of the samples grown at substrate temperatures</i> | |

between 400 °C and 725 °C. Grey dashed and black lines correspond to pure GaP (PDF-00-012-0191) and Sb (PDF-00-001-0802) spectra, respectively. 35

Figure 4.3 Direct Tauc plots from diffuse reflectance measurements of 5 GaSb_zP_{1-z} films grown between 600 and 725 °C with different Sb incorporation levels 37

Figure 4. 4 GaP and GaSb_zP_{1-z} band structure schematic..... 37

Figure 4.5 a. Chronopotentiometry measurements under intermittent 6 sun (full spectrum) and at a current of 0 A. b Linear Sweep Voltammeteries under 6 sun (full spectrum) for GaSb_zP_{1-z} photoanodes with different Sb incorporation levels compared to a commercial sulfur-doped GaP wafer 39

Figure 4.6 a. Linear Sweep Voltammeteries under intermittent 470nm LED illumination (506 mW*cm⁻²) for GaSb_zP_{1-z} photoanodes with different Sb incorporation levels compared to a commercial sulfur-doped GaP wafer. b. Impedance spectroscopy measurements at 0V vs RHE of the GaSb_yP_{1-y} photoanodes compared to a sulfur-doped GaP wafer and an Ir_xWO_{3-x} co-catalyzed GaSb_yP_{1-y} alloy, under a 470nm LED illumination of (506 mW*cm⁻²). 40

Figure 5.1 Schematic of the Ga(Sb or Bi)_xN_{1-x} alloy growth process. 46

Figure 5.2 Cross sectional transmission electron micrograph (a) and scanning electron micrograph (b); top view scanning electron micrographs of GaSb_{0.003}N_{0.997} alloy on GaN (c & d). 47

Figure 5.3 Antimony mapping across GaN substrate and GaSb_{0.003}N_{0.997} alloy.. 47

| | |
|---|----|
| Figure 5.4 Complete XRD spectra of different $\text{GaSb}_x\text{N}_{1-x}$, $\text{GaBi}_y\text{N}_{1-y}$, GaN and sapphire samples..... | 49 |
| Figure 5.5 a. High resolution Transmission Electron Micrographs of sample $\text{GaSb}_{0.003}\text{N}_{0.997}$ b. X-ray diffraction spectra of GaN, sapphire, $\text{GaSb}_x\text{N}_{1-x}$ and $\text{GaBi}_y\text{N}_{1-y}$ alloys..... | 51 |
| Figure 5.6 Absorption coefficient (left), and photoluminescence spectra (right) of GaN, $\text{GaSb}_x\text{N}_{1-x}$ and $\text{GaBi}_y\text{N}_{1-y}$ alloys..... | 52 |
| Figure 5.7 Photoluminescence measurements at room temperature and -196 °C of GaN, $\text{GaSb}_x\text{N}_{1-x}$, $\text{GaBi}_y\text{N}_{1-y}$ on sapphire. | 53 |
| Figure 6.1 $\text{GaSb}_x\text{N}_{1-x}$ wires grown at a. 800 °C, b. 850 °C and c. 950 °C. $\text{GaBi}_y\text{N}_{1-y}$ wires grown at d. 900 °C and e. 950 °C..... | 59 |
| Figure 6.2 a. $\text{GaSb}_{0.041}\text{N}_{0.959}$ wire grown at 850 °C showing a-plane orientation, b. its corresponding diffraction pattern, c. and d. high-resolution Transmission Electron Micrographs of wire's c-plane orientation..... | 60 |
| Figure 6.3 X-ray diffraction measurements of a. $\text{GaSb}_x\text{N}_{1-x}$ and b. $\text{GaBi}_y\text{N}_{1-y}$ samples with different degrees of alloying..... | 61 |
| Figure 6. 4 Plasma-Assisted Vapor Liquid Solid growth mechanism..... | 62 |
| Figure 6.5 High resolution Transmission Electron Micrograph of a. $\text{GaSb}_x\text{N}_{1-x}$ wires grown at 850 °C, b. the corresponding High-angle annular dark-field image, and the elemental mapping of c. copper, d. gallium and e. antimony. | 63 |
| Figure 6.6 Tauc plots of a. $\text{GaSb}_x\text{N}_{1-x}$ and b. $\text{GaBi}_y\text{N}_{1-y}$ samples with different degrees of alloying..... | 64 |

| | |
|---|-----------|
| <i>Figure 6.7 Photocurrent spectroscopy measurements of GaSb_{0.056}N_{0.944} and GaSb_{0.041}N_{0.959} samples.....</i> | <i>66</i> |
| <i>Figure 6.8 Photocurrent density versus applied bias in 3-electrode configuration of Ir_xWO_{3-x} decorated samples GaSb_{0.041}N_{0.959}, GaSb_{0.049}N_{0.951} and GaSb_{0.056}N_{0.944}, under 1, 5 and 10 sun irradiance. Performance of same three samples under 10 sun without Ir_xWO_{3-x} (inset).</i> | <i>68</i> |
| <i>Figure 6.9 Photocurrent density versus applied bias in 3-electrode configuration, under 10 sun irradiance of full spectrum (grey lines) or 470 nm (black lines). a. GaSb_{0.041}N_{0.959}, b. GaSb_{0.049}N_{0.951} and c. GaSb_{0.056}N_{0.944}. d. Optical absorption coefficient versus photon energy of same three samples (solid lines) and x10(AM 1.5 G) irradiance versus photon energy (dotted line)</i> | <i>69</i> |
| <i>Figure 6.10 Photocurrent density versus time of sample GaSb_{0.056}N_{0.944} in a 2-electrode configuration (p-Si counter electrode), at 0.5 V vs RHE and 10 sun/470 nm illumination.....</i> | <i>71</i> |
| <i>Figure 6. 11 Scanning Electron Micrographs and X-ray diffraction spectra of sample GaSb_{0.056}N_{0.944} before (a & c) and after (b & d) stability measurements.</i> | <i>72</i> |

1. CHAPTER ONE

INTRODUCTION

1.1.Overall Goal

The challenge of solar energy conversion and storage translates into the discovery and development of semiconductor materials that can transform sunlight energy into electricity and/or high-density fuels. Previous investigations on $\text{GaSb}_x\text{N}_{1-x}$ and $\text{GaSb}_z\text{P}_{1-z}$ alloys have shown good potential to accomplish that goal, however challenges associated to their synthesis processes have prevented the achievement of their fullest potential as photoanodes for Water Splitting¹⁻³. The general objective of this work is to overcome those synthesis challenges by modifying and developing new techniques to produce high-quality, visible light absorbing $\text{Ga}(\text{Sb or Bi})_x\text{N}_{1-x}$ and $\text{GaSb}_z\text{P}_{1-z}$ alloys, with high substitutional anion incorporation fractions and direct band gap values between 1.7 and 2.0 eV. “Halide Vapor Phase Epitaxy” and “Vapor Liquid Phase Epitaxy” will be modified to study the synthesis of these alloys.

1.2.Rationale and Motivation

The overall motivation of this dissertation is to contribute to the effort of migrating from fossil fuels to renewable energy sources necessary to keep the global temperature raise below 1.5 °C and CO₂ atmospheric concentration below 400 ppm. By far, solar energy is the most abundant renewable resource (89 TW/1.5h) and therefore a clear pathway to meet the energy demand worldwide in a clean way. Single junction silicon solar cells are

reaching their theoretical maximum solar to electricity conversion efficiency of 30% (see Figure 1.1) and to meet the ever-increasing global energy demand using the smallest possible land it is necessary to use ultrahigh efficiency devices and/or solar concentration technologies.

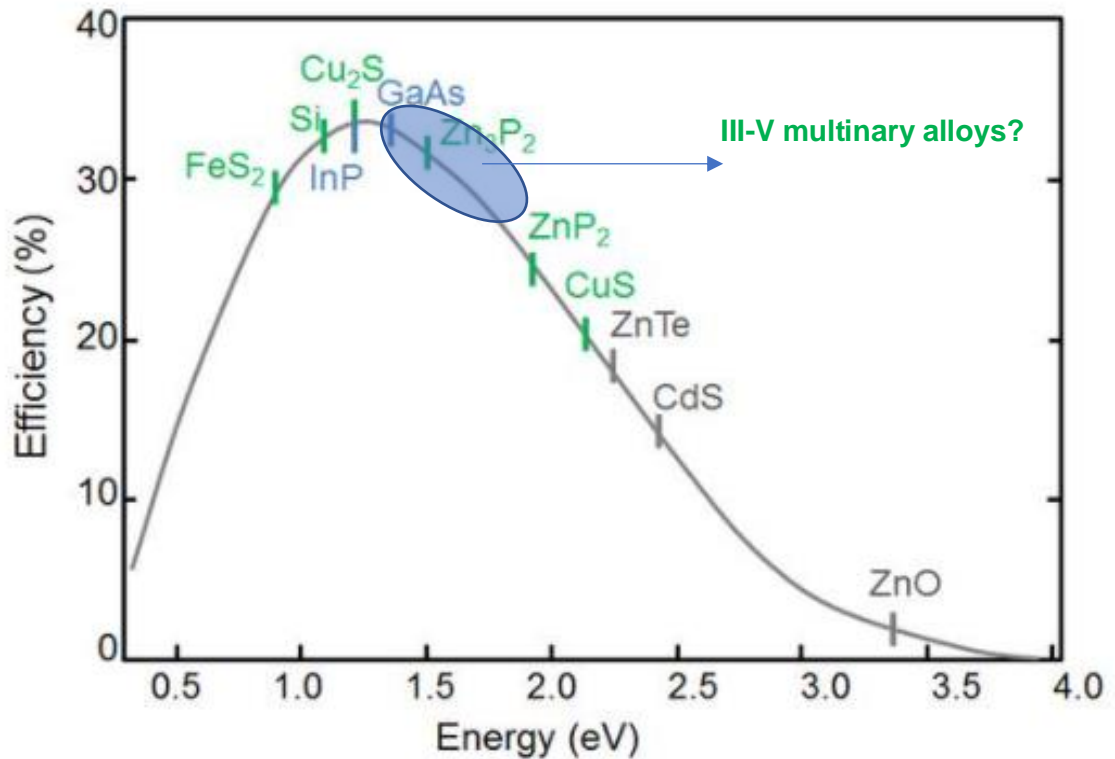


Figure 1.1 Shockley-Queisser limit to the photo-conversion efficiency under condition AM 1.5 as a function of the band gap of the material.

Furthermore, the converted energy storage is a challenge that must be overcome simultaneously. The European Union and USA have proposed hydrogen generation as a key component in their renewable energy plans,⁴ the former is investing in photovoltaic plus electrolyzer systems to perform water splitting photo-electrosynthesis and the latter is funding integrated device approaches of the photo-electrocatalysis type (see Figure 1.2). The detailed analysis of each type of technology is a very broad discussion that is

out of the scope of this dissertation, but in either scenario, the progress made in high energy conversion efficiency materials will have a great impact.

The process of water photo-electrocatalysis has various requirements; since the materials are in direct contact with the electrolyte, they must be stable in aqueous media; the photovoltage generated by the semiconductor electrode needs to be greater than the 1.23 V thermodynamic barrier for water oxidation and hydrogen reduction plus an overpotential associated with reaction kinetics, hence, narrow bandgap semiconductors such as silicon, InP, GaAs do not fulfill this requirement. The light absorption capabilities of the semiconductor material should be direct in nature and capture visible photons of the solar spectrum (wide bandgap materials such as WO_3 and TiO_2 get excluded). And finally, the Conduction Band Edge (CBE) and Valence Band Edge (VBE) must be appropriately aligned; this means that upon Fermi level equilibration between the semiconductor and the electrolyte the CBE must be more negative than the hydrogen reduction potential and the VBE must be more positive than the water oxidation potential, for a p-type and an n-type semiconductor electrodes, respectively, or both conditions simultaneously in the case of a single absorber material.

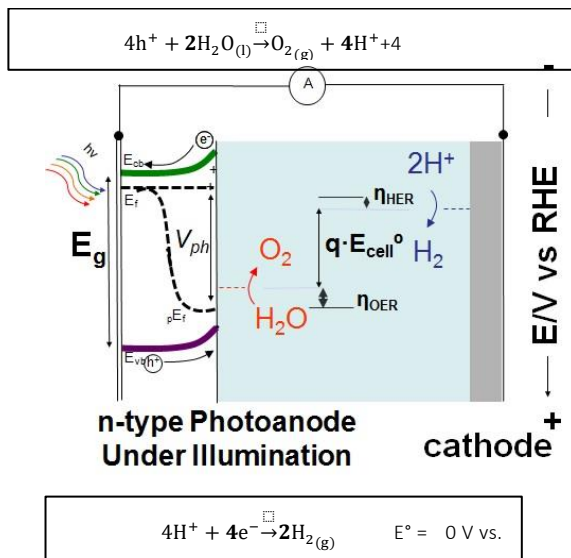


Figure 1.2 Photo-electrochemical cell for Water Splitting

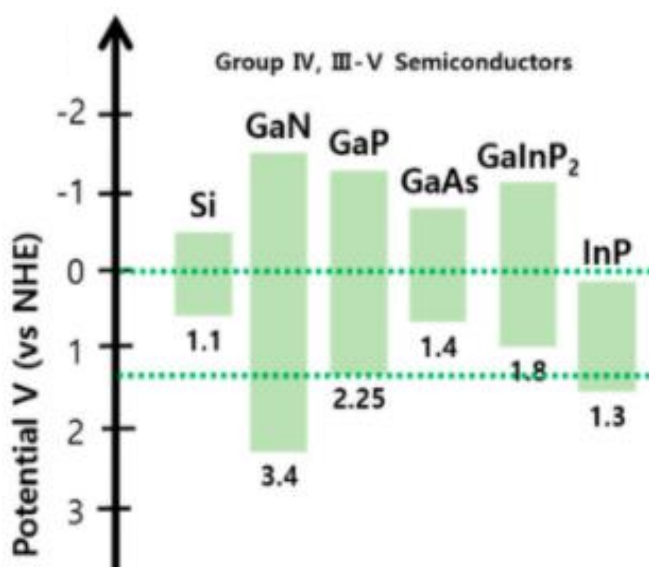


Figure 1.3 Band edge positions of III-V materials vs HER & OER potentials. (Adapted from Joe et. al.)

Currently the solar-to-hydrogen (STH) conversion efficiency records are held by Metal Organic Vapor Phase Epitaxy grown III-V alloys; the band gap and lattice constant tuning upon ternary alloying have made it possible. A double junction of 1.78eV $\text{Ga}_{0.41}\text{In}_{0.59}\text{P}$ top cell coupled to a 1.26eV $\text{Ga}_{0.89}\text{In}_{0.11}\text{As}$ bottom cell achieved a STH conversion efficiency of 19%. Also, a 1.8eV-GaInP/1.2eV-GaInAs tandem cell reached 16.2% STH efficiency. The key common element to both designs is the top phosphide absorber resulting from the cation alloying of indium into GaP, and a bottom semiconductor that adds photovoltage to straddle the Oxygen Evolution Potential. As can be seen in Figure 1.3, GaInP₂ would need the same type of coupling due to its low valence band edge.

The state-of-the-art results are very promising but the fact they have been obtained with expensive processes and raw materials (In), calls for the development of more cost-effective options. Furthermore, MBE and MOVPE have not been particularly attractive for

anion alloying of III-nitrides, due to low anion incorporation at the high synthesis temperatures required to obtain good crystalline quality.¹

Anion alloying of III-V materials, i.e., antimony or bismuth into GaN or GaP, can also produce a band gap reduction of the binary host. However, the behavior of anion alloyed III-nitrides in terms of their potential toward water splitting have not been fully explored. This is because the existing methods have not enabled the growth of crystalline materials with high levels of anion incorporation as explained before. Many questions related to the alloy's properties-synthesis relationship remain unanswered motivating this dissertation. In particular, the synthesis conditions to achieve high crystalline quality and high anion incorporation levels have been investigated.

1.3.Objectives

Primary goal is to develop inexpensive synthesis methods for single crystal quality layers of visible light absorbing $\text{Ga}(\text{Sb or Bi})_x\text{N}_{1-x}$ and $\text{GaSb}_z\text{P}_{1-z}$ alloys, with high substitutional anion incorporation fractions (>10%) and band gap values between 1.7 eV and 2.0 eV, suitable for water splitting applications. Specifically, the objectives of this dissertation are the following:

- Develop a synthesis process for $\text{GaSb}_x\text{N}_{1-x}$ alloys that allows fine control of the incorporation fraction and produce samples with less than 3 at% antimony. Evaluate if such a low incorporation level produces changes in optoelectronic properties.
- Enhance crystalline quality of HVPE-grown $\text{GaSb}_y\text{P}_{1-y}$ alloys by conducting experiments at high substrate temperatures (>650C) and evaluate the effect on the material's photoelectrochemical performance.

- Investigate substitutional anion incorporation in PA-VLPE grown Ga(Sb or Bi)_xN_{1-x} alloys, by introducing other metals into the reacting system (Au or Cu) that add degrees of freedom in terms of thermodynamic and solubility phenomena.
- Increase substitutional anion incorporation into PA-VLPE-grown Ga(Sb or Bi)_x N_{1-x} alloys by facilitating the steps of precursor decomposition and dissolution into Ga, Au and Cu with changes in the melt temperature and/or plasma conditions.

1.4. Organization of this Document

Chapter 2 covers the state of the art of III-V alloys for water splitting applications. It is explained how anion alloyed III-V have paved the way to achieve high solar to hydrogen conversion efficiencies and what are the issues that still need to be addressed.

Chapter 3 details the growing tools that were used in this dissertation, namely Halide Vapor Phase Epitaxy (HVPE) and Plasma-Assisted Vapor Liquid Phase Epitaxy (PA-VLPE) reactors. The methodology employed for the thermodynamic and kinetic modeling of the HVPE reactor, including the approach, the mass balance and the Arrhenius parameters of an extensive reaction set, are presented in this chapter. The materials characterization techniques (Scanning and Transmission Electron Microscopy, X-ray Diffraction, Diffuse Reflectance, Photoluminescence Spectroscopy, and Photoelectrochemical measurements) are also listed in this chapter and some of the key settings used in the acquisition of the data were reported.

Chapter 4 presents the results of the modeling, synthesis, and characterization of GaSb₂P_{1-z} alloys. Chapter 5 is focused on the synthesis through PA-VLPE and

optoelectronic properties of dilute $\text{GaSb}_x\text{N}_{1-x}$ and $\text{GaBi}_y\text{N}_{1-y}$ alloys and elucidating the existence of a band gap reduction discontinuity in anion alloyed nitrides.

Chapter 6 presents the most significant contribution of the present work. It details the results obtained with the plasma assisted VLPE technique and its use for growing anion alloyed $\text{GaSb}_x\text{N}_{1-x}$ and $\text{GaBi}_y\text{N}_{1-y}$ nanowires and demonstration of their capability in absorbing visible wavelength photons due to antimony and bismuth incorporation up to 5.6 and 8.8 at%, respectively. The photoelectrochemical characteristics of these alloys are analyzed.

Chapter 7 and 8 encompass this work with conclusions and recommendations. Chapter 9 lists bibliographic references.

2. CHAPTER TWO

BACKGROUND

2.1.State-of-the-Art

2.1.1.Materials for Water Splitting

Artificial photosynthesis has been attempted with different approaches over time. The most straightforward form is to couple a photovoltaic device with an electrolyzer equipped with platinum electrodes, decoupling the photon to current conversion from the current to chemical step. This approach, which in rigorous nomenclature is termed as photovoltaic electro-synthetic system, eliminates the need to fulfill all water splitting requirements within a single material or tandem of materials, but it also introduces energy losses that result in cost effectiveness issues⁵. Recent advances with solar concentration have enabled a record STH efficiency of 30% with a device comprised of a triple junction solar cell GaInP/GaAs/GaInNAsSb and 2 series connected electrolyzers.⁶ A variety of options within the systems that integrate light-to-current conversion and current-to-chemical conversion (photoelectrochemical systems) where semiconductor-liquid junctions with photogenerated minority carriers being transported to the interface to participate in oxidation and reduction reactions and majority carriers flowing towards the bulk to recombine at an ohmic contact closing the electrical circuit, have been studied so far.⁵The experimental setup to conduct photoelectrochemical processes can be composed of a photoanode and a photocathode connected by an external circuit and immersed in an aqueous solution while carrying out water oxidation and hydrogen reduction, respectively. The system can also be monolithically integrated (i.e particles or sheets) eliminating the

need of an external circuit and exploiting the charge carrier separation and transport enhancement (drift vs diffusion) derived from the electric field formation at the junction between different semiconductor materials. There are different types of junctions that can result, among the most commonly found in the literature for PEC applications is Type II heterojunction, which exhibits a staggered alignment of the bands; the simple p-n junction where minority carriers recombine at the junction interface generating a stronger electric field and charge separation efficiency than Type II junction; and the z-scheme junction where majority carriers recombine at the junction interface and minority carriers are available to be extracted at the semiconductor/electrolyte interface.

In order for such type of system to be able to perform water splitting without the need of an external bias, the energy it generates upon illumination has to be greater than the thermodynamic requirements for the water splitting reactions (1.23 V) plus the kinetic overpotential (0.4 - 0.6 V), furthermore, the energetic level of the minority electrons has to be above 1.23 V vs RHE and the energy of minority holes has to be below 0 V vs RHE in order for these carriers to be transferred and participate in redox reactions. Wide bandgap semiconductors are likely to meet these 2 criteria but as a result, the portion of the solar spectrum they can absorb is limited.

As briefly mentioned earlier, charge carriers also need a transport mechanism faster than diffusion and they need to be effectively separated (minority holes separated from majority electrons in the OER material/site, and minority electrons separated from majority holes in the HER material/site). The built-in electric field that forms between the semiconductor and the electrolyte due to the Fermi level equilibration enhances charge separation by promoting drift-like carrier transport, although not effective enough to suppress recombination processes. To serve transport purposes and harvest a larger portion of the solar spectrum, multijunction tandem devices have been proposed. The electric field generated by heterojunctions allows carriers to be effectively separated and

transported, and because these two aspects are unrelated to the chemical kinetic steps, heterojunctions do not need to be exposed to the electrolyte; that is the reason they are often referred to as buried junctions.

Multijunction PEC cells are usually fabricated with III-V alloys, not only because of the outstanding optoelectronic properties of these kind of materials but also because of the possibility to tune the bandgap and lattice parameter by modifying the composition of the alloys. Tuning the bandgap to desired specific values allows for optimization of the solar to hydrogen conversion efficiency, and on the other hand, tuning the lattice parameter enables the metamorphic growth of heterojunctions with alloys of drastically different lattice parameters, with the use of compositionally graded buffers in between. Among the most efficient III-V tandem structures to date are a 1.78 eV GaIn top cell coupled with a 1.26 eV GaInAs bottom cell (14% STH)⁷; a 1.8eV GaInP top cell coupled with a 1.2eV GaInAs bottom cell (16.2% STH)⁸ and a passivated 1.78 eV GaInP top cell coupled with a 1.26 eV GaInAs bottom cell (19.3% STH)⁹. Unlike photovoltaic applications, in PEC is not common to find more than 2 junctions in a device, because even though the photovoltage increases with the number of junctions, the photocurrent decreases due to the series connection.¹⁰

The challenges associated with light absorption and charge transport have also been addressed using nanostructures. In oriented nanowires arrays for example, the light absorption and charge separation directions are orthogonalized, the light is absorbed as much as the absorption penetration depth of the material allows, and the distance the photogenerated charges must travel from the point of generation to the interface with the electrolyte in the case of minority carriers and to the ohmic contact in the case of majority carriers, is typically shorter than in a planar analogous material. This is particularly important in semiconductor materials with minority carrier diffusion lengths and depletion regions significantly shorter than the absorption depths of incident photons¹¹.

Among the advantages of nanostructures in photoelectrochemical processes, the increased surface area has been credited for the lower adsorption energies of reactive intermediates that participate the water splitting reaction mechanism¹¹. However, the chemical stability of large area semiconductors can be compromised, particularly if the overpotential of holes towards semiconductor oxidation is greater than that of water oxidation. Likewise, if the overpotential of electrons towards semiconductor reduction is greater than that of hydrogen reduction, the use of passivation layers is necessary. TiO₂ or Al₂O₃ are common passivation layers given their good chemical stability.

2.1.2.Challenges with III-V Alloys Synthesis

The synthesis of III-Vs material as in many other semiconductors can proceed through liquid-solid or gas-solid mechanisms. In the former the driving force is a temperature gradient between the two phases. Super-cooling below the melting point should take place for the solid phase to form and the heat of formation removal is the limiting step for the growth. In the case of gas-solid reactions, the driving force for film deposition is species gas phase supersaturation, which means the difference between the partial pressure and the equilibrium pressure of key species at a certain temperature is a positive number. When supersaturation is achieved, surface reconstruction happens through a series of multiple steps, i.e. species impinging on the surface, diffusing to a surface site, decomposing into mono or dimeric forms, further diffusing, and reacting.

The law of mass action (Equation 1) correlates the activity of the solid phase with the partial pressures of the reacting species and is an exponential function of the Gibbs free energy as can be seen in Equation 1. The right side of the equation decreases very fast with increasing temperature, implying that under such conditions, high partial pressures are required.

$$K_{eq} = \frac{a_{MX}}{P_M P_X^{1/n} / P_T^{1+1/n}} = \exp(-\Delta G_f^0 / RT) \quad \text{Equation 1}$$

The two most common gas-solid epitaxial growth techniques are Molecular Beam Epitaxy (MBE) and Metal Organic Vapor Phase Epitaxy (MOVPE). MBE is characterized for ultra-high vacuum conditions, transport in the molecular flow regime and surface processes are faster than transport processes. MBE is advantageous regarding the high purity, control of the composition and structure at the monolayer scale. Anion to cation (V/III) ratios equal or higher than one are used, which poses a challenge when growing multiple layers differing in the anion species, because anion substitution in the gas phase will proceed slowly. Differences in anion surface adsorption (in the case of mixed anion alloys) can produce pure metal monolayers on the growth front that can act as diffusional pathways leading to phase segregation¹² as observed in the case of GaAsBi growth through MBE with Bi segregation.

MOVPE uses V/III ratios in the order of 10 to 1000, mainly because anion precursors suffer from thermodynamic stability at elevated temperatures and the vapor pressure of the V-group cations is typically low. Pressures are in the range of 1 to 100 torr, reactants are fed through shower heads and samples are held in rotating disks to compensate radial non-uniformities. The growth is characterized by three regimes, at low temperature the surface reconstruction processes are limiting because they depend heavily on temperature, at moderate temperatures what reaches the surface is easily incorporated through reactions and the growth is limited by transport diffusion processes that have a weak dependence on temperature (these conditions favor epitaxial growth). At high temperatures desorption from the surface is faster than adsorption and decomposition of precursors in the gas phase is also prevalent, therefore the film growth rate is diminished.

The advantages of MOVPE include the rapid change of gas phase composition and increased safety inherent to low pressures. Its disadvantages include the difficulty to grow mixed V-group alloys since competing reactions can take place and neither anion would be a limiting reactant. Furthermore, metalorganic precursors can lead to additional challenges, one being the unintended carbon incorporation negatively impacting optoelectronic and kinetics properties as reported in the growth of GaAsBi through MOVPE; researchers identified differences for the samples grown using TEBi and TMBi as the source of Bismuth, in the case of TMBi the methyl radicals didn't desorb creating a Bi-CH₃ terminated surface that later became a Bi monolayer, hindering the incorporation of Bi in the alloy.¹³

The growth of III-V semiconductors through HVPE uses gas phase precursors of V element species, typically hydrides and gaseous halide species of the III group of the periodic table, transported in vertical or horizontal hot wall chambers. The species reach a single crystal substrate where they get adsorbed and react forming the solid film.

Halide Vapor Phase Epitaxy offers benefits over other gas-solid mechanisms, for example, it doesn't require the use of expensive group III metalorganic compounds, it has higher utilization of the group-V hydrides and growth rates are one-two orders of magnitude higher than MOVPE and MBE respectively. This is attributed to the faster transfer kinetics that don't involve reduction of many intermediate compounds.

III-V crystalline quality is not compromised with HVPE. The growth of GaAs on Ge (001) substrates with 6° miscut towards [111] was successfully conducted yielding a growth rate of 44um/h and values of surface roughness and FWHM lower than films of the same material/substrate grown by MOVPE¹⁴. The only drawback of HVPE is that because of the high growth rates, it is difficult to deposit layers of different materials with very sharp interfaces between them which is typically the case in the p-n junction of solar cells¹⁵

A challenge that is common to gas-solid synthesis techniques is the difficulty of group-V anion incorporation at high substrate temperatures. Typically, ternary alloy's optimized growth temperatures are lower than those for their binary counterparts and that is because at lower temperatures species surface diffusion and desorption are hindered. For example, the growth of GaAsBi and GaAsN with MOVPE can only be accomplished without phase segregation below 400C, condition at which the self-diffusion coefficients of Ga, Bi and N in GaAs are in the order of $1 \cdot 10^{-30} \text{ cm}^2/\text{s}$.

Additionally, low temperature in pseudomorphically grown alloys produces a high dislocation density that can help decrease the strain generated by the introduction of a smaller or larger element into the host material, increasing the foreign element solubility. One example to illustrate this, is the plasma-assisted MBE growth of GaNBi at a temperature of at $\sim 80\text{-}90\text{C}$, where researchers were able to observe signs of polycrystalline growth with as less as 0.5mol% of bismuth incorporation in the alloy. It was also observed that a 3.5mol% of bismuth incorporation was necessary to bring the band gap below 2.5 eV.¹⁶ In this order of ideas, a pseudomorphically grown alloy for which the lattice parameter increases upon incorporation of a foreign element, will show a higher level of incorporation in single phase when the lattice parameter of the substrate where it is grown is larger, because the lattice mismatch between the substrate and the alloy will decrease and so the compressive elastic strain in the alloy. The drawback of this approach is that optoelectronic properties of III-V materials are negatively impacted by high dislocation densities.

Fortunately, there are examples in the literature where¹⁷ high defect densities have been circumvented even in alloys with high substitutional anion levels. This has been achieved by taking advantage of 1D morphologies which are able to relax strains produced in alloys.

On the thermodynamic aspect, the phase which is in equilibrium with the desired alloy can also influence its composition and stability, for instance, if the alloy has a high thermodynamic drive to decompose into the phase that is in equilibrium with it, the likelihood of stepping into the miscibility gap conditions is higher. A DFT simulation for the GaAsBi system concluded that Bi solubility in the alloy can be increased by a 100 times if Bi metal formation is inhibited.¹⁸

Liquid-solid growth techniques are another growth alternative. Liquid Phase Epitaxy (LPE) has been used in the synthesis of III-Vs,¹⁹ it was predominant during the early development of multi-junction devices and delivers high quality materials with sharp compositional gradients required in multi-junctions. Its drawback relies in the low throughput and small processing areas. The control of the shape of the solid-liquid interphase, the temperature gradient and distribution, etc, play critical roles in the obtention of uniform crystals. Quaternary phase diagrams show the miscibility range reduces with increasing temperature as mentioned before, and an alternative is to grow the materials far from equilibrium conditions to use high temperatures and take advantage of the benefits it offers.

Another aspect to control during liquid-solid growth is the vapor pressure differences between anions and cations. Anion's vapor pressures are orders of magnitude higher than those of cation's, so a high total pressure cannot be used as strategy to prevent anion vaporization. The successful strategies used in the past involve the use of encapsulant gases over the melt of to maintain a vapor concentration of the anion in the gas phase adjacent to the melt, preventing anion depletion and non-stoichiometric solid formation. LPE is the epitaxial synthesis technique that falls within this type of growth.

There has been significant progress in the growth of cation diluted ($\text{III}_{1-x}\text{III}_x\text{V}$) nanowires, i. e., GaInP, GaInAs, AlGaAs, and AlGaP.²⁰ InGaN films in particular have shown continuous band gap reduction, reaching values of 2.7 to 2.1 eV with In

incorporation between 4 to 20 mol%, respectively²¹ or In mol% > 20²². On the other hand, anion diluted (IIIV_{1-x}V_x) counterparts have received less attention.²⁰ GaAsSb, InAsSb, InAsP and GaAsP have been synthesized through selective area vapor-solid,²³ or catalyzed vapor-liquid-solid²⁴ mechanisms, which constitute variations of well-established MOVPE, MOCVD and MBE synthesis techniques. The proposed applications for these anion diluted alloys revolve around transistors and infrared sensors.

Research on anion diluted nitrides is even more scarce since their synthesis through MOCVD and MBE has always been a challenge because of the low decomposition and evaporation temperatures of GaN and group-III elements, respectively,²⁵ which contrast with the high temperatures required for ammonia cracking. To circumvent these challenges many works on binary GaN, and AlN systems introduced the use of nitrogen plasma, enabling the growth at lower temperatures compared to ammonia sourced MBE and MOCVD.²⁶ Plasma-assisted techniques have also made possible the growth of In-containing nitrides, otherwise limited by InN low sublimation temperature at moderate pressures.²⁷

Lower growth temperatures in plasma-assisted vapor-solid growth techniques have also served to overcome challenges in the synthesis of IIIV_{1-x}N_x nitrides that suffer from low anion substitution, due to the high vapor pressures of group-V elements. Through Plasma Assisted Molecular Beam Epitaxy (PA-MBE), 1.2 eV band gap GaBi_{0.11}N_{0.89} was achieved¹⁶ Other studies of alloys with visible light absorption behavior such as PA-MBE-grown GaSbN, report a drastic band gap shift from 3.4 to 2 eV with antimony content below 5 mol%,²⁸ and 1 mol%²⁹ In contrast, in our own experimental work on Plasma Assisted Vapor Liquid Phase Epitaxy (PA-VLPE) synthesis of GaSbN and GaBiN films, we did not observe a band gap reduction (versus pure GaN) for alloys with antimony or bismuth content less than 1 at%, and DFT simulations suggest GaN band gap reduction can only be achieved when antimony content is between 2 - 3 at%.³⁰ Other studies by our

group with ammonia sourced² and Plasma-Assisted¹ MOCVD, have enabled the growth of GaSbN films (2 - 8 Sb at%) and nanowires (2 - 4 Sb at%) with band gaps around to 2 eV. Results that coincide more closely with ours PA-MBE-grown GaSbN nanowires with antimony content between 3 to 10 mol%, exhibited sub-bandgap light absorption.³¹

2.1.3. Technoeconomic Overview

Recently HVPE has regained attention as a method for III-V synthesis as the results have shown high growth rates while keeping the defect density low, it is also one of the most promising ways III-V semiconductors can be implemented in mainstream PV applications because the manufacturing costs can be significantly reduced due to more affordable precursors and shorter processing times that imply less capital costs.³² Schulte et. al. compared synthesis costs of III/Vs through HVPE and MOVPE, reporting raw materials cost and V/III ratio of one order of magnitude lower in the case of HVPE.³³

HVPE uses elemental metallic sources such as Gallium that costs around ten times less than trimethylgallium used in metalorganic chemical vapor deposition (MOCVD) systems and uses an order of magnitude lower V/III ratios³³. Additionally, HVPE is a high throughput process with growth rates in the order of hundreds of microns per hour which allows optimization of the processing time and lowers the capital costs.³⁴

The use of epitaxial lift-off and other film removal strategies is also under development due to potential cost reduction that can be obtained by substrate reuse.³⁵

In the case of III-Nitrides, traditional MBE, MOVPE and HVPE are characterized by the use of large amounts of ammonia, which not only poses a risk hazard but also accounts for 30-50 % of MOCVD costs³⁶ due to its low incorporation efficiency (3.8% at 700 C)²⁵. MBE, MOVPE, HVPE as well as LPE can replace ammonia with nitrogen gas

in conjunction with plasma ionization to enhance the reactivity of nitrogen with other species.

2.2. Summary

Significant progress has been made to increase the efficiency of III-V devices for water splitting and it has been proved that cation and anion alloying of III-Vs is feasible with good control of composition and quality in either 0-D and 1-D structures.

One challenge that still needs to be addressed is related to band gap engineering and simultaneous band edge alignment with respect to oxygen and hydrogen evolution potentials. Furthermore, due to the visible light absorption behavior of anion diluted nitrides, most of the revised literature signals optimism on their performance as photo-electrodes for water splitting applications, but few studies demonstrate it.

Another remaining challenge is associated with the cost-effectiveness of III-V synthesis methods since it is difficult to reduce III-V synthesis costs with incumbent techniques (MBE and MOVPE).

3. CHAPTER THREE

MATERIALS AND METHODS

3.1. Halide Vapor Phase Epitaxy (HVPE)

3.1.1. Reactor and Synthesis Conditions

The experimental setup for the growth of GaSb_yP_{1-y} alloys is shown in Figure 3.1 and consists of a quartz tube with a volume of 1.2 L, fitted in a two-zone furnace and equipped with an additional zone for inductively heating a graphite susceptor where a 111 silicon substrate was held. The reactor is coupled to two gas lines that mix before the entrance and carry 125 sccm of pure hydrogen and 100 sccm of hydrogen that has been previously flown through a bubbler containing phosphorous trichloride, maintained at a constant temperature of 35 °C. In each of the furnace zones quartz boats are placed, the first with 5 g of antimony powder and the second with 10 g of gallium. The pressure inside the reactor was 500 torr and the antimony and gallium zones were kept at 750 °C and 970 °C respectively. The substrate temperature was varied between 400 °C and 725 °C.

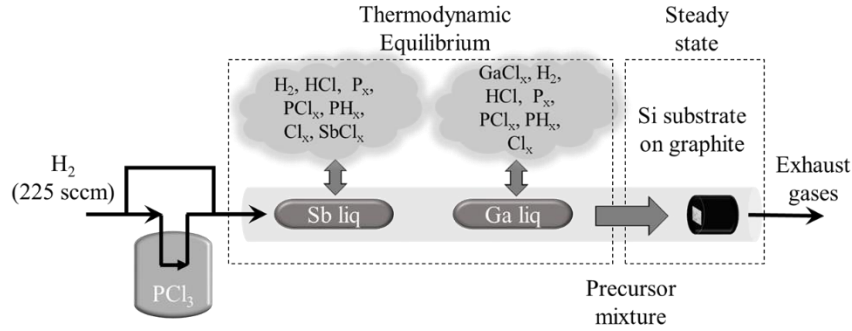


Figure 3.1 Schematic of the experimental setup illustrating two zones: first zone in which precursor generation occurs at gas-solid/liquid equilibrium and second zone in which precursor composition is under steady state condition through gas and gas-solid kinetics.

3.1.2. Thermodynamic Modeling and Simulation

There have been several modeling and experimental studies to understand the HVPE growth. Most of them have focused on direct measurements of the gaseous species and how the results compare with the equilibrium composition based on thermodynamic calculations. It is of general consensus that the group III element is transported by halide species while the group V element is mostly stable as hydrides, a diatomic or tetratomic molecules³⁷.

Hong and Lee used the law of mass action for a simple reaction set to propose an “intrinsic growth” rate of GaAs and then used boundary layer thickness to account for the mass transport effects³⁸. Mimila and Arroyo proposed a very interesting approach with a single reaction of the III element to form the transporting species, and the same reaction in the reverse direction occurring at the substrate, based on activity coefficients that are different in each surface. The effect of the V element species was introduced by the effect its partial pressure has on the activity coefficient of the III element containing species at the substrate surface. This model was validated with GaAs, GaP, InP and InAs growth.³⁹

Hollan et al.⁴⁰ Developed a growth rate based on partition functions and surface coverage coefficients for the deposition of GaAs through a simplified reaction mechanism where GaCl reacts with hydrogen and arsenide to produce gallium arsenide and hydrochloric acid. Veuhoff et al.⁴¹ proposed growth rate models accounting for transport of the species in the bulk phase, diffusion from the bulk to the surface, adsorption of the species on the surface and subsequent reactions governed by the activated-complex theory, also for the growth of GaAs.

All studies agree that the temperature dependence of the growth rate shows two distinctive regions as described in the work by Shaw.⁴² At low temperature, the adsorption/desorption of species on the substrate is the determining step and the growth is kinetically limited, then the growth rate reaches a maximum value and further increase in the temperature causes the growth rate to decrease because the species react faster than they are transported in the bulk gas and it is therefore called the mass transfer limited regime. Low system pressures can diminish the substrate temperature effect and increase the film homogeneity because it enhances the transport of species,⁴¹ contrary to increasing the inert gas content which causes the opposite effect.⁴³ Finally, it is also widely accepted that the growth rate is proportional to the partial pressure of group-V species and an excess of group-III species blocks the substrate surface sites decreasing the growth rate.⁴⁴

Computational modeling of the HVPE reactor is done by dividing the reactor into two zones: first zone in which metals react with halides to form precursors and second zone where the precursors interact with substrate and deposit films. In the first zone, gas-solid/liquid equilibrium is assumed for determining the gas phase composition. In the second zone, steady state composition is determined using gas phase and gas-solid chemical kinetics. This is schematically represented in Figure 1.

The theoretical calculations were done using the software Chemkin Pro 18.1. First the equilibrium composition in zone 1 was determined by the Gibbs free energy minimization method considering an initial mixture of liquid gallium, antimony powder, hydrogen and phosphorous trichloride. In the equilibrium analysis, twenty-one possible species including hydrides and halides such as, GaCl, GaCl₂, GaCl₃, Ga₂Cl₄, Ga₂Cl₆, GaH, GaH₂, GaH₃, PCl, PCl₂, PH, PH₂, PH₃, as well as P, P₂, P₄, H, Cl, Cl₂, HCl and gaseous Ga, were considered. The required thermodynamic data was obtained from Janaf tables and NASA Thermobuild databases. Any other required input was matched with the conditions used experimentally, i.e. 250 and 500 torr, 1.2L, 3.05*10⁻² moles of H₂, 2.92*10⁻³ moles of PCl₃, 1.43*10⁻¹ moles of gallium and 4.11*10⁻² moles of antimony.

The equilibrium composition was used as the input for zone 2 (film deposition) as shown in Figure 3.1 and subsequently the steady state composition was determined for different temperature values matching the range used experimentally. Solid gallium phosphide formation was considered to take place both at the gallium boat driven by reactions between gaseous species and the gallium; as well as at the silicon substrate where gallium halides are transported. The compilation of kinetic parameters is shown in Table 3.1 Table 3.3. The steady-state concentrations required solving the general mass balance.

$$\frac{d}{dt}(\rho V) = \sum_{i=1}^{N_{inlet}} \dot{m}^* - \sum_{i=1}^{N_{outlet}} \dot{m} + \sum_{m=1}^M A_m \sum_{k=1}^{K_g} \dot{S}_{k,m} W_k \quad \text{Equation 2}$$

$$\frac{d}{dt}(\rho V) = \sum_{i=1}^{N_{inlet}} \dot{m}^* - \sum_{i=1}^{N_{outlet}} \dot{m} + \sum_{m=1}^M A_m \sum_{k=1}^{K_g} \dot{S}_{k,m} W_k \quad \text{Equation 3}$$

Where ρ is the mass density, V is the reactor volume, \dot{m}^* and \dot{m} are the inlet and outlet mass flow rates. A_m is the surface area of the mth material. M and K_g are the total

number of materials and gas species respectively. \dot{S}_k is the molar production rate of k^{th} species and is given by

$$\dot{S}_k = \sum_{i=1}^I \nu_{ki} q_i \quad \text{Equation 4}$$

$$\dot{S}_k = \sum_{i=1}^I \nu_{ki} q_i \quad \text{Equation 5}$$

The model considers reversible chemical reactions:



$$\text{where } \nu_{ki} = \nu''_{ki} - \nu'_{ki} \quad \text{Equation 7}$$

ν_{ki} are the stoichiometric coefficients and X_k are the chemical symbols of the k^{th} species. The rate of progress for the i^{th} reaction, q_i , is given by the difference of the forward and reverse rates:

$$q_i = k_{if} \prod_{k=1}^K [X_k]^{\nu'_{ki}} - k_{ir} \prod_{k=1}^K [X_k]^{\nu''_{ki}} \quad \text{Equation 8}$$

k_i is the rate constant for the i^{th} reaction and follows an Arrhenius type of dependence with the temperature:

$$k_i = A_i T^{\beta_i} \exp\left(-E_i/R_C T\right) \quad \text{Equation 9}$$

Where A_i is the pre-exponential factor, β_i is the temperature exponent and E_i is the activation energy.

Table 3.1 Gas Phase reactions

| | | A_i (mole cm ⁻³) | β_i | E_i (kcal mole ⁻¹) | Ref. |
|------|--|-----------------------------------|-----------|-------------------------------------|------|
| G.1 | $\text{GaCl} + \text{Cl}_2 \leftrightarrow \text{GaCl}_3$ | $1.7 \cdot 10^{-12}$ | 0.690 | $8.55 \cdot 10^4$ | 45 |
| G.2 | $0.5\text{H}_2 + 0.5\text{Cl}_2 \leftrightarrow \text{HCl}$ | $1.51 \cdot 10^{-1}$ | -0.713 | $2.08 \cdot 10^4$ | 45 |
| G.3 | $\text{GaCl}_3 + \text{H}_2 \leftrightarrow \text{GaCl} + 2\text{HCl}$ | $2.21 \cdot 10^{10}$ | -2.116 | $-4.38 \cdot 10^4$ | 45 |
| G.4 | $\text{P}_4 \leftrightarrow 2\text{P}_2$ | $7.56 \cdot 10^7$ | -1.150 | $-5.53 \cdot 10^4$ | 45 |
| G.5 | $0.25\text{P}_4 + 1.5\text{H}_2 \leftrightarrow \text{PH}_3$ | $1.84 \cdot 10^1$ | -2.760 | $6.72 \cdot 10^3$ | 45 |
| G.6 | $0.25\text{P}_4 + 1.5\text{Cl}_2 \leftrightarrow \text{PCl}_3$ | $1.54 \cdot 10^{-6}$ | 0.575 | $8.18 \cdot 10^4$ | 45 |
| G.7 | $\text{Ga}_2\text{Cl}_6 \leftrightarrow 2\text{GaCl}_3$ | $1.61 \cdot 10^9$ | 0.000 | $8.18 \cdot 10^4$ | 46 |
| G.8 | $\text{Ga}_2\text{Cl}_4 \leftrightarrow \text{GaCl}_3 + \text{GaCl}$ | $4.83 \cdot 10^2$ | 0.000 | $-2.10 \cdot 10^4$ | 46 |
| G.9 | $\text{PH}_3 \leftrightarrow \text{PH} + \text{H}_2$ | $7.55 \cdot 10^{-4}$ | 0.000 | $7.36 \cdot 10^4$ | |
| G.10 | $\text{PH} \leftrightarrow 0.5\text{P}_2 + 0.5\text{H}_2$ | $7.092 \cdot 10^{-6}$ | 0.000 | $6.93 \cdot 10^4$ | |
| G.11 | $\text{PCl}_3 + \text{H} \leftrightarrow \text{HCl} + \text{PCl}_2$ | $2.41 \cdot 10^{-20}$ | 0.000 | 0.00 | 47 |
| G.12 | $2\text{H}_2 \leftrightarrow 2\text{H} + \text{H}_2$ | $9.04 \cdot 10^3$ | 0.000 | 0.00 | 48 |
| G.13 | $\text{P} + \text{Cl}_2 \leftrightarrow \text{PCl} + \text{Cl}$ | $3.90 \cdot 10^{-20}$ | 0.000 | 0.00 | 47 |
| G.14 | $\text{PCl}_3 + \text{P} \leftrightarrow \text{PCl}_2 + \text{PCl}$ | $2.51 \cdot 10^{-19}$ | 0.000 | 0.00 | 47 |
| G.15 | $\text{P} + \text{H}_2 \leftrightarrow \text{PH}_2$ | $5.00 \cdot 10^{-23}$ | 0.000 | 0.00 | 47 |
| G.16 | $\text{Cl} + \text{Cl} \leftrightarrow \text{Cl}_2$ | $5.51 \cdot 10^{-42}$ | 0.000 | 0.00 | 47 |
| G.17 | $\text{PH}_3 + \text{Cl} \leftrightarrow \text{HCl} + \text{PH}_2$ | $2.20 \cdot 10^{-31}$ | 0.000 | 0.00 | 47 |
| G.18 | $\text{H}_2 + \text{Cl} \leftrightarrow \text{HCl} + \text{H}$ | $2.44 \cdot 10^{-20}$ | 0.000 | 0.00 | 47 |

Table 3.2 Surface reactions at the gallium boat

| | | A_i (mole cm ⁻³) | β_i | E_i (kcal mole ⁻¹) | Ref. |
|-----|--|-----------------------------------|-----------|-------------------------------------|------|
| B.1 | Ga+0.5Cl ₂ ⇌GaCl | 6.98*10 ¹⁰ | -1.081 | 1.69*10 ⁴ | 45 |
| B.2 | Ga+1.5Cl ₂ ⇌GaCl ₃ | 2.71*10 ² | -0.391 | 1.03*10 ⁵ | 45 |
| B.3 | GaCl ₃ +2Ga⇌3GaCl | 2.93*10 ²⁵ | -2.829 | -5.16*10 ⁴ | 45 |
| B.4 | Ga+0.5P ₂ ⇌GaP | 1.09*10 ⁻¹ | 0.000 | 4.30*10 ⁴ | 45 |
| B.5 | Ga+0.25P ₄ ⇌GaP | 8.59*10 ¹ | -0.299 | 2.29*10 ⁴ | 45 |
| B.6 | Ga+HCl⇌GaCl+0.5H ₂ | 1.14*10 ⁸ | -0.368 | -3.98*10 ³ | 49 |

Table 3.3 Surface reactions at the silicon substrate

| | | A_i (mole cm ⁻³) | β_i | E_i (kcal mole ⁻¹) | Ref. |
|-----|---|-----------------------------------|-----------|-------------------------------------|------|
| S.1 | 2GaCl+0.5P ₄ ⇌2GaP+Cl ₂ | 2.58 | 1.564 | 2.46*10 ⁴ | 45 |
| S.2 | 3GaCl+0.5P ₄ ⇌2GaP+GaCl ₃ | 9.14*10 ⁻⁹ | 2.254 | 1.10*10 ⁵ | 45 |
| S.3 | GaCl+0.25P ₄ +0.5H ₂ ⇌GaP+HCl | 2.08*10 ¹² | 0.069 | 3.32*10 ⁴ | 45 |

3.2. Plasma-Assisted Vapor Liquid Phase Epitaxy (PA-VLPE)

The experimental setup used to obtain results of CHAPTER SIX is illustrated in Figure 3.2 (setup used in CHAPTER FIVE is similar but details are described elsewhere).³⁰

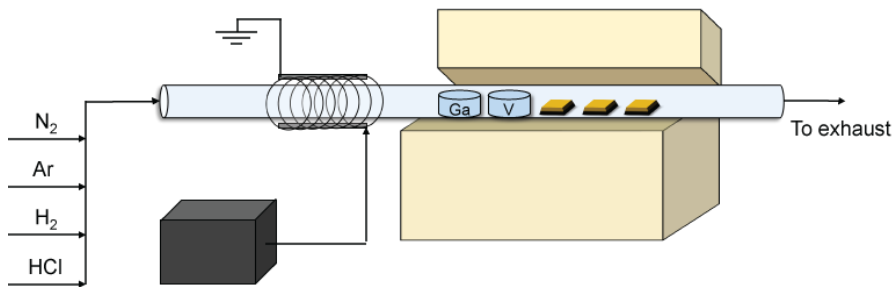


Figure 3.2 Experimental setup (gases, radio frequency plasma source and furnace)

Four different gases can be fed to the system (N_2 , Ar, H_2 and HCl) and the flow rates are controlled by MKS mass flow controllers. Hydrochloric acid was purchased from Sigma Aldrich as well as solid gallium and antimony. Substrates were gold and copper-coated in a Trovato evaporator (not depicted in Figure 3.2). The radio-frequency plasma system included a power supply (R601), and a matching network (MC2-5382, AT6-009) purchased from Seren IPS.

3.3. Materials Characterization Techniques

3.3.1. Electrochemical Measurements

The electrochemical measurements were performed with a Metrohm potentiostat/galvanostat (PGSTAT204 with a compliance voltage of 20 V and a maximum current of 400 mA or 10 A), in a 3-electrode configuration (unless stated otherwise), using a platinum mesh counter electrode, a Ag/AgCl reference electrode and $Ga(Sb \text{ or } Bi)_xN_{1-x}$ or $GaSb_2P_{1-z}$ working electrodes. The electrochemical cell had a capacity of 100 mL and was equipped with a quartz window. 1 M sulfuric acid solution was the electrolyte used to conduct the measurements. A Newport solar simulator (300 W arc lamp, AM 1.5 filter, IR filter) was used on its own or coupled with a monochromator for the photocurrent spectroscopy measurements. A 470nm LED was also used for some of the

photoelectrochemical measurements. Reported irradiance values of the different light sources were measured with a calibrated silicon photodiode purchased from Thorlabs.

3.3.2.Uv-Vis Spectroscopy

Diffuse reflectance measurements were carried out with a PerkinElmer Lambda950 spectrometer equipped with a 60 mm integrating sphere. Scans covered the range between 850 to 300 nm with 1 nm intervals.

3.3.3.X-ray Diffraction

A Bruker Discovery D8 HR-x-ray diffractometer equipped with a Cu K α source and LynxEye(TM) detector, was used to perform the x-ray diffraction scans in a 2θ range between 20 to 90 degrees at a rate of 0.05 seconds/step. The software EVA 2.0 (ICCD PDF-2) enabled crystal structure matching and scans background subtraction.

3.3.4.Scanning and Transmission Electron Microscopy

Transmission Electron Micrographs were acquired using 200-kV FEI Tecnai F20 FEG-TEM/STEM (transmission electron microscope/scanning TEM). Scanning Electron Micrographs were acquired with FEI Nova600 FEG-SEM and TESCAN Vega3 SEM and microscopes. Typical image acquisition settings for Scanning Electron Micrographs were a working distance of 5 mm or less, 10 to 20 keV, spot size 4 and magnification between $(10 \times 10^3)x$ to $(25 \times 10^3)x$.

3.3.5.Raman and Photoluminescence Spectroscopy

Photoluminescence measurements were acquired with a Renishaw inVia confocal Raman/PL microscope system, using a 325-nm laser, 1200 mm⁻¹ grating, exposure time

of 10 s and a minimum of 10 accumulations, at room temperature or at $-196\text{ }^{\circ}\text{C}$ with the aid of a Linkam cooling stage (THMS 600).

4. CHAPTER FOUR

GaSb_zP_{1-z} THROUGH HALIDE VAPOR PHASE EPITAXY

4.1. Introduction

In section 2.1.2 it was explained how the elevated temperatures needed to grow epitaxial films in vapor-solid synthesis techniques can become a challenge for the obtention of high incorporation fractions in ternary III-V alloys. The available HVPE setup for the synthesis of GaSb_zP_{1-z} alloys does not allow an independent control of key V-group species, since generation of SbCl depends on the PCl₃ flow rate. Therefore, it is particularly important to map the experimental conditions (temperatures, pressure, flow rates, etc) that promote high concentrations of substitutional anion species SbCl in the same order of magnitude as competing P₂ and P₄ species.

Process conditions mapping usually involves modelling approaches. Despite the available literature on HVPE modeling, the reported approaches focus either on precursor formation or on surface kinetics but not on both aspects, use limited reaction sets, and were developed for well-established III-V materials.

In this study, a simple methodology for the computational modeling of HVPE reactors was developed, where precursors are formed by means of vapor-liquid/solid reactions in the first zone and then transported to a second zone where the film grows. The growth of films in the second zone was modeled using a comprehensive gas phase and gas-surface reaction sets. The described first and second zones refer to Figure 3.1.

The simulations results helped identify key growth species and were used to design and conduct the synthesis of GaSb_zP_{1-z} at high substrate temperatures (>725C)

resulting in antimony incorporation fraction “z” of up to 6.7 at%. Good agreement between predicted and experimental $\text{GaSb}_z\text{P}_{1-z}$ alloys growth rates was found. Finally, the morphologic, crystallographic, optoelectronic, and photo-electrochemical properties of the grown $\text{GaSb}_z\text{P}_{1-z}$ alloys were evaluated as explained in section 3.3.

4.2. Thermodynamic Modeling and Simulation of HVPE-grown $\text{GaSb}_z\text{P}_{1-z}$ Alloys

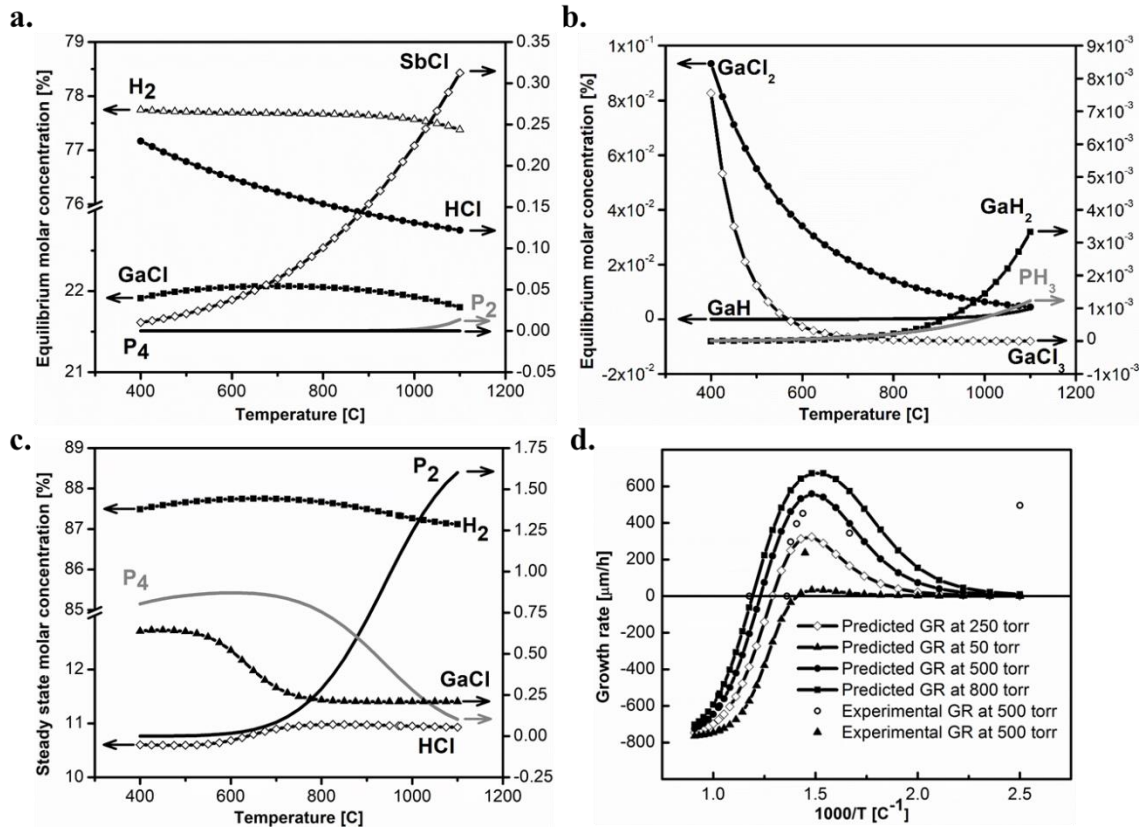


Figure 4.1. **a.** Most abundant gaseous species in zone 1 under thermodynamic equilibrium, **b.** Less abundant gaseous species in zone 1 under thermodynamic equilibrium, **c.** Most abundant gaseous species in zone 2 under steady state conditions, **d.** Film growth rate versus inverse temperature of the substrate.

Computational results of equilibrium composition in zone 1 (refer to Figure 3.1) are shown in Figure 4.1a&b. Hydrogen molecule is by far the most abundant species due to

its thermodynamic stability and its initial excess relative to other species in the feed. GaCl also shows high stability as well as SbCl and HCl. The percentage of P₂ and P₄ is two orders of magnitude lower but these are the most stable of the phosphorous containing species. Both y-axes in Figure 4.1a-c represent the molar concentrations of the species.

GaCl₂, GaCl₃, GaH, GaH₂ and PH₃ are also present throughout the whole temperature range in the order of 10⁻²-10⁻³ molar percentages. All other hydride species considered in this study PH, PH₂ and GaH₃, exhibit low relative abundance values. Particularly the absence of gallium hydrides can be explained by the claims that III group element hydrides dissociate into their constituting elements at near ambient temperatures.⁵⁰

Other species such as the phosphorous halides PCl, PCl₂, PCl₃ as well as Cl, Cl₂ and P, have negligible concentration values, observations that are supported by several studies with similar systems.^{49,51} For example, thermodynamic computations for the GaAs, H₂ and Cl system between 800-1200 K, established that among the species of interest for this study, only Ga, GaCl₃, GaCl, HCl, H₂, Cl₂ are present in important amounts contrary to Cl and GaCl₂.⁵² The equilibrium calculations of the Cl + GaP system predict that in a range of 1000-1200 K the most abundant gaseous species are GaCl, P₄, P₂, GaCl₃, while Ga₂Cl₂, Ga₂Cl₄, GaCl₂, Ga₂Cl₆, PCl, PCl₃ and Cl are present in lower orders of magnitude.⁵³ Ga₂Cl₂ and Ga₂Cl₆ were found to have negligible presence throughout the studied temperature range, a result in agreement with Raman spectral observations conducted in gaseous mixtures of Ga and Cl containing species under the studied conditions (700-785 K)⁵⁴ and therefore these species were not considered in the present study.

One of the major discrepancies of our results with the ones found in the literature is that even though P₂ and P₄ are present, their amounts are not significant when compared to other species, while the theoretical calculations by Klima⁵¹ of the Ga-PCl₃-H₂ system, and by Seki⁵⁵ for a system of H₂ and a chloride source over GaP (powder) to form

a GaP film, yielded that up to 850 °C P_4 is a predominant species, and at temperatures higher than 900 °C, P_2 becomes significant. In the deposition of GaAsP films modeled by Bleicher⁴⁹ under temperature conditions similar to the ones of the present study, PH_3 was found to have comparable partial pressures to P_2 , coinciding with our results.

The equilibrium composition along with flow rates were used as input for zone 2 (refer to Figure 3.1). Using the reaction set of homogeneous and heterogeneous reactions,⁵⁶ steady state compositions were obtained at various substrate temperatures. When the steady state composition is compared to the one under thermodynamic equilibrium, most of the species are supersaturated except GaCl particularly at high temperatures; implying thermodynamic constraints are also significant. Furthermore, the used kinetic model also suggests GaCl is the limiting reagent (see reactions S.1-S.3 of Table 3.3).

Other species with significant presence at the deposition zone under steady state conditions, are shown in Figure 2c. Hydrogen is very abundant in this case, as well as hydrochloric acid, even reaching supersaturation conditions which causes acid condensation. At low temperatures P_4 has significant concentrations and at high temperatures P_2 increases as a result of P_4 decomposition.

Regarding the effect of V/III ratio on the growth rate, several studies have reported that HCl and GaCl have higher adsorption coefficients than V species and therefore increasing the partial pressure of the latter, normally causes the growth rate to increase.⁴⁴ Despite the fact our model considers only kinetic and not adsorption effects, it coincides with the literature reports in the region below 650 °C, as the V/III ratio increases, so does the growth rate. A further increase in the temperature results in higher V/III ratios but under those conditions GaCl becomes the limiting reactant as stated before. It was not possible to evaluate the effect of the V/III ratio experimentally because the employed setup uses PCl_3 as the source for V species and HCl. As discussed previously Gallium halides are

the major transport mechanism of III species making both variables, V and III species concentrations dependent on each other.

Figure 4.1d shows the dependence of the gallium antimonide phosphide growth rate with the inverse of the substrate temperature at four different pressures. The curves represent the predicted values from 800 to 50 torr and the scattered points correspond to the experimental samples obtained at 500 and 250 torr. For all pressure conditions, the increase in the temperature is reflected in higher growth rates, implying the process is kinetically driven. After reaching a maximum the growth rate decreases, a phenomenon widely observed in CVD literature and summarized by Shaw,⁴² which is attributed to transport limitations of the species in the bulk of the gas. In our case the decrease in the growth rate can be explained by the decrease in the concentration of GaCl and P₄, however, the fact that the experimental values are lower than the ones predicted by the model is an indication of mass transport limitations. The difference between the measured and predicted growth rates could also be attributed to uncertainties in the reported experimental values because ramp up and shut down periods were not considered as growth time. At 400 °C (1000/T=2.5) the obtained film was very thick but mostly composed of agglomerated particles (see Figure 4.2a) that probably nucleated in the gas phase close to the substrate, a phenomenon not considered in the simulation. For more details on the experimental growth conditions of GaSb_zP_{1-z} alloys refer to section 3.1.1.

The closest reference we can compare to in the literature is gallium phosphide. The results of Seki and Araki⁵⁵ suggest that the relative concentration of GaP under thermodynamic equilibrium increases at higher temperatures but it is worth noting their calculations are not based on Gibbs free energy minimization, instead the authors use the partial pressures as function of temperature and calculate equilibrium constants for the main possible reactions between the available species. This result is contradicted by another theoretical study⁵¹ in which although GaP is stable in the temperature range

between 600-840 °C, its mole fraction decreases with temperature, coinciding with the results of this study. Surprisingly, Bleicher⁴⁹ shows that solid GaP is stable in the narrow studied temperature range between 1000-1150 K, but its mole fraction doesn't show a strong dependence with the temperature.

4.3. GaSb_zP_{1-z} Alloys Growth and Characterization

4.3.1. Effect of the Substrate Temperature on Antimony Incorporation and Crystalline Quality of the Films

As explained in section 2.1.1, GaSb_yP_{1-z} alloys are good photoanode candidates for Water Splitting. It is hypothesized their photoelectrochemical performance will improve alongside with their crystalline quality and the latter requires an increase in the substrate temperature. It is well known high temperatures promote an enhancement of species surface diffusion and therefore nucleation islands coalesce with each other at initial stages of the growth producing good crystalline quality films.

The experimental setup for the growth of GaSb_zP_{1-z} alloys is shown in Figure 3.1 and consists of a quartz tube with a volume of 1.2 L, fitted in a two-zone furnace and equipped with an additional zone for inductively heating a graphite susceptor where the 111 silicon substrate was held. The reactor is coupled to two gas lines that mix before the entrance and carry 125 sccm of pure hydrogen and 100 sccm of hydrogen that has been previously flown through a bubbler containing phosphorous trichloride, maintained at a constant temperature of 35 °C. In each of the furnace zones quartz boats are placed, the first with 5 g of antimony powder and the second with 10 g of gallium. The pressure inside the reactor was 500 torr and the antimony and gallium zones were kept at 750 °C and 970 °C respectively. The substrate temperature was varied between 400 °C and 725 °C.

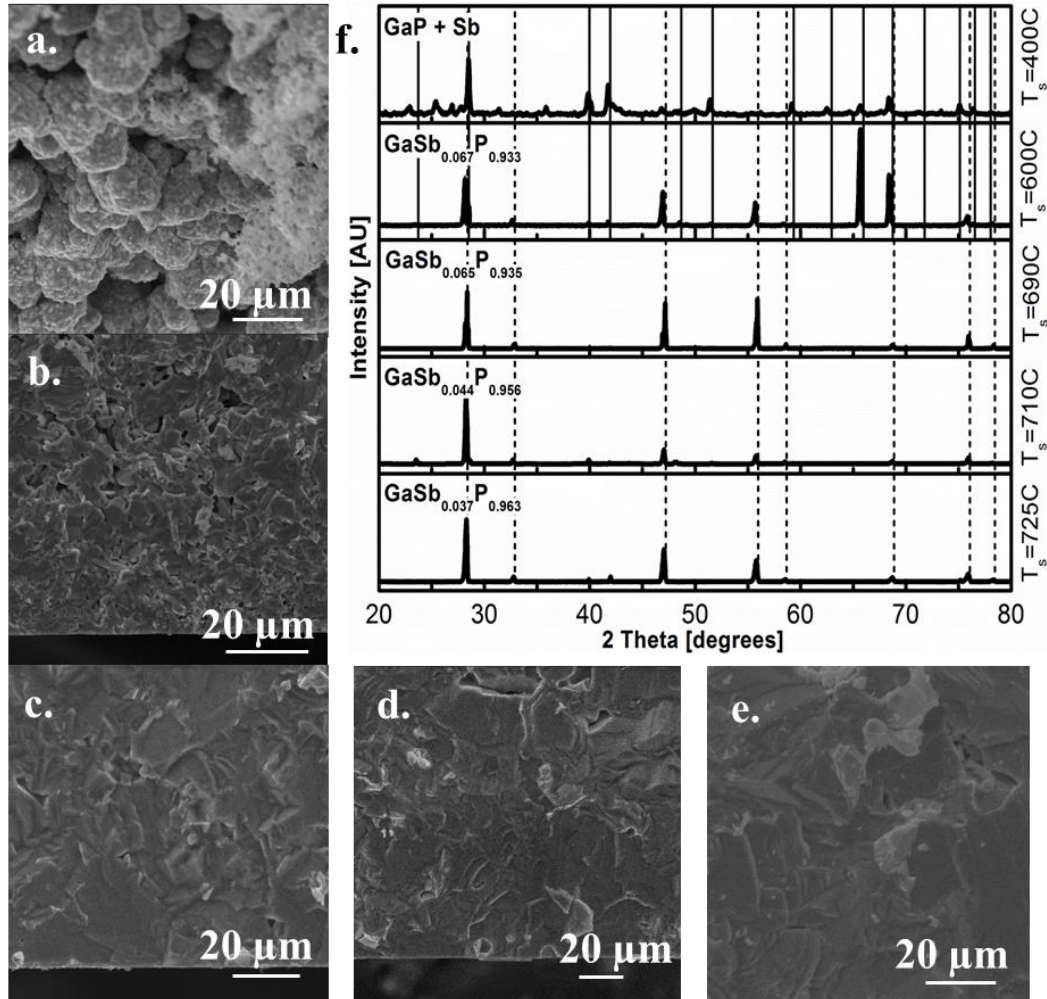


Figure 4.2 Cross sectional SEM images of free standing $\text{GaSb}_z\text{P}_{1-z}$ films grown at different substrate temperatures: a. 400 °C, b. 600 °C, c. 690 °C, d. 710 °C, e. 725 °C and f. X-ray spectra of the samples grown at substrate temperatures between 400 °C and 725 °C. Grey dashed and black lines correspond to pure GaP (PDF-00-012-0191) and Sb (PDF-00-001-0802) spectra, respectively.

As seen in Figure 4.2, Increasing the substrate temperature had a positive effect in the crystal quality of the film which can be attributed to an increased surface diffusion of the impinging species and/or faster lateral growth rate that allows the nucleation islands to coalesce, less voids and grain boundaries can be observed for the higher substrate temperature samples. The XRD spectra also confirms the higher purity of the phase, and

the growth orientation is preferential towards [111] plane as its intensity is higher compared to the other peaks, and the ratio of [111] to each of the other planes increases with substrate temperature except for the sample grown at 725 °C. It can be observed the peaks are shifted to lower angles versus the pure GaP spectrum, indicating an increase in the lattice parameter. The shift magnitude was employed to estimate the degree of antimony incorporation using Vegard's Law. At low substrate temperature the degree of Antimony incorporation was the highest and even pure Sb peaks were evidenced. An increase in the temperature causes a decrease in the incorporation probably due to desorption of the antimony precursors from the substrate, pointing out the major limitation of the used setup/recipe for the synthesis of $\text{GaSb}_z\text{P}_{1-z}$ alloys with high antimony content.

4.3.2. Optoelectronic Properties and Photoelectrochemical Performance

From diffuse reflectance measurements (Figure 4.3), it can be observed that the alloys exhibit direct energy transitions between 2.4 -2.5 eV, confirming a decrease of the direct energy transition at 2.68 eV of pure GaP. Energy transitions below 2.0 eV were disregarded since they have been described as “exponential tails” that lead to bandgap underestimation.⁵⁷ Figure 4. 4 helps illustrate band gap differences caused by the alloying. While

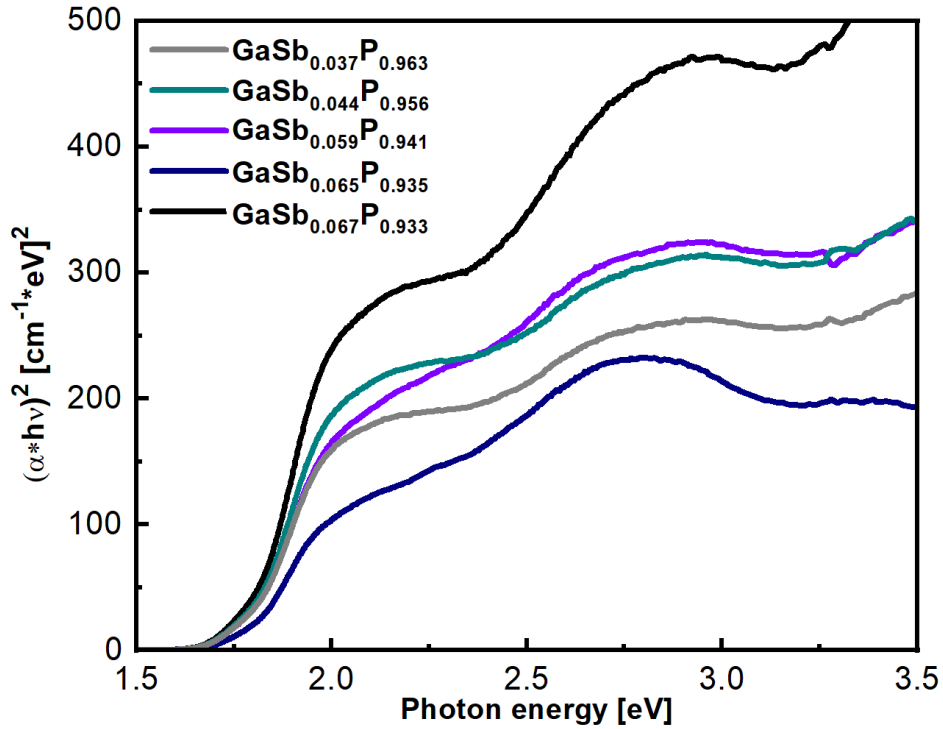


Figure 4.3 Direct Tauc plots from diffuse reflectance measurements of 5 GaSb_zP_{1-z} films grown between 600 and 725 °C with different Sb incorporation levels

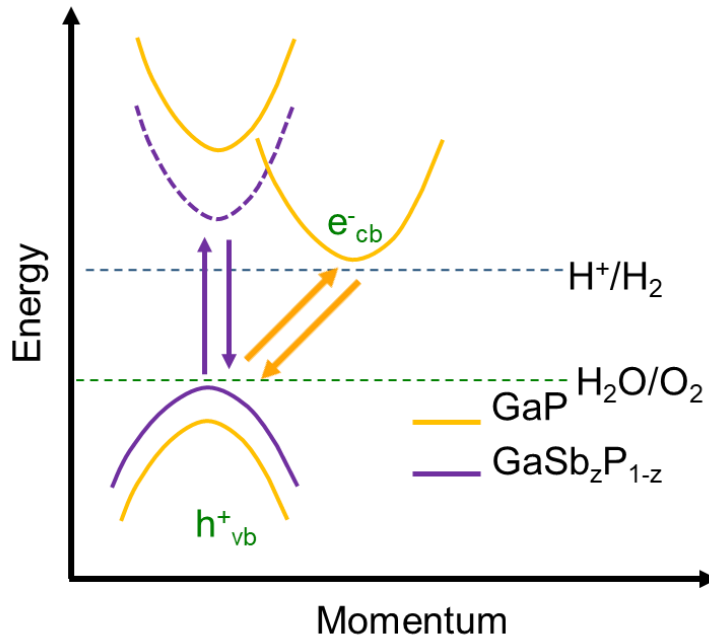


Figure 4. 4 GaP and GaSb_zP_{1-z} band structure schematic

Photoelectrochemical measurements were performed in 1M H₂SO₄ using a 3-electrode setup including an Ag/AgCl reference electrode and a platinum mesh counter electrode. The different levels of irradiance for the experiments with a solar simulator and a 470nm LED were measured using a calibrated silicon photodiode immersed in the electrolyte in the same position working electrodes were placed.

Figure 4.5 shows chronopotentiometry and Linear Sweep Voltammetry measurements of the same alloys under 6 sun full spectrum illumination. The potential under illumination condition switched to more negative values indicating an n-type conductivity and their conduction band edge as estimated from the potential value under illumination became more negative as the antimony level increased. The higher antimony content alloys also show slower response to the changes in illumination, i.e. the steps are less flat, indicating charge transport deficiencies. However, this observation can also be related to the worse crystalline quality of these samples grown at lower substrate temperatures.

Figure 4.6a shows the linear sweep voltammeteries under intermittent 470nm LED illumination corresponding to an irradiance of 506 mW*cm⁻². Once more the GaSb_zP_{1-z} alloys show significantly higher current densities at lower applied biases compared to the commercial sulfur-doped GaP. The performance differences among the alloys can be attributed to the crystallinity variations but in the case of the two alloys grown at 710°C with 4.4 and 5.9 at% antimony incorporation, the measurements suggest a better performance of the sample with less antimony. Electrochemical impedance spectroscopy (EIS) measurements were performed at 506 mW*cm⁻² (470nm LED) and 0V RHE for sulfur-doped GaP and GaSb_zP_{1-z} photoanodes.

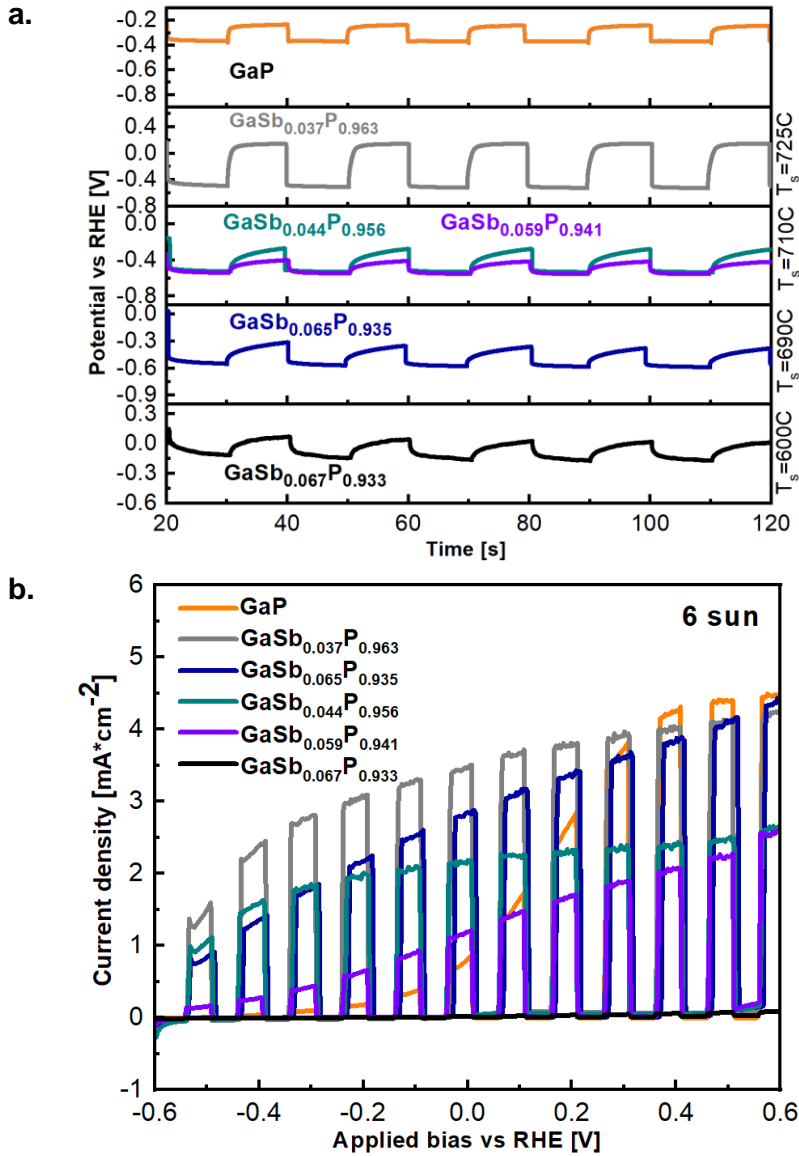


Figure 4.5 a. Chronopotentiometry measurements under intermittent 6 sun (full spectrum) and at a current of 0 A. b Linear Sweep Voltammetries under 6 sun (full spectrum) for GaSb_zP_{1-z} photoanodes with different Sb incorporation levels compared to a commercial sulfur-doped GaP wafer

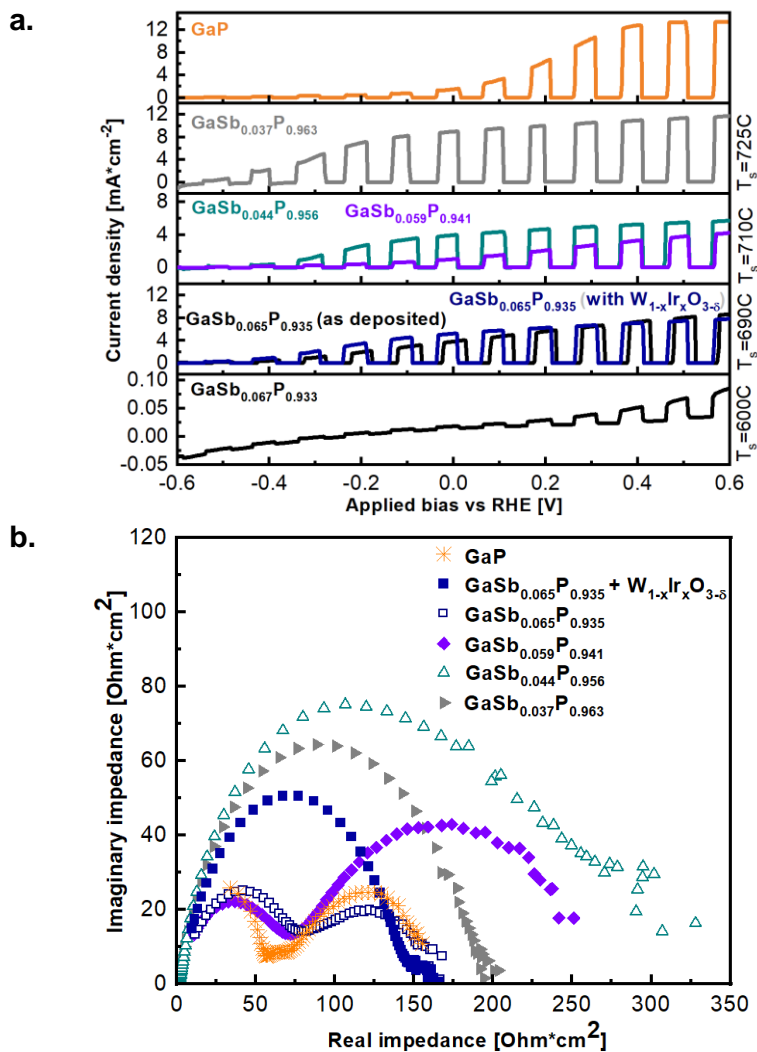


Figure 4.6 a. Linear Sweep Voltammeteries under intermittent 470nm LED illumination (506 mW*cm⁻²) for GaSb_zP_{1-z} photoanodes with different Sb incorporation levels compared to a commercial sulfur-doped GaP wafer. b. Impedance spectroscopy measurements at 0V vs RHE of the GaSb_yP_{1-y} photoanodes compared to a sulfur-doped GaP wafer and an Ir_xWO_{3-x} co-catalyzed GaSb_yP_{1-y} alloy, under a 470nm LED illumination of (506 mW*cm⁻²).

The Nyquist plots in Figure 4.6b indicate the presence of two semicircles for the sulfur-doped GaP, GaSb_{0.059}P_{0.941} and GaSb_{0.065}P_{0.935} electrodes. The semicircle located at lower resistances and high frequencies is attributed to the charge transfer

process in the depletion zone meanwhile the semicircle at low frequencies is related with minority carrier charge transfer and recombination at the semiconductor-electrolyte interface.⁵⁸ Here the relatively large second semicircles indicate low charge transfer efficiencies explaining the corresponding low photocurrent values at 0V RHE in the case of the sulfur-doped GaP, GaSb_{0.059}P_{0.941} and GaSb_{0.065}P_{0.935} electrodes the relatively large second semicircles indicate low charge transfer efficiencies and could explain the low photocurrents observed in Figure 4.5b for the samples at 0V RHE. On the other hand, at the same applied bias the GaSb_{0.044}P_{0.956} and GaSb_{0.037}P_{0.963} materials exhibit only one clear semicircle and a better performance which is consistent with the fact that for these electrodes the operating point is closer to the current saturation plateau where the transfer efficiency reaches its maximum. These results suggest that a controlled antimony concentration in the alloy can increase the charge injection from the valence band, however an excess of antimony can generate surface states in the alloy that lead to surface charge carrier recombination.

From the photoelectrochemical and impedance results of GaSb_zP_{1-z} alloys it is hypothesized the system might exhibit antimony segregation that causes the higher antimony containing samples to show charge transport issues. It is also possible that antimony is adsorbing onto the substrate as a monoatomic species in higher proportion than as SbCl and that the monoatomic species incorporation kinetics is not favorable. More research is needed to understand the Halide Vapor Phase Epitaxy Mechanisms, in order to synthesize GaSb_zP_{1-z} alloys with high antimony incorporation that would result in a direct bandgap between 1.7eV to 2.0eV, while enhancing the crystalline quality simultaneously.

The current chemistry used in our HVPE setup uses PCl₃ carried by H₂ that flows over Sb and Ga solid sources producing mainly GaCl, SbCl, P₂ and P₄ species that react to form GaSb_yP_{1-y}. The gas phase concentration of anion species Sb and P that compete

for available surface sites to adsorb onto, cannot be controlled independently (increasing PCl_3 to produce more SbCl will also result in higher P_2/P_4 partial pressures).

4.4. Summary

A thermodynamic and kinetic model for the $\text{GaSb}_z\text{P}_{1-z}$ growth through Halide Vapor Phase Epitaxy was developed in Chemkin Pro. This model was instrumental to understand the correlation between experimental conditions and alloys properties and growth mechanisms.

Optical, crystallographic and photoelectrochemical properties of as-deposited and $\text{Ir}_x\text{WO}_{3-x}$ decorated $\text{GaSb}_z\text{P}_{1-z}$ alloys were compared to sulfur-doped GaP. The results suggest as-deposited $\text{GaSb}_z\text{P}_{1-z}$ alloys have an improved catalytic performance when compared with GaP but will benefit from larger substitutional anion incorporation that will lead to larger bandgap reduction and more efficient light absorption.

5. CHAPTER FIVE

DILUTE ANION ALLOYED, $\text{GaSb}_x\text{N}_{1-x}$ AND $\text{GaBi}_y\text{N}_{1-y}$ FILM SYNTHESIS THROUGH PLASMA ASSISTED VAPOR LIQUID PHASE EPITAXY

5.1. Introduction

Dilute anion alloying into III-Nitrides is of interest for exploring materials with band gap and band edge engineering. Reports have shown that dilute ternary alloys for the $\text{GaN}_x\text{Sb}_{1-x}$ system for even a very small y value exhibit band gap bowing from that of GaSb and extend to negative band gaps for composition in excess of about 8% N.⁵⁹ Following the same line of thought, the optoelectronic properties of GaN were expected to change with small amounts of anions such as antimony. Initial experimental reports show that substitutional alloying with antimony can produce visible light absorbing alloys.⁶⁰ However, there are some contradictions in the literature about how band gap bowing occurs from 3.45 to 2 eV and at what concentrations of Sb. Sheets et al⁶⁰ predicted a band-gap value of 2 eV for incorporation fractions $0.05 < x < 0.06$. Later on, Andriotis et al.⁶¹ theoretically determined that antimony incorporation fractions as low as 0.02 could indeed produce $\text{GaSb}_x\text{N}_{1-x}$ alloys with direct 1.8 eV band gap. More recently, Chowdhury et al.²⁹ claimed it was possible obtain $\text{GaSb}_x\text{N}_{1-x}$ alloys with continuous band gap reduction versus pure GaN with antimony incorporation fractions x , below 0.01. A critical examination of the latter study reveals possible misinterpretation of photoluminescence results where defect recombination emission is presented as bandgap emission. To understand the true band gap and band edge engineering potential of dilute $\text{GaSb}_x\text{N}_{1-x}$ alloys it is necessary to conduct further experimental and theoretical research.

The synthesis of III-Nitrides is another major challenge, GaN growth is especially intricate due to the strong bond between Ga and N and because in a solution of these two elements, gaseous nitrogen is thermodynamically favored versus solid GaN at temperatures close to the melting point and moderate system pressures, therefore traditional Bridgman or Czochralski techniques are beyond consideration. Vapor phase epitaxy techniques such as halide vapor phase epitaxy (HVPE), metalorganic chemical vapor deposition (MOCVD) and molecular beam epitaxy (MBE), show similar synthesis issues for GaN and ternary III-Nitride alloys, including the difficulty to control final alloy thickness, contamination with carbon from metal-organic precursors, and ultra-high vacuum requirements. Particularly for the ternary alloys, phase segregation is very common.⁶²

Direct nitridation of molten gallium using nitrogen plasma can be used to create GaN. However, the nucleation and growth of Gallium nitride occurs in bulk and results in GaN layer on top of molten gallium. Recently, epitaxial growth of gallium nitride on substrates using nitridation of molten gallium was achieved by intermittently exposing nitrogen plasma. The plasma exposure created a concentration gradient of nitrogen radicals in the melt and pulsing on the order of minutes avoided supersaturation of the molten gallium surface to reach critical levels compared to bulk. Under these conditions, the growth of GaN occurred in epitaxial fashion at the substrate/liquid interface and not in other regions of the melt neither on its surface. The technique resulted in the growth of single-crystal quality GaN films at around 1 $\mu\text{m}/\text{h}$, in a Vapor Liquid Phase Epitaxy (VLPE) fashion.⁶³ In the present work, the same technique proved its effectiveness to grow dilute $\text{GaSb}_x\text{N}_{1-x}$ and $\text{GaBi}_y\text{N}_{1-y}$ films with alloying fraction around 0.01, which has been out of reach in techniques such as MOCVD.

Crystallographic and optical properties of the alloys were evaluated confirming the potential of the synthesis technique to produce good crystal quality materials, and on the

other hand, that the alloys have a band gap reduction discontinuity in the studied alloying range.

5.2. Growth of $\text{GaSb}_x\text{N}_{1-x}$ and $\text{GaBi}_y\text{N}_{1-y}$ Films

The experimental setup consists of a quartz tube of 30mm OD and 80cm length sitting on a furnace. N to Ar gas mixture has been flown in a 1:9 ratio and an radio-frequency plasma of 100 W was applied intermittently with cycles of 1 minute “on” and 10 minutes “off”. A 0.1 mm molten gallium layer covered the substrate (GaN for $\text{GaSb}_{0.012}\text{N}_{0.988}$ and sapphire for $\text{GaSb}_{0.015}\text{N}_{0.985}$ and $\text{GaBi}_{0.014}\text{N}_{0.986}$) and it was heated at 900 °C. Antimony has been supplied in powder form in a boat reaching a temperature of 500 °C and bismuth has been supplied as BiCl_3 at room temperature

The samples were synthesized on GaN or sapphire substrates by dissolving plasma activated nitrogen and substitutional anion species i.e., bismuth trichloride and antimony, into the molten gallium layer dispersed on the substrate and kept at 900 °C. 100 sccm of nitrogen were ionized with a radio frequency source at room temperature and then used to transport substitutional anion species that were kept.

The duration of the growth was five hours. More details related the Plasma Assisted Vapor Liquid Phase Epitaxy method can be found in the work by Jaramillo et al.⁶³ The main difference here is the introduction of anion species in the gas phase along with nitrogen for liquid phase epitaxy of ternary alloys.

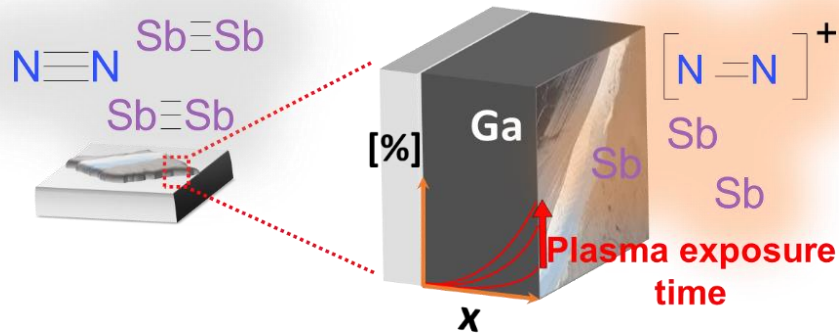


Figure 5.1 Schematic of the $Ga(Sb \text{ or } Bi)_xN_{1-x}$ alloy growth process.

Figure 5.1 shows different stages in the growth of the $Ga(Sb \text{ or } Bi)_xN_{1-x}$ alloys, initially the surface tension of molten gallium causes it to form droplets and then at elevated temperatures and the exposure to plasma, it spreads out covering the substrate of approximately 2 cm². After the dissolution of V-group species into gallium, the alloy formation takes place in a Vapor Liquid Phase Epitaxy fashion. By the end of the growth process, unreacted gallium covers the top of the III-V alloy.

5.3. $GaSb_xN_{1-x}$ and $GaBi_yN_{1-y}$ Film Characterization

Figure 5.2a&b show cross sectional transmission electron micrograph (a) and scanning electron micrograph (b) of 400 nm thick $GaSb_{0.003}N_{0.997}$ alloy on GaN. The grown alloy exhibits a satisfactory crystalline quality which can also be confirmed through high-resolution transmission electron micrographs (see Figure 5.5a). Figure 5.2c&d present a top view of the same sample, where the hexagonal structure becomes evident.

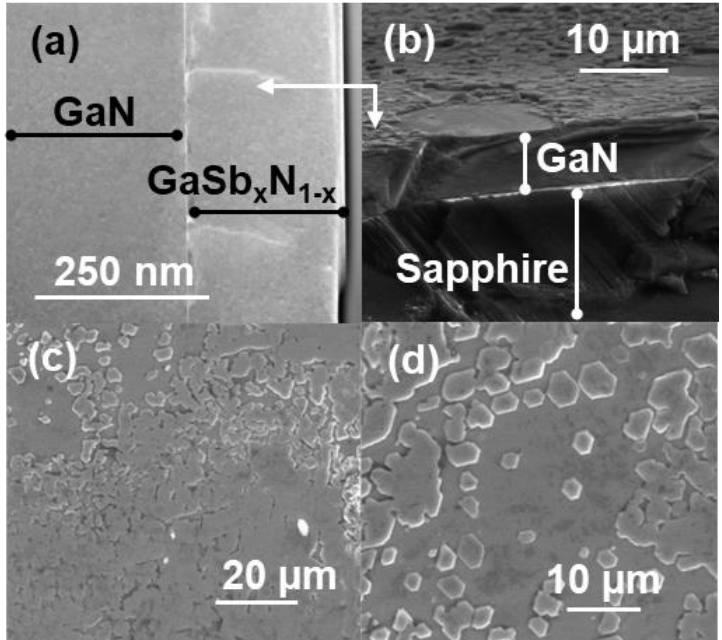


Figure 5.2 Cross sectional transmission electron micrograph (a) and scanning electron micrograph (b); top view scanning electron micrographs of $\text{GaSb}_{0.003}\text{N}_{0.997}$ alloy on GaN (c & d).

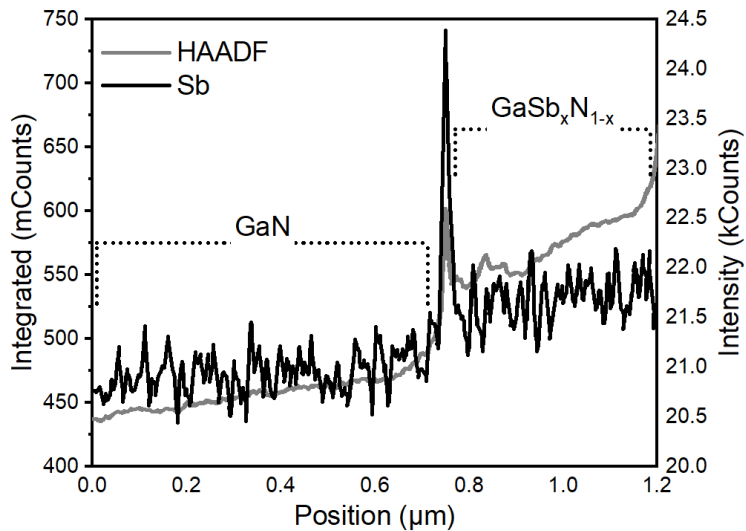


Figure 5.3 Antimony mapping across GaN substrate and $\text{GaSb}_{0.003}\text{N}_{0.997}$ alloy.

Figure 5.3 shows the antimony mapping across the GaN substrate, the interface and the grown $\text{GaSb}_{0.003}\text{N}_{0.997}$ alloy. Even though a level of antimony can be observed in the GaN

side, it was interpreted as the detection baseline of the instrument. The alloy side shows a slightly higher antimony content that is consistent with the incorporation level determined by x-ray diffraction spectra.

Of particular interest is the antimony level spike detected at the interface between GaN and $\text{GaSb}_{0.003}\text{N}_{0.997}$. Antimony segregation indicates the species can diffuse through the gas bulk and the molten gallium layer reaching the gallium-substrate interface, and having less surface tension than gallium, spreads out onto the substrate. There are reports of the use of antimony and bismuth as wetting agents in Liquid Phase Epitaxy growth of III-V alloys. Furthermore, when a metallic layer is formed at the substrate, the rate of diffusion changes differently for each reacting species leading to phase segregation.⁶² This incidental finding could be potentially exploited in the integration of these ternary alloys into functional devices as the metallic layers could provide ohmic or Schottky contacts and/or tunnel junctions.

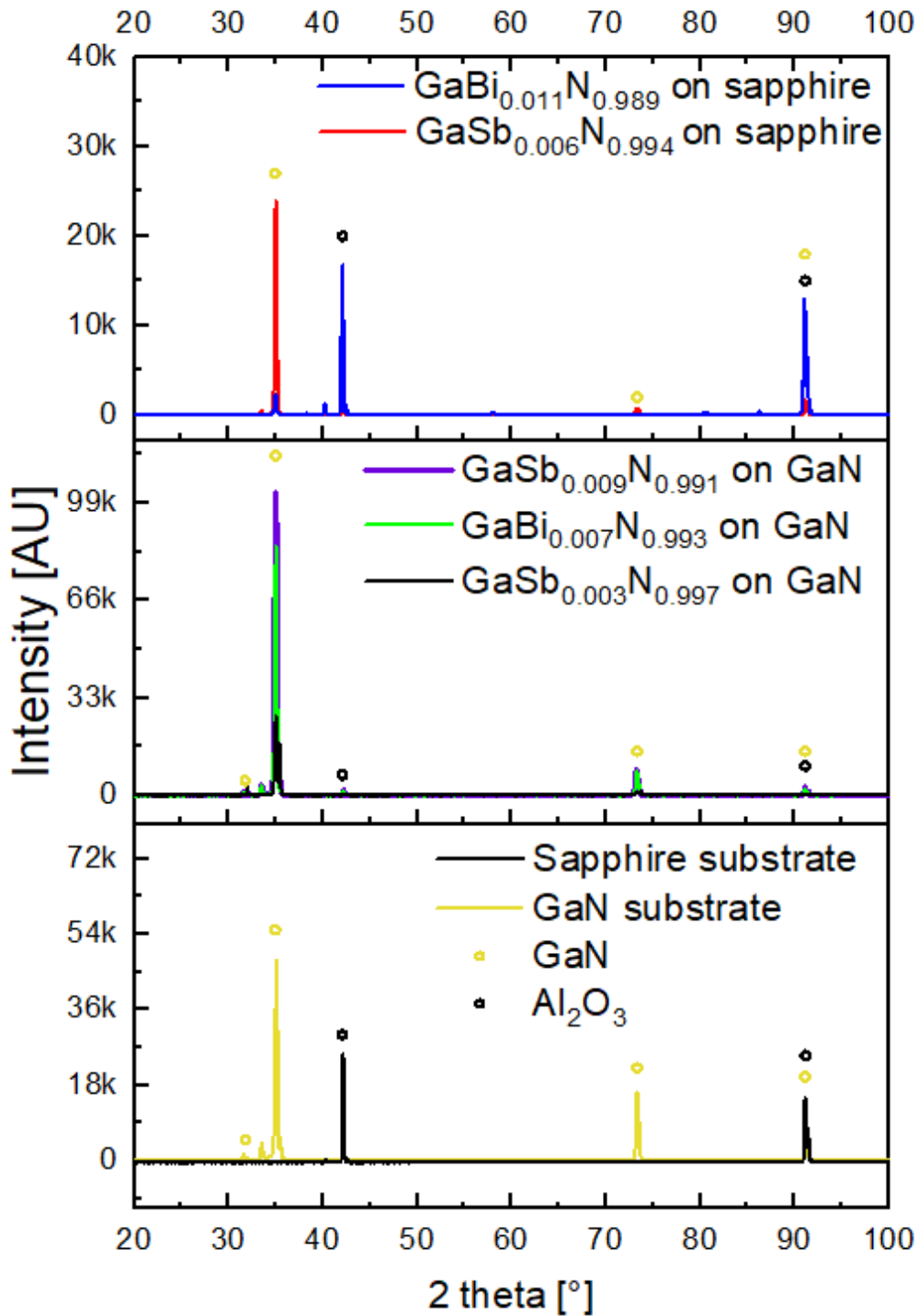


Figure 5.4 Complete XRD spectra of different $\text{GaSb}_x\text{N}_{1-x}$, $\text{GaBi}_y\text{N}_{1-y}$, GaN and sapphire samples.

High resolution Transmission Electron Micrographs of sample $\text{GaSb}_{0.003}\text{N}_{0.997}$ (Figure 5.5a) reveal the epitaxial nature of the grown alloys as the planes on both sides of the $\text{GaN}/\text{GaSb}_x\text{N}_{1-x}$ interface are aligned in the same orientation. This growth characteristic was observed in different regions of the interface however, complete x-ray diffraction spectra of $\text{GaSb}_x\text{N}_{1-x}$ and $\text{GaBi}_y\text{N}_{1-y}$ samples (see Figure 5.4), show the grown alloys have wurtzite structure with (002) and (004) peaks, suggesting that over a larger area the samples exhibit polycrystallinity, particularly where the gallium wetting of the substrate was not optimum. Figure 5.5b compares x-ray diffraction spectra around (002) of different $\text{GaSb}_x\text{N}_{1-x}$ and $\text{GaBi}_y\text{N}_{1-y}$ alloys versus commercial MOCVD-grown GaN and a sapphire substrate. Most of the ternary alloys were grown on GaN substrates except $\text{GaSb}_{0.006}\text{N}_{0.994}$ and $\text{GaBi}_{0.011}\text{N}_{0.989}$ which were grown directly on c-plane oriented sapphire, but regardless of the used substrate all samples exhibit a (002) peak shift towards lower 2θ values, consistent with a lattice parameter increase due to radii size difference between nitrogen and the substitutional anion, i.e., Sb or Bi. The lattice parameter increase and Vegard's Law were used to estimate the reported levels of substitutional anion incorporation. EDAX analysis was also performed to investigate the alloying degree and even though the results are slightly higher than the values determined through x-ray diffraction, they are in the same order of magnitude (see Table 5.1).

Table 5.1. Comparison of sample composition determined through X-ray diffraction and EDAX

| Sample | From XRD | | From Edax |
|---------------------------------------|-------------------------|-----------------------|-----------------------|
| | molar concentration (%) | atomic percentage (%) | atomic percentage (%) |
| $\text{GaSb}_{0.009}\text{N}_{0.991}$ | 0.45 | 0.23 | 0.32 ± 0.05 |
| $\text{GaSb}_{0.003}\text{N}_{0.997}$ | 0.15 | 0.08 | 0.28 ± 0.05 |
| $\text{GaBi}_{0.007}\text{N}_{0.993}$ | 0.33 | 0.16 | 0.24 ± 0.13 |
| $\text{GaSb}_{0.006}\text{N}_{0.994}$ | 0.30 | 0.15 | 0.24 ± 0.07 |
| $\text{GaBi}_{0.011}\text{N}_{0.989}$ | 0.53 | 0.26 | 0.23 ± 0.1 |

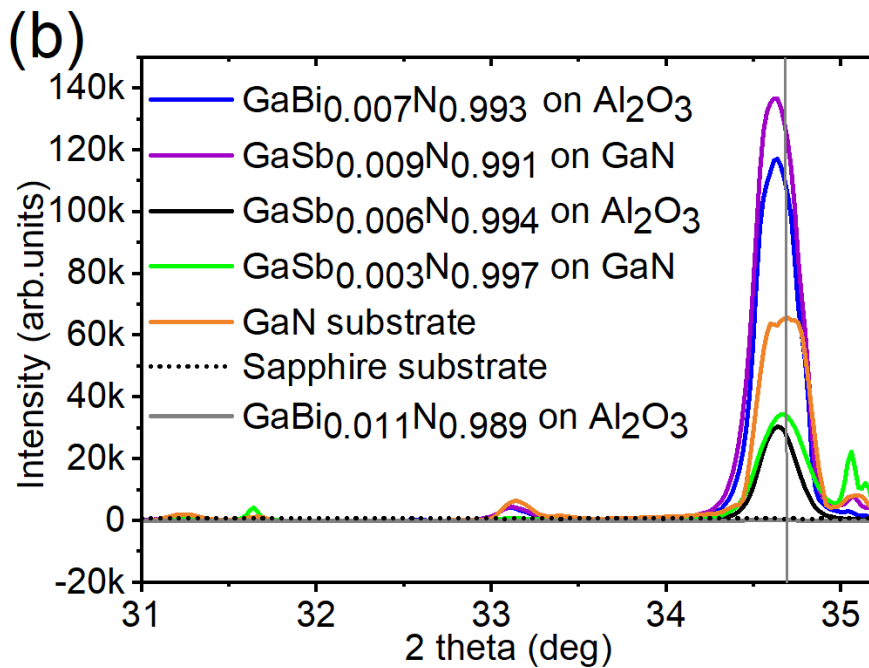
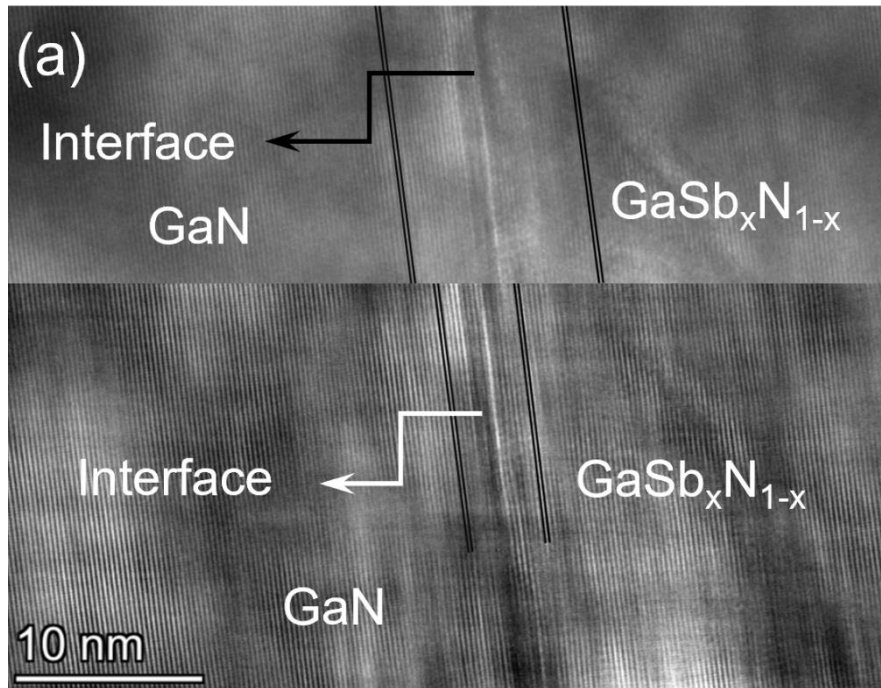


Figure 5.5 a. High resolution Transmission Electron Micrographs of sample $\text{GaSb}_{0.003}\text{N}_{0.997}$ b. X-ray diffraction spectra of GaN, sapphire, $\text{GaSb}_x\text{N}_{1-x}$ and $\text{GaBi}_y\text{N}_{1-y}$ alloys

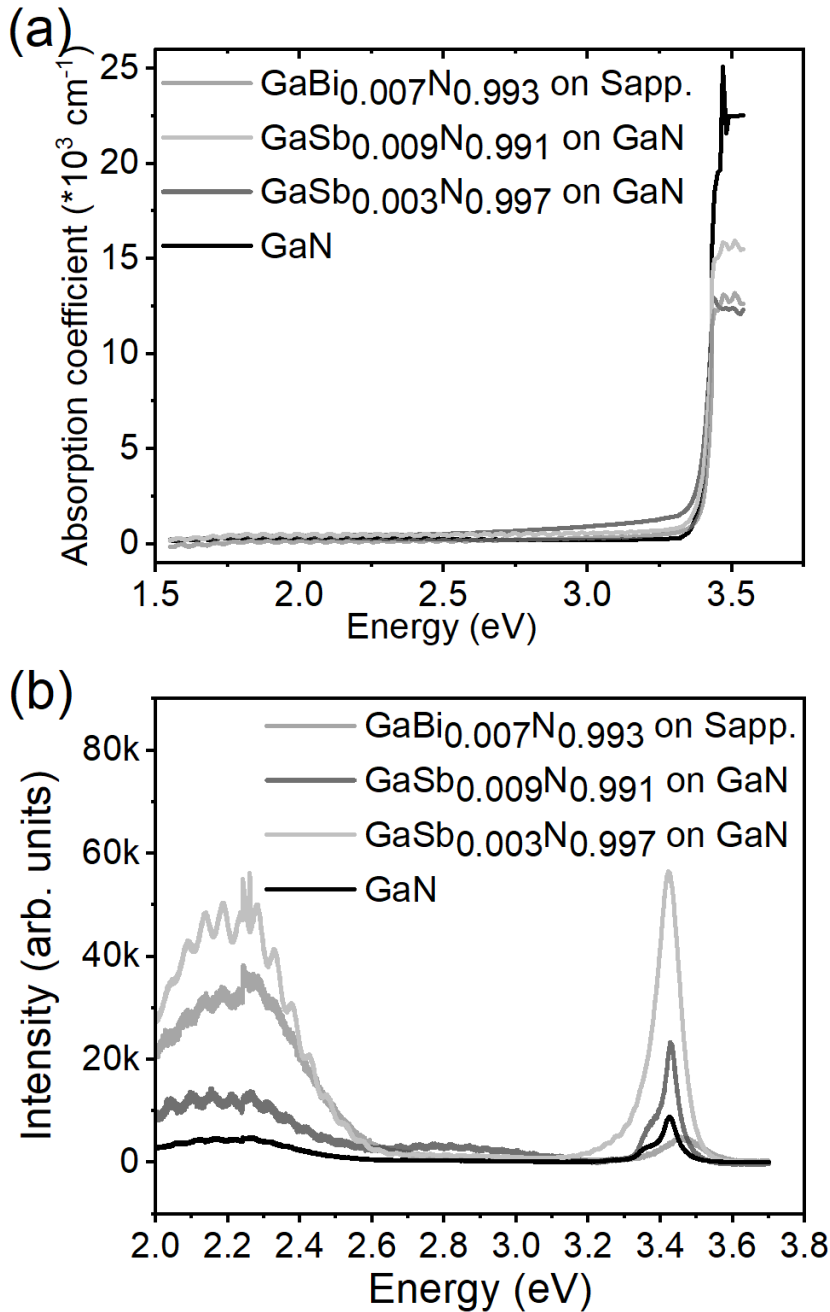


Figure 5.6 Absorption coefficient (left), and photoluminescence spectra (right) of GaN, GaSb_xN_{1-x} and GaBi_yN_{1-y} alloys.

Figure 5.6a&b present the absorption coefficient and photoluminescence spectra of samples GaSb_{0.006}N_{0.994}, GaSb_{0.003}N_{0.997}, GaSb_{0.009}N_{0.991}, GaBi_{0.007}N_{0.993} and GaN. The absorption coefficient curves show the photon energy required for band-to-band

absorption is around 3.4 eV, same as pure GaN direct band gap. The negligible light absorption at energy values below the direct band gap can be attributed to intra-band energy states. The room temperature photoluminescence spectra, Figure 5.6b, shows two distinctive peaks around 2.2 eV and 3.4 eV which correspond to yellow luminescence and band gap energy respectively. The discussed findings suggest dilute anion substitution alloying is not sufficient to produce changes in the density of states of host material, GaN.

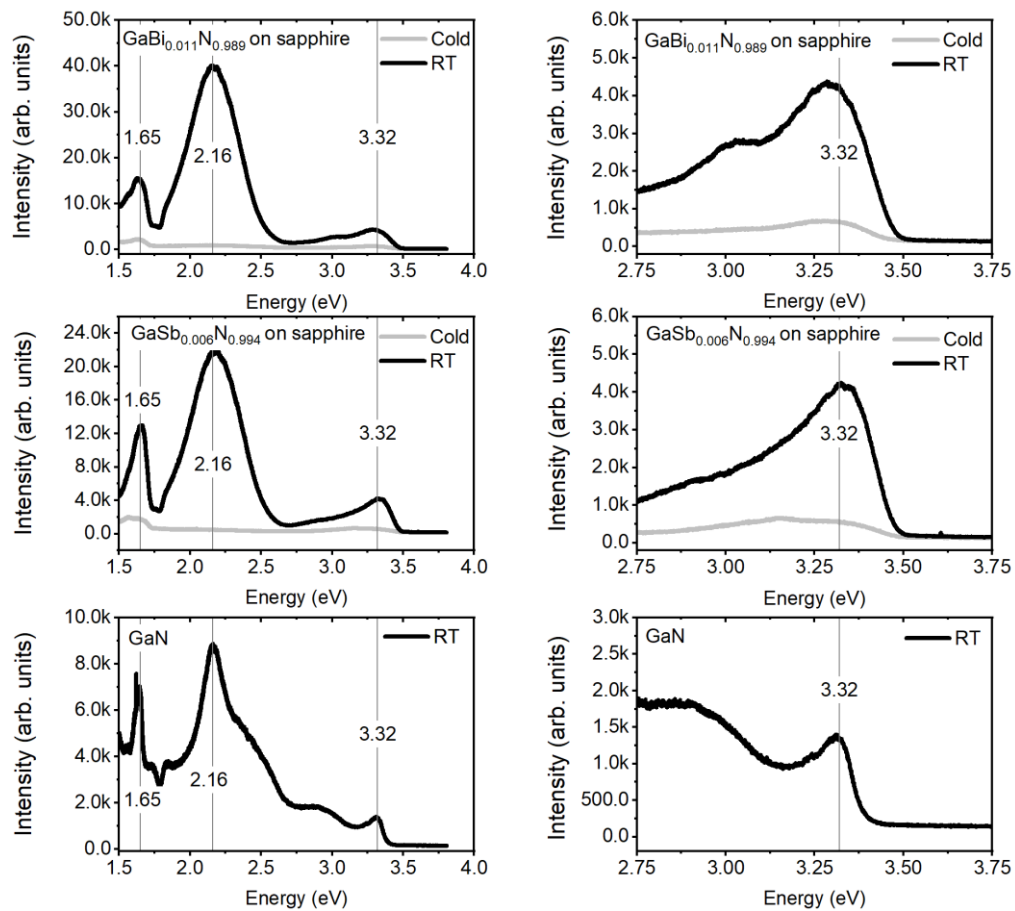


Figure 5.7 Photoluminescence measurements at room temperature and $-196\text{ }^{\circ}\text{C}$ of GaN, $\text{GaSb}_x\text{N}_{1-x}$, $\text{GaBi}_y\text{N}_{1-y}$ on sapphire.

For a better understanding of the energy transitions in pure GaN and the grown ternary alloys, wider range photoluminescence measurements were performed at room

temperature and $-196\text{ }^{\circ}\text{C}$ (see Figure 5.7). GaN, GaSb_{0.006}N_{0.994} and GaBi_{0.011}N_{0.989} grown on sapphire, all exhibit the band gap energy transition at 3.4 eV and yellow luminescence around 2.2 eV, as well as a peak around 1.65 eV. A band gap peak closeup presented in the right panel of Figure 5.7 shows a shoulder towards lower energy values, around 3 eV in the case of sample GaBi_{0.011}N_{0.989}, which is worth further investigation.

Chowdhury et al.²⁹ synthesized GaSb_xN_{1-x} alloys through Molecular Beam Epitaxy with antimony content between 0 and 0.8% (determined through Secondary Ion Mass Spectrometry) and claimed the achievement of a continuous band gap reduction within this dilute incorporation range. The photoluminescence measurements of 0-D and nanowire samples reported as band-to-band energy transitions were 2.03 eV, 2.27 eV, 2.34 eV and 2.90 eV. By comparing these values to the ones presented in Figure 5.7 we can observe relative correspondence, for instance, peaks 1.65 eV and 2.2 eV in our measurements and 2.03 and 2.27 eV in theirs, could probably be ascribed to the same originating intra-band defect and not to band gap energy transitions.

5.4. Summary

GaSbN with 1.2 and 1.5 at% antimony incorporation and GaBiN with 1.4 at% bismuth incorporation have been synthesized with Plasma-Assisted Vapor Liquid Phase Epitaxy. This technique has allowed the synthesis of high crystalline quality alloys with dilute anion incorporation levels that have been out of reach in previous studies of the same material system, carried out with Metal-Organic Chemical Vapor Deposition.

6. CHAPTER SIX

GaSb_xN_{1-x} AND GaBi_yN_{1-y} NANOWIRE GROWTH THROUGH METAL CATALYZED PLASMA-ASSISTED VAPOR LIQUID PHASE EPITAXY

6.1. Introduction

Research on anion diluted nitrides is scarce since their synthesis through MOCVD and MBE has always been a challenge because of the low decomposition and evaporation temperatures of GaN and group-III elements, respectively,²⁵ which contrast with the high temperatures required for ammonia cracking. Additionally, this precursor accounts for 30-50 % of MOCVD costs³⁶ due to its low incorporation efficiency (3.8% at 700 C).²⁵ To circumvent these challenges many works on binary GaN, and AlN systems introduced the use of nitrogen plasma, enabling the growth at lower temperatures compared to ammonia sourced MBE and MOCVD.²⁶ Plasma-assisted techniques have also made possible the growth of In-containing nitrides, otherwise limited by InN low sublimation temperature at moderate pressures²⁷.

Lower growth temperatures in plasma-assisted vapor-solid growth techniques have also served to overcome challenges in the synthesis of IIIV_{1-x}N_x nitrides that suffer from low anion substitution, due to the high vapor pressures of group-V elements. Through Plasma Assisted Molecular Beam Epitaxy (PA-MBE), 1.2 eV band gap GaBi_{0.11}N_{0.89} was achieved.¹⁶ Other studies of alloys with visible light absorption behavior such as PA-MBE-grown GaSbN, report a drastic band gap shift from 3.4 to 2 eV with antimony content below 5 mol%,²⁸ and 1 mol%.²⁹ In contrast, in our own experimental work on Plasma Assisted Vapor Liquid Phase Epitaxy (PA-VLPE) synthesis of GaSbN and GaBiN films

(CHAPTER FIVE), we did not observe a band gap reduction (versus pure GaN) for alloys with antimony or bismuth content less than 1 at%, and DFT simulations suggest GaN band gap reduction can only be achieved when antimony content is between 2 - 3 at%.³⁰ Other studies of our group with ammonia sourced² and Plasma-Assisted¹ MOCVD, have enabled the growth of GaSbN films (2 - 8 Sb at%) and nanowires (2 - 4 Sb at%) with band gaps around to 2 eV. PA-MBE-grown GaSbN nanowires with antimony content between 3 to 10 mol%, exhibited sub-bandgap light absorption³¹, results that coincide more closely with ours.

Due to the visible light absorption behavior of these anion diluted nitrides, most of the previous studies also focused on their performance as photoanodes for water splitting applications. In this chapter the growth and characterization of Au and Cu catalyzed PA-VLPE synthesis of $\text{GaSb}_x\text{N}_{1-x}$ and $\text{GaBi}_y\text{N}_{1-y}$ nanowires where x and y lie between 3.4 - 5.6 at% and 1.0 – 8.8 at%, respectively, are presented.

6.2. Metal Catalyzed $\text{GaSb}_x\text{N}_{1-x}$ and $\text{GaBi}_z\text{N}_{1-z}$ Nanowire Growth

The experimental setup for the alloy's growth is illustrated in Figure 3.2. Sapphire, (100)-Si and stainless-steel substrates were coated with 20 nm thick catalyst layer (gold or copper) are loaded into the quartz tube that is heated with a one-zone furnace. Preceding the substrates gallium and group-V metals (antimony or bismuth) are loaded in quartz boats. The electrodes used to apply radio frequency power are located right outside of the furnace.

After the substrates and precursors are loaded in the appropriate positions inside the tube, the system is closed, purged with hydrogen and leak checked. To remove any oxide from the substrates and metallic precursors, 50 sccm of hydrogen are fed to the system and 70 W are applied to the flowing gas while the system is heated from room

temperature to 750 C, which takes about 15 min. While keeping the furnace temperature at 750 C, 10 sccm of hydrogen chloride diluted in 50 sccm of hydrogen, are fed for one hour, with the purpose of transporting gallium and group-V halide species that result from the reaction between hydrogen chloride and the metals. Since the substrates have a 20 nm catalyst coating, the flux of GaCl and SbCl/BiCl reached the surface and the species dissolved into the catalyst. After the “transport” step has been completed, the furnace temperature is raised to the growth temperature (between 800-950 C) and a mixture of 40 sccm of nitrogen, 15 sccm of argon and 10 sccm of HCl are fed into the system. As has been explained elsewhere ²¹, nitrogen gas does not react with gallium to form GaN at the pressure and temperature conditions used in this study, and therefore 70 W radio frequency power was applied intermittently (0.5 min on and 5 min off) to the gas mixture for one hour, generating ionized and other activated nitrogen species that dissolved into the catalyst and formed the alloys by reacting with gallium and antimony/bismuth.

It is worth noting that high (Ga+Sb/Bi)/N ratio was likely the prevalent condition in all experiments, given that gallium and antimony/bismuth fluxes are exponentially proportional to temperature, as the metals react with hydrogen chloride during “transport” and “growth” steps at 750 °C and 800 °C- 950 °C, respectively, while nitridation occurs only during the “growth” step.

6.3. GaSb_xN_{1-x} and GaBi_yN_{1-y} Nanowire Characterization

Scanning Electron micrographs of GaSb_xN_{1-x} and GaBi_yN_{1-y} nanowires grown at different temperatures are shown in Figure 6.1. The growth temperature affects both the alloying degree and the shape of the wires, i.e., at 800 °C GaSb_xN_{1-x} wires are very thin and the antimony incorporation is only 3.4%, however, the wire diameters become larger at 900 and 950 °C and the antimony content in these alloys is 4.9 and 5.6 %, respectively.

A similar trend can be observed in $\text{GaBi}_y\text{N}_{1-y}$ samples, where thin wires with low bismuth content are obtained at 800 °C, and the wire diameter increases as well as the bismuth content when the growth temperature was increased to 950 °C. The diffusion coefficient of all alloy constituents into the catalyst increases with temperature and so does the $(\text{Ga}+\text{Sb}/\text{Bi})/\text{N}$ ratio (as explained in section 6.2) which promotes the observed morphology changes, as it has been previously described for GaN wire growth through halide VLS mechanism, that an increase in the GaCl flux while keeping ammonia flux constant, would favor lateral growth over axial growth resulting in shorter and thicker wires.³¹

Figure 6.1a shows $\text{GaSb}_{0.041}\text{N}_{0.959}$ sample grown at 850 °C, the wire growth direction was identified as a-plane because it is parallel to $10\bar{1}0$ direction. The corresponding hexagonal diffraction pattern is shown in Figure 6.2b and high-resolution Transmission Electron Micrographs perpendicular to wire's c-plane orientation are shown in Figure 6.2c&d. The interplanar distance, for $\bar{1}100$, $01\bar{1}0$ and $10\bar{1}0$ was determined to be 2.69, 2.83 and 2.69 Å, respectively, averaging 2.74 Å which is close to pure a-GaN interplanar distance of 2.76 Å. Considering the wires are mostly exposing c-plane when still attached to the substrate (see Figure 6.1), it is consistent to observe (002) peak in the x-ray diffraction measurements (Figure 6.3a). The degree of alloying (x or y) increases as a function of temperature from 3.4 to 5.6 at% in the case of $\text{GaSb}_x\text{N}_{1-x}$ wires, and from 1 to 8.8 at% in the case of $\text{GaBi}_y\text{N}_{1-y}$ alloys grown at temperatures between 800 and 950 °C, respectively. Higher growth temperatures result in larger (002) peak shifts towards lower 2θ values with respect to pure GaN. As described previously, $(\text{Ga}+\text{Sb})/\text{N}$ ratio increases as a function of temperature and therefore the availability and incorporation of substitutional species increases as well.

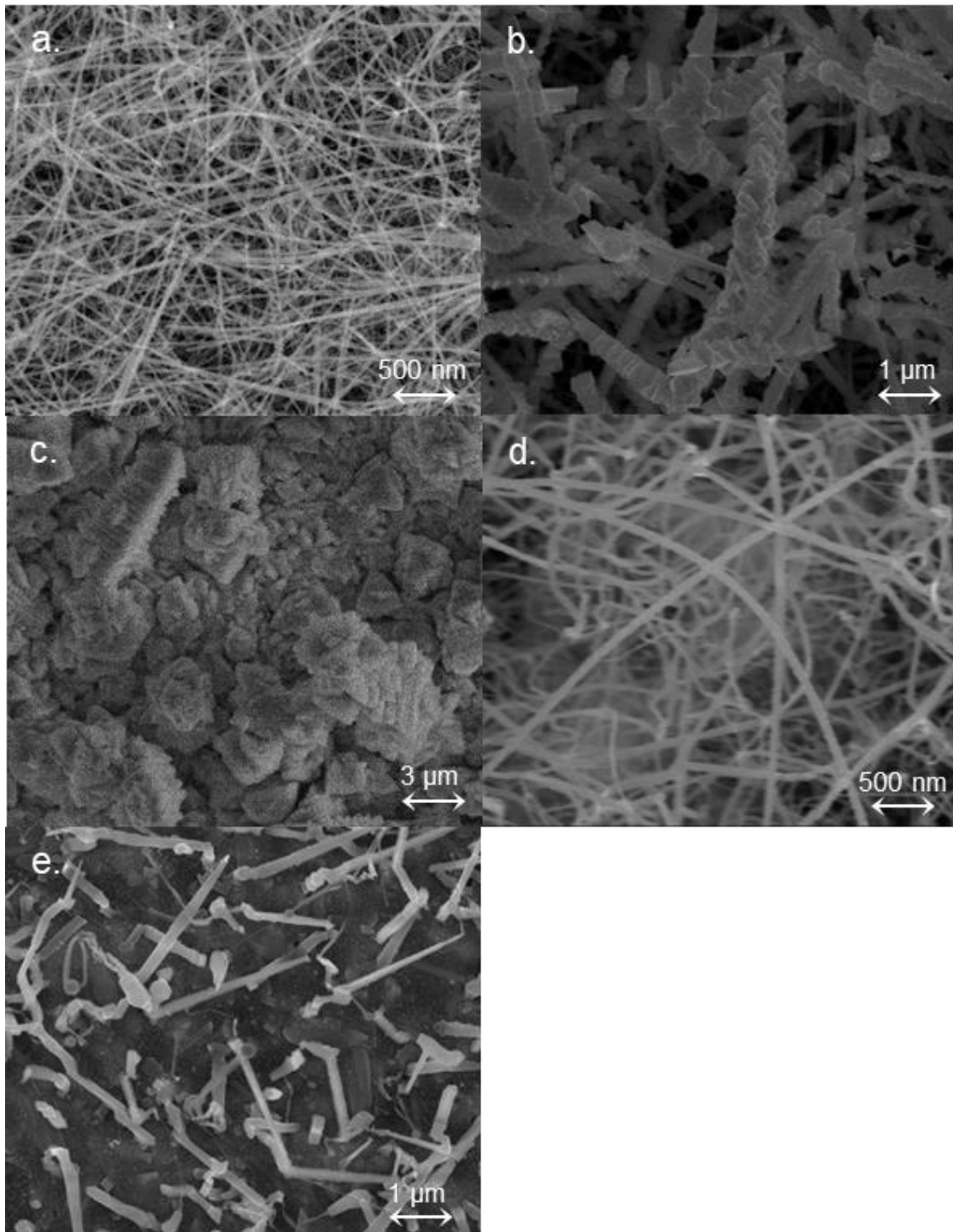


Figure 6.1 $\text{GaSb}_x\text{N}_{1-x}$ wires grown at a. 800 °C, b. 850 °C and c. 950 °C. $\text{GaBi}_y\text{N}_{1-y}$ wires grown at d. 900 °C and e. 950 °C

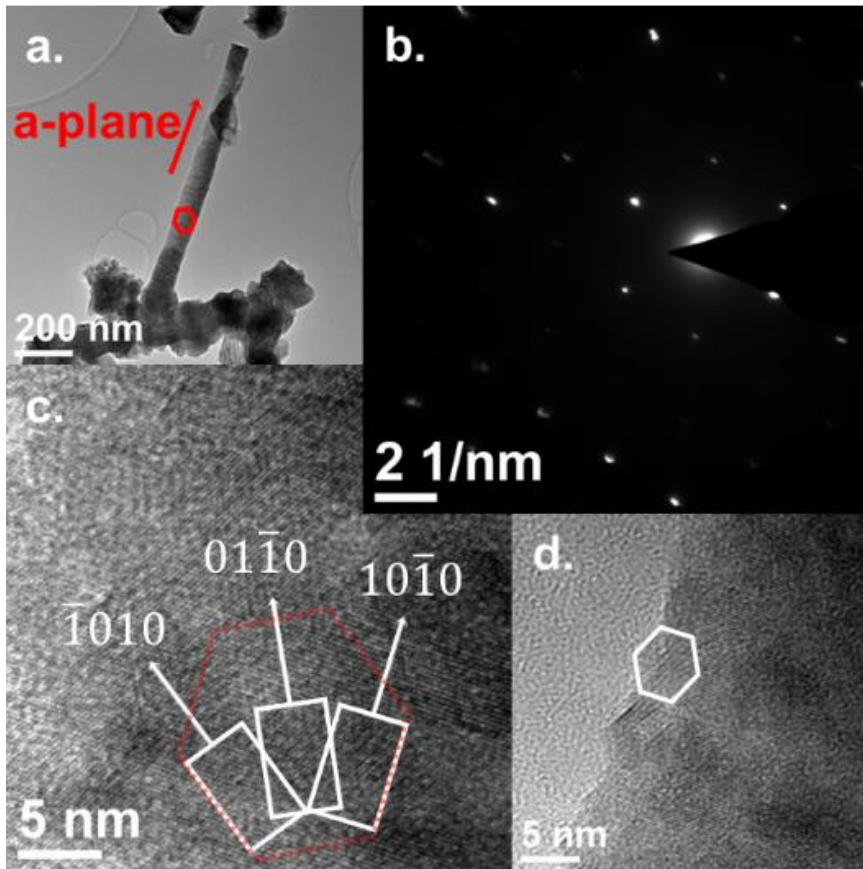


Figure 6.2 a. $\text{GaSb}_{0.041}\text{No}_{0.959}$ wire grown at $850\text{ }^\circ\text{C}$ showing a-plane orientation, b. its corresponding diffraction pattern, c. and d. high-resolution Transmission Electron Micrographs of wire's c-plane orientation.

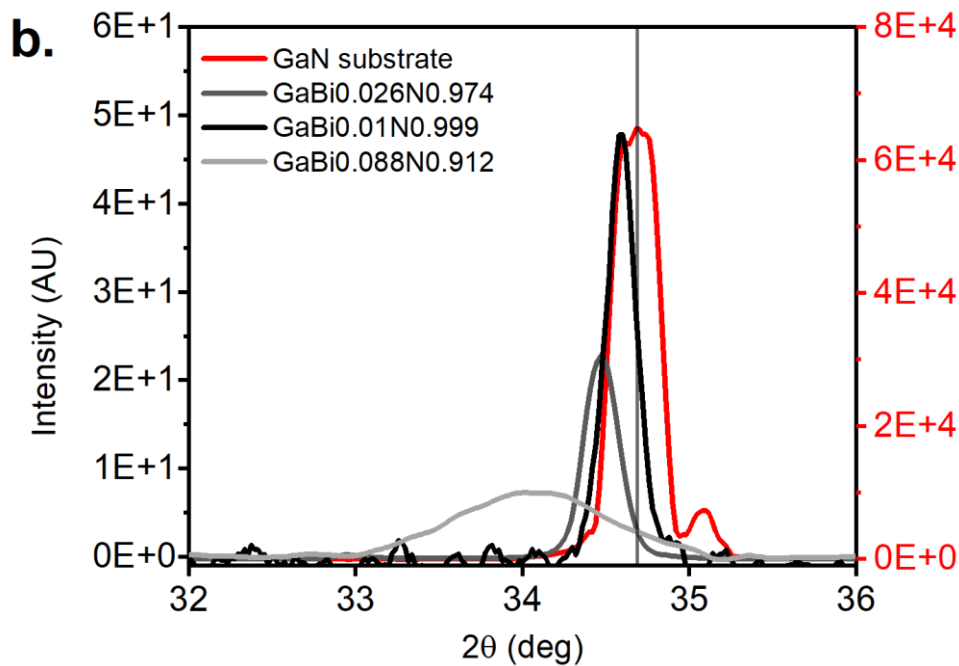
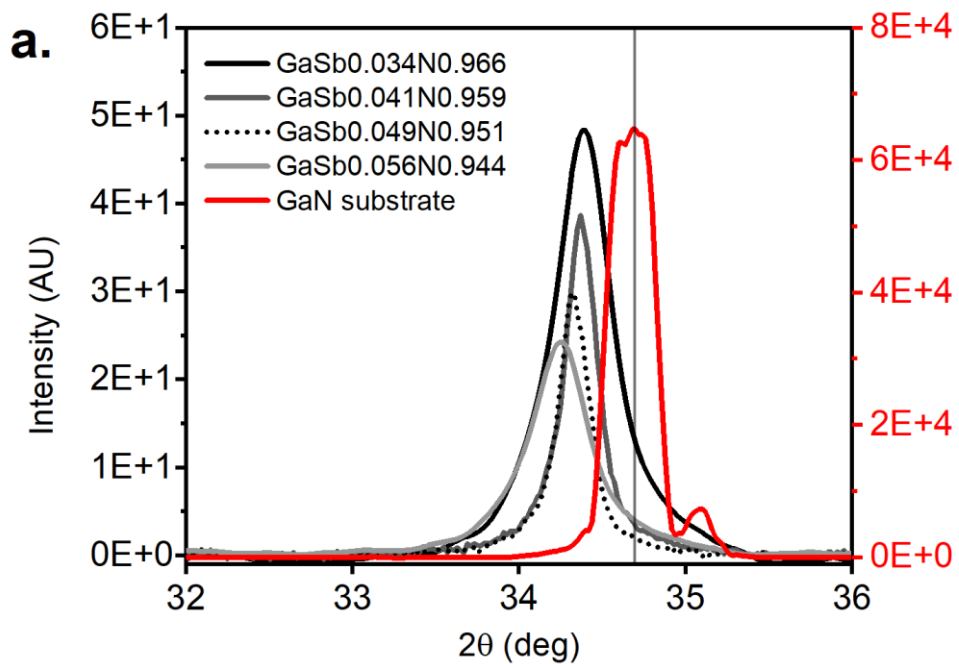


Figure 6.3 X-ray diffraction measurements of a. $\text{GaSb}_x\text{N}_{1-x}$ and b. $\text{GaBi}_y\text{N}_{1-y}$ samples with different degrees of alloying.

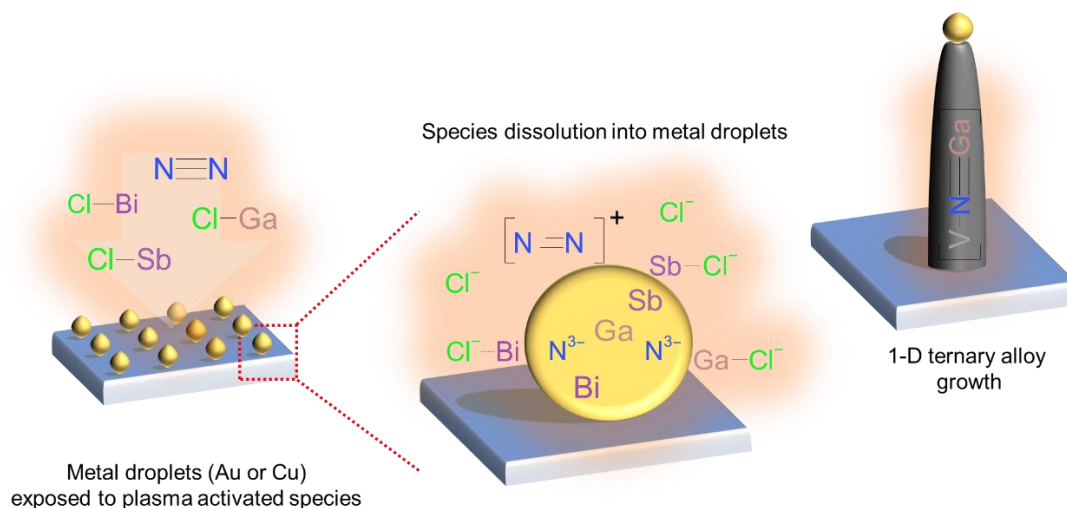


Figure 6. 4 Plasma-Assisted Vapor Liquid Solid growth mechanism

Figure 6. 4 depicts the proposed growth mechanism. The dissolution of atomic nitrogen species has been shown before. N_2^+ species may exist in plasma along N species which ultimately dissolve into molten Ga. In this case gallium, nitrogen and substitutional anions saturate the catalyst droplet and the alloy starts to grow epitaxially forming a 1-D structure.

Figure 6.5 corresponds to $GaSb_xN_{1-x}$ wires grown at 850 °C. *Figure 6.5a* shows a high-resolution Transmission Electron Micrograph where a round darker element stands out, and the contrast difference suggests it probably contains a high conductivity element. Being located at the tip of the wire is indicative of a Vapor Liquid Solid mechanism of alloy growth, by dissolution into copper droplets.

In *Figure 6.5c*, it can be observed that copper mainly concentrates in round areas, and even though, the alloyed nature of the samples has been discussed previously, antimony seems to have higher concentration in the same spots as copper (see *Figure 6.5e*).

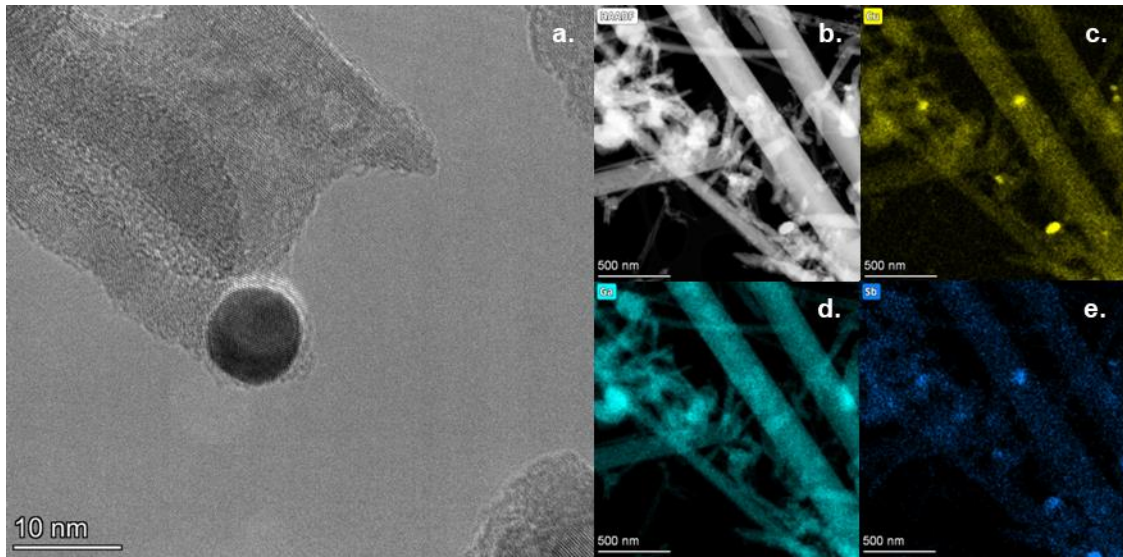


Figure 6.5 High resolution Transmission Electron Micrograph of a. $\text{GaSb}_x\text{N}_{1-x}$ wires grown at 850 °C, b. the corresponding High-angle annular dark-field image, and the elemental mapping of c. copper, d. gallium and e. antimony.

Figure 6.6a&b show tauc plots of $\text{GaSb}_x\text{N}_{1-x}$ and $\text{GaBi}_y\text{N}_{1-y}$ samples with different degrees of alloying. These plots were derived from diffuse reflectance measurements carried out in a PerkinElmer Lambda950 spectrometer equipped with a 60 mm integrating sphere. $\text{GaBi}_y\text{N}_{1-y}$ samples with 1.0 and 2.6 at% of bismuth show a direct absorption band edge close to 3.4 eV that corresponds to pure GaN. The bismuth content 8.8 at% alloy has a very sharp absorption edge below 2 eV. $\text{GaSb}_x\text{N}_{1-x}$ samples containing 3.4 and 4.1 at% of antimony show sub-band gap absorption around 2 eV while samples with 4.9 and 5.6 degree of alloying have a sharper absorption edge below 2 eV.

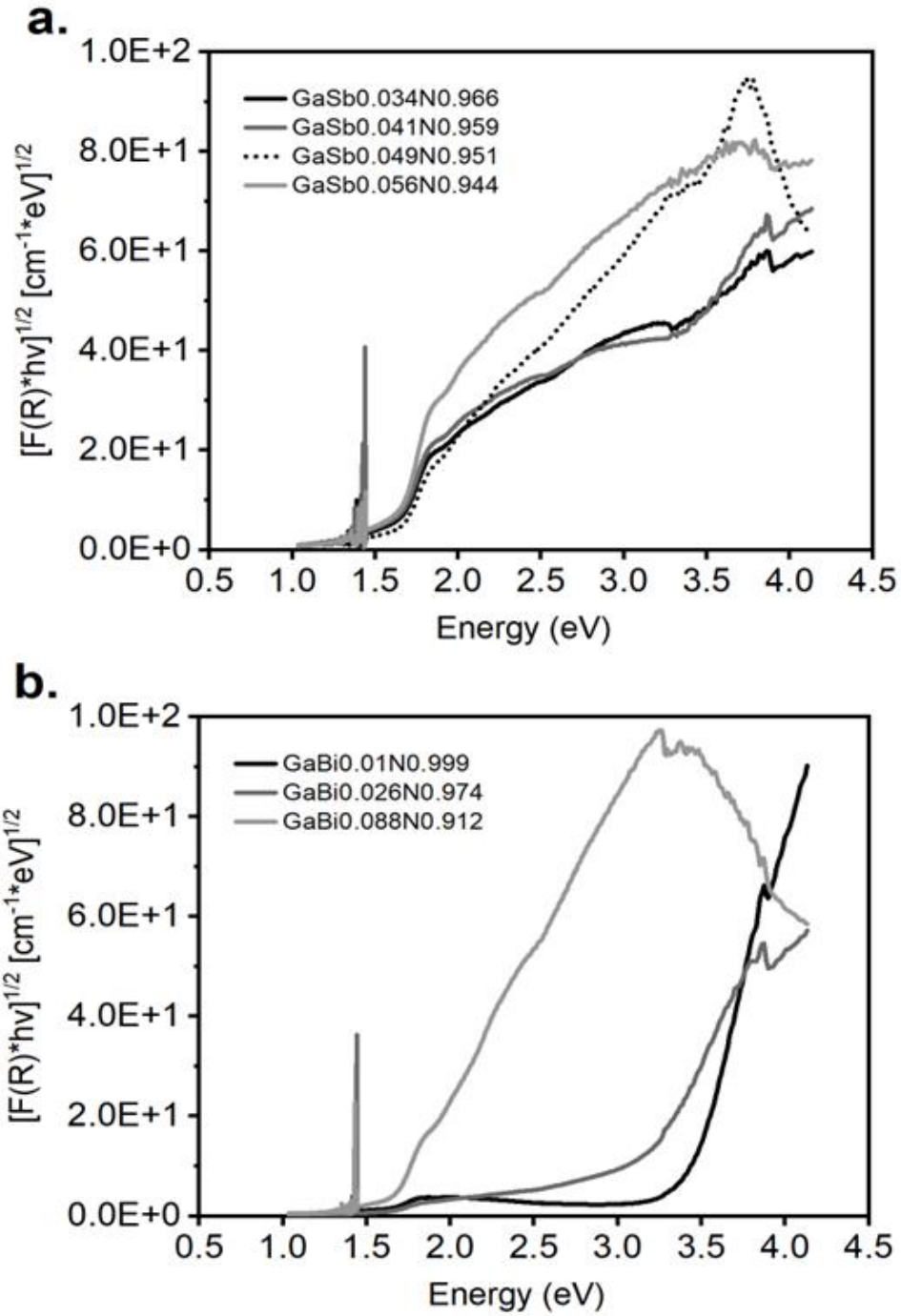


Figure 6.6 Tauc plots of a. $\text{GaSb}_x\text{N}_{1-x}$ and b. $\text{GaBi}_y\text{N}_{1-y}$ samples with different degrees of alloying.

Photocurrent spectroscopy measurements were carried out with $\text{GaSb}_x\text{N}_{1-x}$ samples containing 4.1 and 5.6 at% of antimony, and GaN sample. These measurements

were carried out using a Newport solar simulator with 10 sun irradiance ($1000 \text{ mW}\cdot\text{cm}^{-2}$), in conjunction with a monochromator that was manually set at each individual wavelength from 320 nm to the photoactivity limit of each sample, with increments of 5 or 10 nm. The photocurrent was measured under 0.5 V vs RHE. The results are presented in Figure 6.7. $\text{GaSb}_{0.056}\text{N}_{0.944}$ and $\text{GaSb}_{0.041}\text{N}_{0.959}$ samples exhibit photocurrent up to 620 and 585 nm, 2.00 and 2.12 eV, respectively, while pure GaN is not photoactive beyond 370 nm (3.35 eV). We encountered a difficulty to keep constant irradiance as a function of wavelength after the light beam is filtered in the monochromator. The irradiance decreases by two orders of magnitude (also after beam is filtered) was in the range between 20–80 $\text{mW}\cdot\text{cm}^{-2}$ and explains the low photocurrent density magnitudes shown in Figure 6.7.

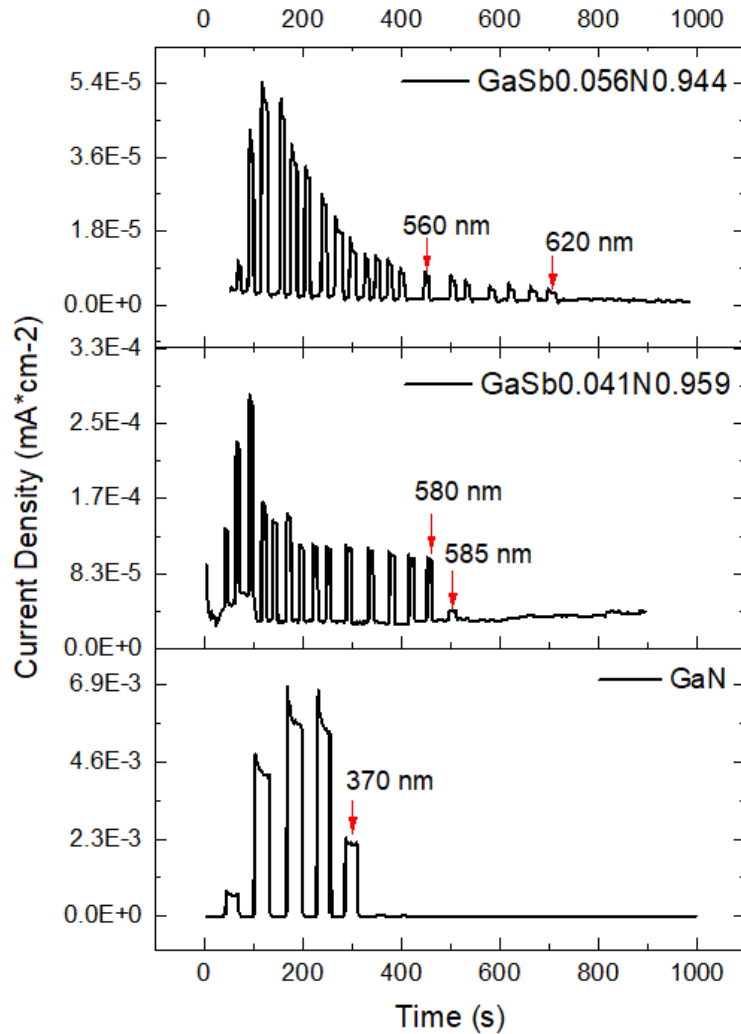


Figure 6.7 Photocurrent spectroscopy measurements of $\text{GaSb}_{0.056}\text{N}_{0.944}$ and $\text{GaSb}_{0.041}\text{N}_{0.959}$ samples

Photocurrent spectroscopy measurements tend to overestimate the optical band gap of materials because a portion of the photo-generated carriers recombines before they can be measured as current. Nonetheless, the photocurrent spectroscopy measurements of three alloys shown in Figure 6.7 are in good agreement with the optical band gap values deduced from Tauc plots.

Linear Sweep Voltammeteries of $\text{Ir}_x\text{WO}_{3-x}$ decorated samples $\text{GaSb}_{0.041}\text{N}_{0.959}$, $\text{GaSb}_{0.049}\text{N}_{0.951}$ and $\text{GaSb}_{0.056}\text{N}_{0.944}$, under 1, 5 and 10 sun irradiance are shown in Figure

6.8. The measurements were conducted in a three-electrode configuration using Ag/AgCl and platinum mesh as reference and counter electrode, respectively. The photocurrent onset is visible at applied biases that differ among the samples within tens of mV around 0 V vs RHE. Surprisingly, same photocurrent density onset potential was observed for the uncatalyzed samples (see inset in Figure 6.8), however the magnitude of the photocurrent density is ~20% lower when no catalyst is used. This suggests $\text{Ir}_x\text{WO}_{3-x}$ might be acting as a co-absorber rather than a catalyst. More details about the synthesis of $\text{Ir}_x\text{WO}_{3-x}$ can be found in the work by Kumari et. al.⁶⁴. $\text{Ir}_x\text{WO}_{3-x}$ loading in this study was approximately $0.028 \text{ mg} \cdot \text{cm}^{-2}$.

As expected, the increase of irradiance has a positive effect on the magnitude of the photocurrent density, i.e. J_{ph} at 5 sun is approximately $5 \times (J_{\text{ph}}$ at 1 sun), however the photocurrent density at 10 sun falls short from the expected proportional increase. This indicates the photoactivity of the alloys might be absorption limited.

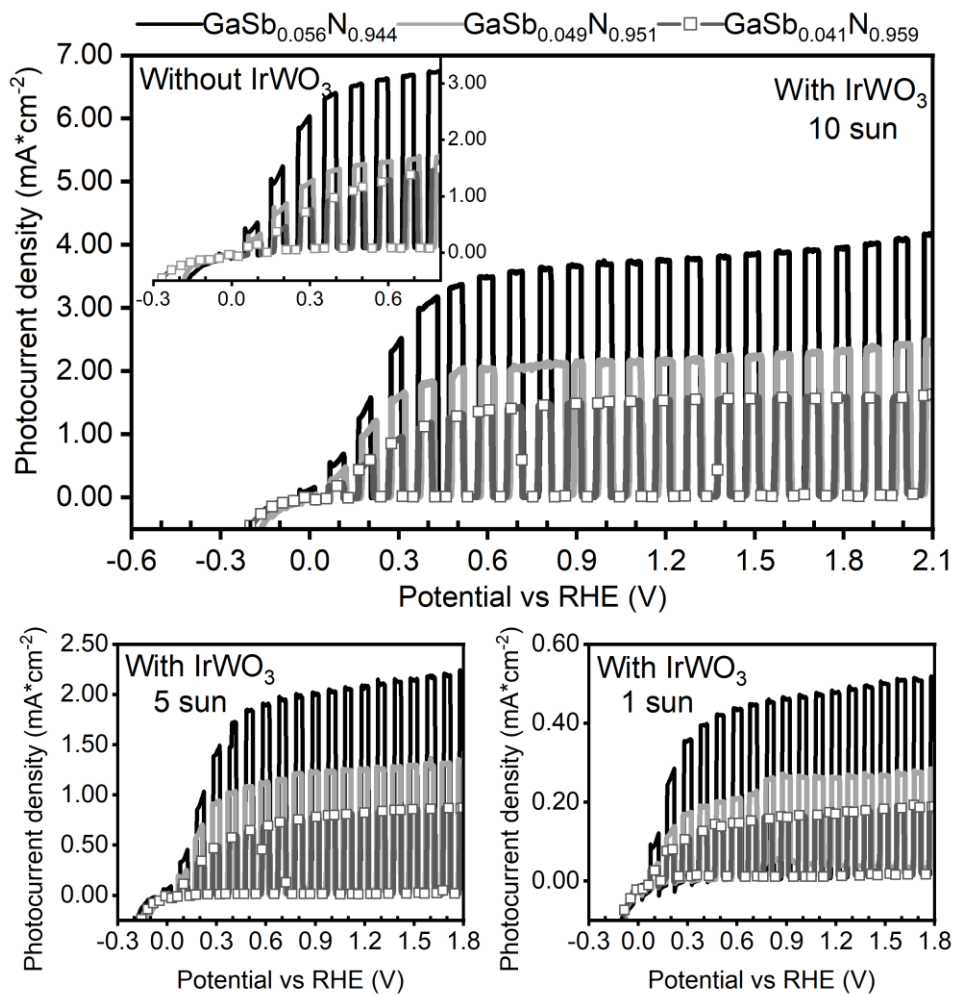


Figure 6.8 Photocurrent density versus applied bias in 3-electrode configuration of Ir_xWO_{3-x} decorated samples $GaSb_{0.041}N_{0.959}$, $GaSb_{0.049}N_{0.951}$ and $GaSb_{0.056}N_{0.944}$, under 1, 5 and 10 sun irradiance. Performance of same three samples under 10 sun without Ir_xWO_{3-x} (inset).

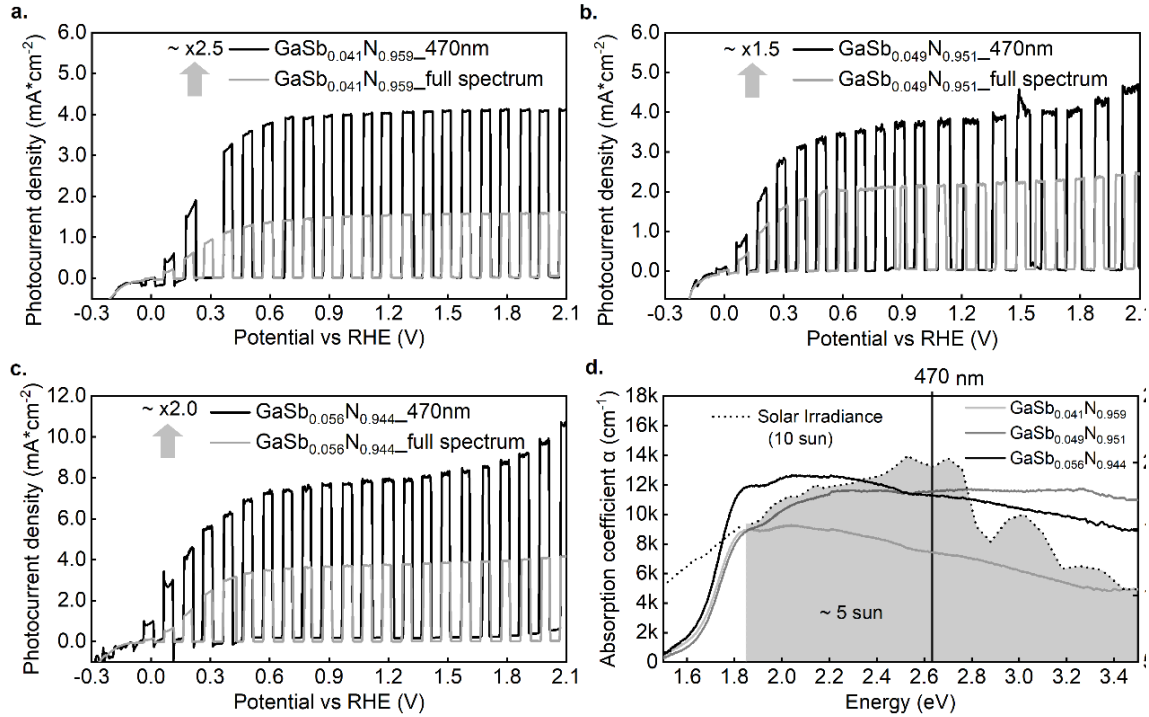


Figure 6.9 Photocurrent density versus applied bias in 3-electrode configuration, under 10 sun irradiance of full spectrum (grey lines) or 470 nm (black lines). a. $\text{GaSb}_{0.041}\text{N}_{0.959}$, b. $\text{GaSb}_{0.049}\text{N}_{0.951}$ and c. $\text{GaSb}_{0.056}\text{N}_{0.944}$. d. Optical absorption coefficient versus photon energy of same three samples (solid lines) and x10(AM 1.5 G) irradiance versus photon energy (dotted line)

Photocurrent density magnitude is also impacted by antimony incorporation differences among the three samples shown in Figure 6.8. Optical absorption coefficients versus photon energy (see Figure 6.9d) show low absorption of photons with energies below 1.8 eV, which means only about half of the energy input supplied with full spectrum illumination can be absorbed by these alloys. $\text{GaSb}_{0.041}\text{N}_{0.959}$ sample exhibits the lowest absorption coefficient, but it increases towards the visible range, while $\text{GaSb}_{0.049}\text{N}_{0.951}$ and $\text{GaSb}_{0.056}\text{N}_{0.944}$ samples have similar absorption capability with weaker wavelength dependence.

Figure 6.9a-c compares the photocurrent density versus applied bias of each sample under 10 sun illumination of full spectrum or 10 sun of 470 nm LED. Considering photocurrent spectroscopy, Tauc plots and absorption coefficient results, it is reasonable to assume that photocurrent density under 470 nm illumination should be twice as high compared to when a full spectrum source is used. That is the case for sample $\text{GaSb}_{0.056}\text{N}_{0.944}$. $\text{GaSb}_{0.049}\text{N}_{0.951}$ sample only shows 1.5 times increase, but sample $\text{GaSb}_{0.041}\text{N}_{0.959}$ which has the lowest absorption coefficient, shows an increase of photocurrent density of 2.5 times. $\text{GaSb}_{0.041}\text{N}_{0.959}$ samples is also the one with thinnest and less vertically aligned wires, which can explain why 470 nm photons can be efficiently absorbed while photons with a broad wavelength distribution cannot.

Figure 6.10 shows the photocurrent density of sample $\text{GaSb}_{0.056}\text{N}_{0.944}$ shorted with a p-Si electrode under 0.5 V versus RHE and 10 sun/470nm illumination. The photocurrent magnitude was high enough to produce visible hydrogen and oxygen bubble formation at the surface of the electrodes. The photocurrent maintained the same order of magnitude over a period longer than 30 hours. There is a moment when electrodes were shaken to remove the accumulated bubbles and the photocurrent recovered a magnitude close to the initial value. This demonstrates the stability of the alloy at typical application conditions.

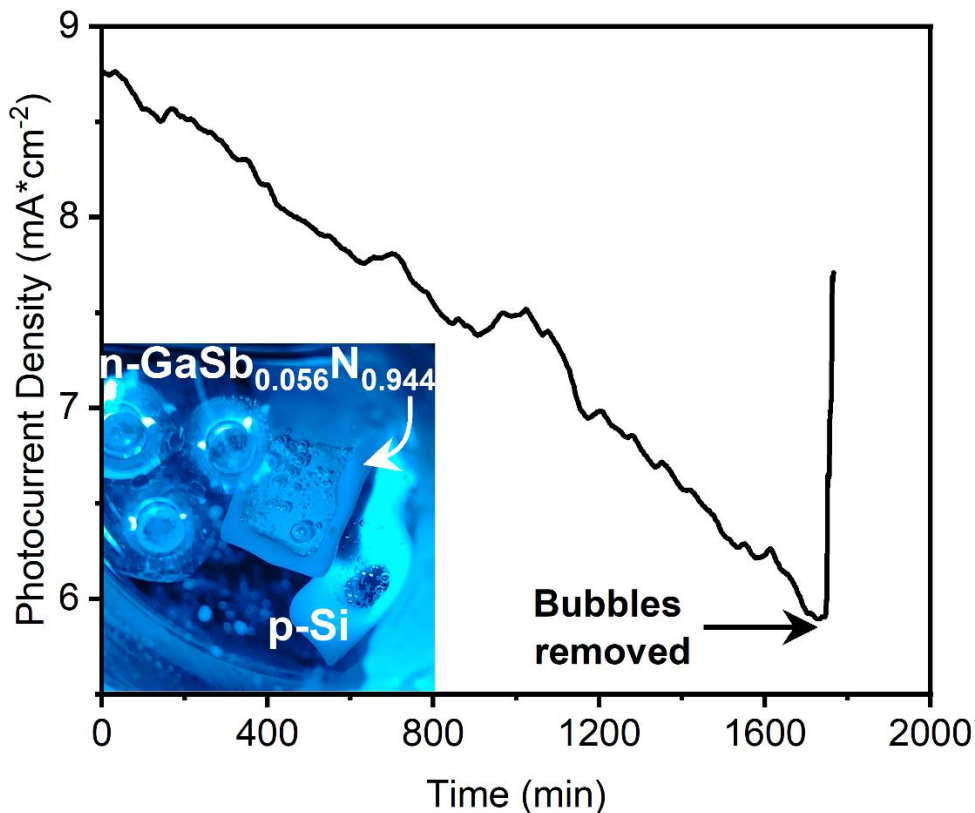


Figure 6.10 Photocurrent density versus time of sample $\text{GaSb}_{0.056}\text{N}_{0.944}$ in a 2-electrode configuration (*p*-Si counter electrode), at 0.5 V vs RHE and 10 sun/470 nm illumination

Figure 6. 11 shows the Scanning Electron Micrographs and X-ray diffraction spectra of sample $\text{GaSb}_{0.056}\text{N}_{0.944}$ before and after stability measurements. A slight smoothening of the surface can be seen in the sample after the 30-hour chronoamperometry measurement (see Figure 6.10) and it is possible this change in morphology is responsible for the decrease in the photocurrent density. However, the alloy shows no signs of degradation according to the X-ray Diffraction spectra that shows only *c*-plane gallium nitride reflections and the right shift of peak (002) is still present in the “after” measurement.

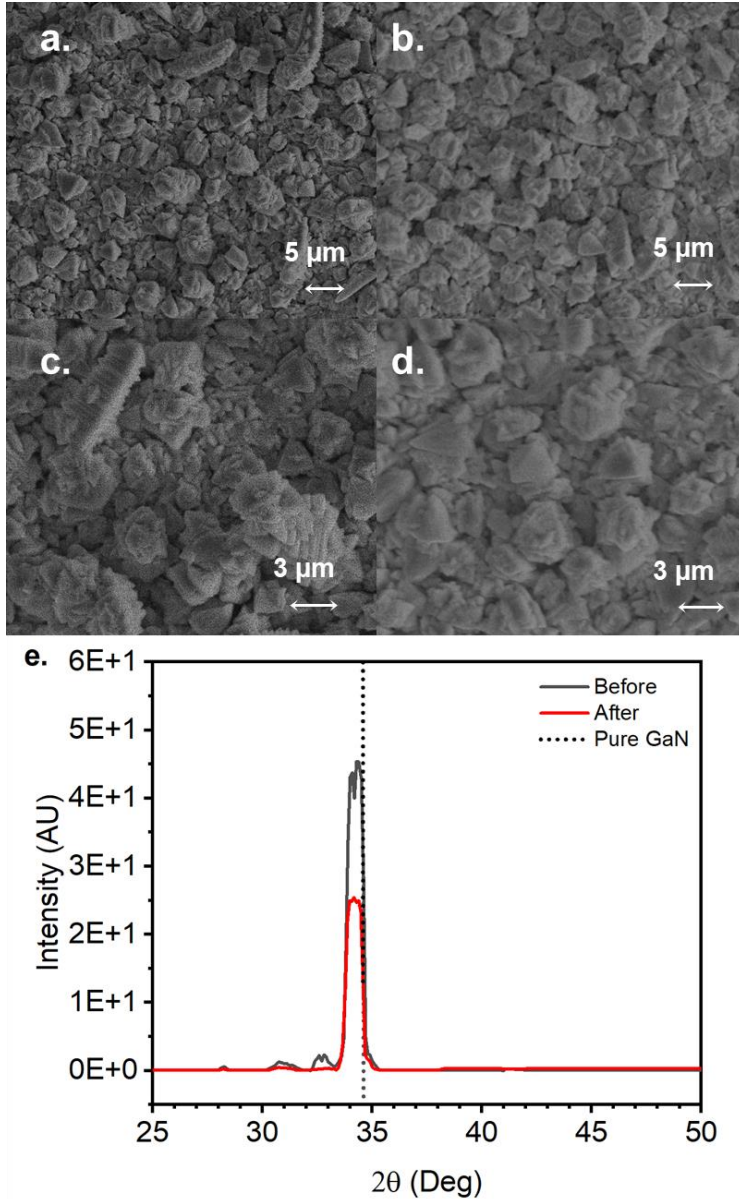


Figure 6. 11 Scanning Electron Micrographs and X-ray diffraction spectra of sample $\text{GaSb}_{0.056}\text{N}_{0.944}$ before (a & c) and after (b & d) stability measurements.

6.4. Summary

For the first time $\text{GaSb}_x\text{N}_{1-x}$ and $\text{GaBi}_y\text{N}_{1-y}$ alloys were synthesized through Plasma-Assisted Vapor Liquid Phase Epitaxy, with alloying degree values, x and y, ranging from 3.4 to 5.6 at% and from 1.0 to 8.8 at%, respectively. Band gap values below and around 2.0 eV were observed for the samples with larger anion substitution.

The synthesized alloys were characterized with Scanning and Transmission Electron Microscopy, X-ray diffraction, Diffuse reflectance and photoelectrochemical techniques. A setup shorting n-GaSb_{0.056}N_{0.944} and p-Si electrodes showed stable photocurrent density at 0.5 V versus RHE reaching values between 6 – 9 mA*cm⁻² for more than 30 hours under 10 sun/470 nm illumination.

7. CHAPTER SEVEN

CONCLUSIONS

The Halide Vapor Phase Epitaxy growth of $\text{GaSb}_z\text{P}_{1-z}$ was successfully modeled with a set of gas and surface phase reactions following the law of mass action formalism, in a cluster of equilibrium and steady state reactors connected in series.

Predicted and experimental growth rates are in good agreement and exhibit similar trends as function of the substrate temperature and system pressure. The growth rate of $\text{GaSb}_z\text{P}_{1-z}$ versus the inverse of the substrate temperature shows two distinctive regions that have been defined in the literature as kinetically and mass transfer limited, at low and high substrate temperatures, respectively.

Additionally, thermodynamic calculations show $\text{GaSb}_z\text{P}_{1-z}$ stability is not favored at temperatures above 850 °C, at a chamber pressure of 500 torr. A decrease in the system pressure lowers the concentrations of all species which are directly proportional to the production rate of $\text{GaSb}_z\text{P}_{1-z}$. HCl , P_2 , and P_4 are the species under supersaturated conditions throughout the studied temperature range and therefore are the ones that determine the growth of $\text{GaSb}_z\text{P}_{1-z}$ on the substrate. SbCl is present in low concentrations but is probably the species responsible for Sb transport, as it is thermodynamically favored particularly at high temperatures. Increasing the substrate temperature is beneficial for the crystalline quality of the $\text{GaSb}_z\text{P}_{1-z}$ films as evidenced in SEM images and XRD measurements showing a preferential orientation towards [111] peak. The antimony content of the films decreased at high substrate temperatures.

The incorporation of antimony in the GaP lattice modifies its light absorption properties as evidenced in the more pronounced slopes of direct Tauc plots of the higher antimony content alloys and it also enhances their performance as photoanodes towards the water splitting reactions, with a lower onset potential and higher fill factor versus the sulfur-doped GaP reference material. Our results also suggest there might be an optimum degree of antimony incorporation given that the alloys with the highest antimony levels show evidence of charge transfer resistance at the interface between the material and the electrolyte.

$\text{GaSb}_x\text{N}_{1-x}$ and $\text{GaBi}_y\text{N}_{1-y}$ dilute alloys with antimony ($0.003 < x < 0.009$) and bismuth ($0.007 < y < 0.011$) fractions were synthesized through Plasma-Assisted Vapor Liquid Phase Epitaxy. The alloy's morphologic, crystallographic, and optical properties were characterized confirming good crystalline quality with preferential (002) orientation of wurtzite structure. No band gap reduction of host material (GaN) was observed through photoluminescence and absorption coefficient estimations, indicating the existence of a band gap reduction discontinuity within the dilute alloying range.

Gold and copper catalyzed PA-VLPE proved to be effective for the growth of high anion-alloyed nitride nanowires for the first time. The synthesized wurtzite nanowires are single crystalline and have band gaps below and around 2.0 eV and therefore are great candidates for solar Water splitting.

Optimization of the growth process are necessary to achieve vertical alignment of $\text{GaSb}_x\text{N}_{1-x}$ and $\text{GaBi}_y\text{N}_{1-y}$ on the substrates. Which will enable a more efficient light absorption and an enhancement of the material's performance in its targeted application.

8. CHAPTER EIGHT

RECOMMENDATIONS

- Both growth tools used in this work need modifications to allow the independent control of competing group-V substitutional anion species.
 - In the HVPE system used to grow $\text{GaSb}_z\text{P}_{1-z}$, this can be accomplished by supplying antimony halide species contained in a bubbler and fed at the entrance of the reactor along phosphorous trichloride.
 - In the PA-VLPE system used to grow $\text{GaSb}_x\text{N}_{1-x}$ and $\text{GaBi}_y\text{N}_{1-y}$ films and wires, a multiple feedthrough setup would allow independent generation and transport of the different species involved, as separate hydrochloric acid flow rates would enable precise control of gallium, antimony/bismuth halide species. Such a setup would also result in a more efficient transport as each precursor discharge can be placed closer to the substrates. A two-zone furnace would also help to control the gallium and substitutional anion species in-situ generation since these metals have different vapor pressures as a function of temperature.
- To enhance $\text{GaSb}_x\text{N}_{1-x}$ and $\text{GaBi}_y\text{N}_{1-y}$ wires light absorption and photoelectrochemical performance it is necessary to either achieve vertical arrays growth or increase the thickness of the nanowire film to fully utilize the absorption depth of these dilute alloys.

REFERENCES

- (1) Sunkara, S. New visible light absorber for solar fuels: Ga(Sbx)N_{1-x} alloys. University of Louisville, Louisville KY, USA, 2015.
- (2) Sunkara, S.; Vendra, V. K.; Jasinski, J. B.; Deutsch, T.; Andriotis, A. N.; Rajan, K.; Menon, M.; Sunkara, M. New Visible Light Absorbing Materials for Solar Fuels, Ga(Sb-x)N_{1-x}. *Advanced Materials* **2014**, 26 (18), 2878-2882. DOI: 10.1002/adma.201305083.
- (3) Martinez-Garcia, A.; Russell, H. B.; Paxton, W. Unassisted water splitting using a GaSbxP_{1-x} photoanode. *Advanced Energy Materials* **2018**, 8 (16), 1703247, Article. DOI: <https://doi.org/10.1002/aenm.201703247>.
- (4) Tsao, J.; Lewis, N.; Crabtree, G. *Solar FAQs*. 2006. <https://www.sandia.gov/app/uploads/sites/153/2022/02/Solar-FAQs.pdf> (accessed 2022 12/06/2022).
- (5) Bard, A. J.; Fox, M. A. ARTIFICIAL PHOTOSYNTHESIS - SOLAR SPLITTING OF WATER TO HYDROGEN AND OXYGEN. *Accounts Chem. Res.* **1995**, 28 (3), 141-145, Review. DOI: 10.1021/ar00051a007.
- (6) Jia, J. Y.; Seitz, L. C.; Benck, J. D.; Huo, Y. J.; Chen, Y. S.; Ng, J. W. D.; Bilir, T.; Harris, J. S.; Jaramillo, T. F. Solar water splitting by photovoltaic-electrolysis with a solar-to-hydrogen efficiency over 30%. *Nature Communications* **2016**, 7, 6, Article. DOI: 10.1038/ncomms13237.
- (7) May, M. M.; Lewerenz, H. J.; Lackner, D.; Dimroth, F.; Hannappel, T. Efficient direct solar-to-hydrogen conversion by in situ interface transformation of a tandem structure. *Nature Communications* **2015**, 6. DOI: 10.1038/ncomms9286.

- (8) Young, J. L.; Steiner, M. A.; Doscher, H. Direct solar-to-hydrogen conversion via inverted metamorphic multi-junction semiconductor architectures. *Nature Energy* **2017**, *2* (4), 17028, Article. DOI: <https://doi.org/10.1038/nenergy.2017.28>.
- (9) Cheng, W. H.; Richter, M. H.; May, M. M.; Ohlmann, J.; Lackner, D.; Dimroth, F.; Hannappel, T.; Atwater, H. A.; Lewerenz, H. J. Monolithic Photoelectrochemical Device for Direct Water Splitting with 19% Efficiency. *Acs Energy Letters* **2018**, *3* (8), 1795-1800. DOI: 10.1021/acseenergylett.8b00920.
- (10) Tournet, J.; Lee, Y.; Krishna, S. K.; Tan, H. H.; Jagadish, C. III-V Semiconductor Materials for Solar Hydrogen Production: Status and Prospects. *Acs Energy Letters* **2020**, *5* (2), 611-622. DOI: 10.1021/acseenergylett.9b02582.
- (11) Deng, J.; Su, Y. D.; Liu, D.; Yang, P. D.; Liu, B.; Liu, C. Nanowire Photoelectrochemistry. *Chemical Reviews* **2019**, *119* (15), 9221-9259, Review. DOI: 10.1021/acs.chemrev.9b00232.
- (12) Masnadi-Shirazi, M.; Beaton, D. A.; Lewis, R. B.; Lu, X. F.; Tiedje, T. Surface reconstructions during growth of GaAs_{1-x}Bi_x alloys by molecular beam epitaxy. *Journal of Crystal Growth* **2012**, *338* (1), 80-84, Article. DOI: 10.1016/j.jcrysgr.2011.09.055.
- (13) Forghani, K.; Anand, A.; Mawst, L. J.; Kuech, T. F. Low temperature growth of GaAs_{1-y}Bi_y epitaxial layers. *Journal of Crystal Growth* **2013**, *380*, 23-27, Article. DOI: 10.1016/j.jcrysgr.2013.05.033.
- (14) Schulte, K. L.; Wood, A. W.; Reedy, R. C.; Ptak, A. J.; Meyer, N. T.; Babcock, S. E.; Kuech, T. F. Heteroepitaxy of GaAs on (001) double right arrow 6 degrees Ge substrates at high growth rates by hydride vapor phase epitaxy. *Journal of Applied Physics* **2013**, *113* (17), 9, Article. DOI: 10.1063/1.4803037.
- (15) Schulte, K. L.; Simon, J.; Roy, A.; Reedy, R. C.; Young, D. L.; Kuech, T. F.; Ptak, A. J. Computational fluid dynamics-aided analysis of a hydride vapor phase epitaxy reactor.

Journal of Crystal Growth **2016**, *434*, 138-147, Article. DOI: 10.1016/j.jcrysgro.2015.10.033.

(16) Novikov, S. V.; Yu, K. M.; Levander, A. X.; Liliental-Weber, Z.; dos Reis, R.; Kent, A. J.; Tseng, A.; Dubon, O. D.; Wu, J.; Denlinger, J.; et al. Molecular beam epitaxy of GaN_{1-x}Bi_x alloys with high bismuth content. *Physica Status Solidi a-Applications and Materials Science* **2012**, *209* (3), 419-423, Article. DOI: 10.1002/pssa.201100312.

(17) Gorji Ghahamestani, S. a. E. M. a. G. B. a. T. C. a. J. J. a. C. P. a. D. K. A. Demonstration of Defect-Free and Composition Tunable GaIn_{1-x}Sb Nanowires. *Nano Letters* **2012**, *12* (9), 4914-4919. DOI: 10.1021/nl302497r. Metaferia, W. a. P. A. R. a. M. K. a. Y. F. a. Z. W. a. Y. A. a. W. R. a. P. M.-E. a. D. K. a. S. L. GaAsP Nanowires Grown by Aerotaxy. *Nano Letters* **2016**, *16* (9), 5701-5707. DOI: 10.1021/acs.nanolett.6b02367 , note = PMID: 27564139. Gagliano, L. a. B. A. a. A. M. a. A. S. a. V. M. A. a. M. L. a. B. F. a. H. J. E. M. Pseudodirect to Direct Compositional Crossover in Wurtzite GaP/In_xGa_{1-x}P Core-Shell Nanowires. *Nano Letters* **2016**, *16* (12), 7930-7936. DOI: 10.1021/acs.nanolett.6b04242.

(18) Jacobsen, H.; Puchala, B.; Kuech, T. F.; Morgan, D. Ab initio study of the strain dependent thermodynamics of Bi doping in GaAs. *Physical Review B* **2012**, *86* (8), 10, Article. DOI: 10.1103/PhysRevB.86.085207.

(19) Capper, P.; Irvine, S.; Joyce, T. *Epitaxial Crystal Growth: Methods and Materials* , *bookTitle= Springer Handbook of Electronic and Photonic Materials*; Springer International Publishing, 2017. DOI: 10.1007/978-3-319-48933-9_14.

(20) Ghasemi, M.; Leshchenko, E. D.; Johansson, J. Assembling your nanowire: an overview of composition tuning in ternary III-V nanowires. *Nanotechnology* **2021**, *32* (7). DOI: 10.1088/1361-6528/abc3e2.

(21) Kitamura, T.; Cho, S. H.; Ishida, Y.; Ide, T.; Shen, X. Q.; Nakanishi, H.; Chichibu, S.; Okumura, H. Growth and characterization of cubic InGa_N epilayers on 3C-SiC by RF

MBE. *Journal of Crystal Growth* **2001**, *227*, 471-475. DOI: 10.1016/s0022-0248(01)00745-x.

(22) Garcia, V. D. C.; Hinojosa, I. E. O.; Echavarria, A. E.; Luna, E. L.; Rodriguez, A. G.; Vidal, M. A. Bulk lattice parameter and band gap of cubic $\text{In}_x\text{Ga}_{1-x}$ (001) alloys on MgO (100) substrates. *Journal of Crystal Growth* **2015**, *418*, 120-125. DOI: 10.1016/j.jcrysgro.2015.02.033.

(23) Farrell, A. C.; Lee, W. J.; Senanayake, P.; Haddad, M. A.; Prikhodko, S. V.; Huffaker, D. L. High-Quality InAsSb Nanowires Grown by Catalyst-Free Selective-Area Metal-Organic Chemical Vapor Deposition. *Nano Letters* **2015**, *15* (10), 6614-6619. DOI: 10.1021/acs.nanolett.5b02389. Du, W. N.; Yang, X. G.; Wang, X. Y.; Pan, H. Y.; Ji, H. M.; Luo, S.; Yang, T.; Wang, Z. G. The self-seeded growth of InAsSb nanowires on silicon by metal-organic vapor phase epitaxy. *Journal of Crystal Growth* **2014**, *396*, 33-37. DOI: 10.1016/j.jcrysgro.2014.03.020. Potts, H.; Friedl, M.; Amaduzzi, F.; Tang, K. C.; Tutuncuoglu, G.; Matteini, F.; Alarcon Llado, E.; McIntyre, P. C.; Morral, A. F. I. From Twinning to Pure Zincblende Catalyst-Free InAs(Sb) Nanowires. *Nano Letters* **2016**, *16* (1), 637-643. DOI: 10.1021/acs.nanolett.5b04367. Mandl, B.; Keplinger, M.; Messing, M. E.; Kriegner, D.; Wallenberg, R.; Samuelson, L.; Bauer, G.; Stangl, J.; Holy, V.; Deppert, K. Self-Seeded Axio-Radial InAs-InAs_{1-x}P_x Nanowire Heterostructures beyond "Common" VLS Growth. *Nano Letters* **2018**, *18* (1), 144-151. DOI: 10.1021/acs.nanolett.7b03668. Isakov, I.; Panfilova, M.; Sourribes, M. J. L.; Tileli, V.; Porter, A. E.; Warburton, P. A. InAs_{1-x}P_x nanowires grown by catalyst-free molecular-beam epitaxy. *Nanotechnology* **2013**, *24* (8). DOI: 10.1088/0957-4484/24/8/085707. Ren, D. K.; Farrell, A. C.; Williams, B. S.; Huffaker, D. L. Seeding layer assisted selective-area growth of As-rich InAsP nanowires on InP substrates. *Nanoscale* **2017**, *9* (24), 8220-8228. DOI: 10.1039/c7nr00948h.

- (24) Kauko, H.; Fimland, B. O.; Grieb, T.; Munshi, A. M.; Muller, K.; Rosenauer, A.; van Helvoort, A. T. J. Near-surface depletion of antimony during the growth of GaAsSb and GaAs/GaAsSb nanowires. *Journal of Applied Physics* **2014**, *116* (14). DOI: 10.1063/1.4896904. Zhou, C.; Zheng, K.; Chen, P. P.; Matsumura, S.; Lu, W.; Zou, J. Crystal-phase control of GaAs-GaAsSb core-shell/axial nanowire heterostructures by a two-step growth method. *Journal of Materials Chemistry C* **2018**, *6* (25), 6726-6732. DOI: 10.1039/c8tc01529e. Harmand, J. C.; Glas, F.; Patriarche, G. Growth kinetics of a single InP_{1-x}As_x nanowire. *Physical Review B* **2010**, *81* (23). DOI: 10.1103/PhysRevB.81.235436. Zhang, Y. Y.; Sanchez, A. M.; Sun, Y.; Wu, J.; Aagesen, M.; Huo, S. G.; Kim, D.; Jurczak, P.; Xu, X. L.; Liu, H. Y. Influence of Droplet Size on the Growth of Self-Catalyzed Ternary GaAsP Nanowires. *Nano Letters* **2016**, *16* (2), 1237-1243. DOI: 10.1021/acs.nanolett.5b04554. Ngo, C.; Zhou, H. L.; Mecklenburg, M.; Pozuelo, M.; Regan, B. C.; Xiao, Q. F.; Shenoy, V. B.; Hicks, R. F.; Kodambaka, S. Effect of precursor flux on compositional evolution in InP_{1-x}Sb_x nanowires grown via self-catalyzed vapor-liquid-solid process. *Journal of Crystal Growth* **2011**, *336* (1), 14-19. DOI: 10.1016/j.jcrysgro.2011.09.043.
- (25) Jain, S. C.; Willander, M.; Narayan, J.; Van Overstraeten, R. III-nitrides: Growth, characterization, and properties. *Journal of Applied Physics* **2000**, *87* (3), 965-1006. DOI: 10.1063/1.371971.
- (26) Yu, W. Y.; Wang, J.; Luo, Y.; Zhang, Z. X.; Li, X.; Yu, J. D.; Wang, L.; Hao, Z. B.; Sun, C. Z.; Han, Y. J.; et al. Spatial distribution study of a nitrogen plasma in an ion-filtered inductively coupled plasma used to grow GaN films. *Journal of Physics D-Applied Physics* **2019**, *52* (39). DOI: 10.1088/1361-6463/ab2ea3.
- (27) Sakakita, H.; Kumagai, N.; Shimizu, T.; Kim, J.; Yamada, H.; Wang, X. L. Ammonia-free epitaxy of single-crystal InN using a plasma-integrated gas-injection module. *Applied Materials Today* **2022**, *27*. DOI: 10.1016/j.apmt.2022.101489.

- (28) Yu, K. M.; Novikov, S. V.; Ting, M.; Sarney, W. L.; Svensson, S. P.; Shaw, M.; Martin, R. W.; Walukiewicz, W.; Foxon, C. T. Growth and characterization of highly mismatched GaN_{1-x}Sbx alloys. *Journal of Applied Physics* **2014**, *116* (12). DOI: 10.1063/1.4896364.
- (29) Chowdhury, F. A.; Sadaf, S. M.; Shi, Q.; Chen, Y. C.; Guo, H.; Mi, Z. Optically active dilute-antimonide III-nitride nanostructures for optoelectronic devices. *Applied Physics Letters* **2017**, *111* (6). DOI: 10.1063/1.4997450.
- (30) Calero-Barney, S. J.; Andriotis, A. N.; Menon, M.; Sunkara, M. Plasma-assisted vapor liquid phase epitaxial growth of dilute GaSbxN_{1-x} and GaBi_yN_{1-y} alloys: Confirmation of band gap reduction discontinuity. *Physical Review B* **2022**, *105* (8). DOI: 10.1103/PhysRevB.105.085307.
- (31) Shaw, M.; Yu, K. M.; Ting, M.; Powell, R. E. L.; Sarney, W. L.; Svensson, S. P.; Kent, A. J.; Walukiewicz, W.; Foxon, C. T.; Novikov, S. V.; et al. Composition and optical properties of dilute-Sb GaN_{1-x}Sbx highly mismatched alloys grown by MBE. *Journal of Physics D-Applied Physics* **2014**, *47* (46). DOI: 10.1088/0022-3727/47/46/465102.
- (32) Simon, J.; Young, D.; Ptak, A.; Ieee. Low-Cost III-V Solar Cells Grown by Hydride Vapor-Phase Epitaxy. *2014 Ieee 40th Photovoltaic Specialist Conference (Pvsc)* **2014**, 538-541, Proceedings Paper.
- (33) Schulte, K. L.; Simon, J.; Roy, A. Computational fluid dynamics-aided analysis of a hydride vapor phase epitaxy reactor. *Journal of Crystal Growth* **2016**, *434* (15), 138-147, Article. DOI: <https://doi.org/10.1016/j.jcrysgro.2015.10.033>.
- (34) Simon, J.; Young, D.; Ptak, A. Low-cost III-V solar cells grown by hydride vapor-phase epitaxy. *2014 Ieee 40th Photovoltaic Specialist Conference (Pvsc)* **2014**, 538-541, Article. DOI: <https://doi.org/10.1109/PVSC.2014.6924977>.
- (35) Ward, J. S.; Remo, T.; Horowitz, K.; Woodhouse, M.; Sopori, B.; VanSant, K.; Basore, P. Techno-economic analysis of three different substrate removal and reuse strategies for

III-V solar cells. *Progress in Photovoltaics* **2016**, 24 (9), 1284-1292, Article. DOI: 10.1002/pip.2776.

(36) Oda, O.; Hori, M. Novel Epitaxy for Nitride Semiconductors Using Plasma Technology. *Physica Status Solidi a-Applications and Materials Science* **2021**, 218 (1). DOI: 10.1002/pssa.202000462.

(37) Ban, V. S. Mass spectrometric and thermodynamic studies of the CVD of some III-V compounds. *J. Cryst. Growth* **1972**, 17 (12), 19-23, Article. DOI: [https://doi.org/10.1016/0022-0248\(72\)90227-8](https://doi.org/10.1016/0022-0248(72)90227-8).

(38) Hong, J. C.; Lee, H. H. Epitaxial-growth rate of GaAs: chloride transport process. *J. Electrochem. Soc.* **1985**, 132 (2), 427-432, Article. DOI: <https://doi.org/10.1149/1.2113858>.

(39) Mimila-Arroyo, J.; Diaz-Reyes, J. Modeling halogen chemical vapor deposition for III-V semiconductor compounds. *J. Cryst. Growth* **2001**, 225 (1), 50-58, Article. DOI: [https://doi.org/10.1016/S0022-0248\(01\)01032-6](https://doi.org/10.1016/S0022-0248(01)01032-6).

(40) Hollan, L.; Durand, J. M.; Cadoret, R. Influence of growth parameters in GaAs vapor-phase epitaxy. *J. Electrochem. Soc.* **1977**, 124 (1), 135-139, Article. DOI: <https://doi.org/10.1149/1.2133227>.

(41) Veuhoff, E.; Putz, N.; Korec, J. Modeling of GaAs growth in the low-pressure halide transport-system. *J. Electron. Mater.* **1983**, 12 (2), 235-246, Article. DOI: <https://doi.org/10.1007/bf02651131>.

(42) Shaw, D. W. Kinetic aspects in the vapour phase epitaxy of III-V compounds. *J. Cryst. Growth* **1975**, 31 (12), 130-141, Article. DOI: [https://doi.org/10.1016/0022-0248\(75\)90122-0](https://doi.org/10.1016/0022-0248(75)90122-0).

(43) Mizuno, O.; Watanabe, H. Vapor growth kinetics of III-V compounds in a hydrogen inert gas mixed carrier system. *J. Cryst. Growth* **1975**, 30 (2), 240-248, Article. DOI: [https://doi.org/10.1016/0022-0248\(75\)90095-0](https://doi.org/10.1016/0022-0248(75)90095-0).

- (44) Korec, J.; Heyen, M. Modeling of chemical vapor deposition: II. Gas phase epitaxy of (100) GaAs. *J. Cryst. Growth* **1982**, *60* (2), 297-306, Article. DOI: [https://doi.org/10.1016/0022-0248\(82\)90102-6](https://doi.org/10.1016/0022-0248(82)90102-6). Heyen, M.; Balk, P. Epitaxial growth of GaAs in chloride transport systems. *Prog. Cryst. Growth Charact. Mater.* **1983**, *6* (3), 265-303, Review. DOI: [https://doi.org/10.1016/0146-3535\(83\)90043-6](https://doi.org/10.1016/0146-3535(83)90043-6).
- (45) Kirwan, D. J. Reaction equilibria in the growth of GaAs and GaP by the chloride transport process. *J. Electrochem. Soc.* **1970**, *117* (12), 1572-1577, Article. DOI: <https://doi.org/10.1149/1.2407387>.
- (46) Kuniya, Y.; Hosaka, M. Vapor-phase equilibria in systems In-InCl₃ and Ga-GaCl₃. *J. Cryst. Growth* **1975**, *28* (3), 385-391, Article. DOI: [https://doi.org/10.1016/0022-0248\(75\)90077-9](https://doi.org/10.1016/0022-0248(75)90077-9).
- (47) Manion, J. A.; Huie, R. E.; Levin, R. D.; Burgess Jr., D. R.; Orkin, V. L.; Tsang, W.; McGivern, W. S.; Hudgens, J. W.; Knyazev, V. D.; Atkinson, D. B.; et al. *NIST Chemical Kinetics Database*. National Institute of Standards and Technology, <http://kinetics.nist.gov/> (accessed).
- (48) Hirako, A.; Kusakabe, K.; Ohkawa, K. Modeling of reaction pathways of GaN growth by metalorganic vapor-phase epitaxy using TMGa/NH₃/H₂ system: A computational fluid dynamics simulation study. *Japanese Journal of Applied Physics* **2005**, *44* (2), 874-879, Article. DOI: <https://doi.org/10.1143/JJAP.44.874>.
- (49) Bleicher, M. Thermodynamic calculations for GaAs_{1-x}P_x vapor growth. *J. Electrochem. Soc.* **1972**, *119* (5), 613-617, Article. DOI: <https://doi.org/10.1149/1.2404272>.
- (50) Downs, A. J.; Pulham, C. R. The hydrides of aluminum, gallium, indium, and thallium: a re-evaluation. *Chemical Society Reviews* **1994**, *23* (3), 175-184, Review. DOI: <https://doi.org/10.1039/CS9942300175>.

- (51) Klima, P.; Silhavy, J.; Rerabek, V. Study of equilibrium reactions in Ga-PCl₃-H₂ and Ga-AsCl₃-H₂ epitaxial systems. *J. Cryst. Growth* **1976**, *32* (3), 279-286, Article. DOI: [https://doi.org/10.1016/0022-0248\(76\)90108-1](https://doi.org/10.1016/0022-0248(76)90108-1).
- (52) Ferguson, R. R.; Gabor, T. The transport of gallium arsenide in the vapor phase by chemical reaction. *J. Electrochem. Soc.* **1964**, *111* (5), 585-592, Article. DOI: <https://doi.org/10.1149/1.2426188>.
- (53) Chatillon, C.; Bernard, C. Thermodynamic calculations in CVD growth of GaAs compounds 1. Critical-assessment of the thermodynamic properties for the gaseous molecules of the Ga-Cl system. *J. Cryst. Growth* **1985**, *71* (2), 433-449, Article. DOI: [https://doi.org/10.1016/0022-0248\(85\)90103-4](https://doi.org/10.1016/0022-0248(85)90103-4).
- (54) Bernard, C.; Chatillon, C.; Aithou, A. Thermodynamics of (gallium + chlorine) (G). 1. Vapor-pressure measurements and thermodynamic stability of gacl(G), gacl₂(G), gacl₃(G), ga₂cl₂(G), ga₂cl₄(G), and ga₂cl₆(G). *J. Chem. Thermodyn.* **1988**, *20* (2), 129-141, Article. DOI: [https://doi.org/10.1016/0021-9614\(88\)90148-6](https://doi.org/10.1016/0021-9614(88)90148-6).
- (55) Seki, H.; Araki, H. Vapor transport thermodynamics of GaP-Cl₂-H₂ system in an open tube. *Japanese Journal of Applied Physics* **1967**, *6* (12), 1414-1418, Article. DOI: <https://doi.org/10.1143/JJAP.6.1414>.
- (56) Calero-Barney, S. J.; Paxton, W.; Ortiz, P.; Sunkara, M. K. Gallium antimonide phosphide growth using Halide Vapor Phase Epitaxy. *Solar Energy Materials and Solar Cells* **2020**, *209*, 9, Article. DOI: 10.1016/j.solmat.2020.110440.
- (57) Chen, Z.; Dinh, H. N. *Photoelectrochemical Water Splitting: Standards, Experimental Methods, and Protocols*; Springer-Verlag, 2013.
- (58) Schefold, J. Impedance and intensity modulated photocurrent spectroscopy as complementary differential methods in photoelectrochemistry. *Journal of Electroanalytical Chemistry* **1992**, *341* (1-2), 111-136, Article. DOI: [https://doi.org/10.1016/0022-0728\(92\)80479-N](https://doi.org/10.1016/0022-0728(92)80479-N). Klahr, B.; Gimenez, S.; Fabregat-Santiago, F. Water oxidation at

hematite photoelectrodes: the role of surface states. *Journal of the American Chemical Society* **2012**, *134* (9), 4294-4302, Article. DOI: <https://doi.org/10.1021/ja210755h>.

(59) Belabbes, A.; Ferhat, M.; Zaoui, A. Giant and composition-dependent optical band gap bowing in dilute GaSb_{1-x}N_x alloys. *Applied Physics Letters* **2006**, *88* (15). DOI: 10.1063/1.2196049.

(60) Sheetz, R. M.; Richter, E.; Andriotis, A. N.; Lisenkov, S.; Pendyala, C.; Sunkara, M. K.; Menon, M. Visible-light absorption and large band-gap bowing of GaN_{1-x}Sb_x from first principles. *Physical Review B* **2011**, *84* (7). DOI: 10.1103/PhysRevB.84.075304.

(61) Andriotis, N. A.; Sheetz, R. M.; Ernst, R.; Madhu, M. Band alignment and optical absorption in Ga(Sb)N alloys. *Journal of Physics: Condensed Matter* **2014**, *26* (5), 055013.

(62) Kuech, T. F.; Babcock, S. E.; Mawst, L. Growth far from equilibrium: Examples from III-V semiconductors. *Appl. Phys. Rev.* **2016**, *3* (4), 12, Review. DOI: 10.1063/1.4944801.

(63) Jaramillo-Cabanzo, D. F.; Jasinski, J. B.; Sunkara, M. K. Liquid Phase Epitaxy of Gallium Nitride. *Crystal Growth & Design* **2019**, *19* (11), 6577-6585. DOI: 10.1021/acs.cgd.9b01011.

(64) Kumari, S.; Ajayi, B. P.; Kumar, B. A low-noble-metal W_{1-x}Ir_xO_{3-d} water oxidation electrocatalyst for acidic media via rapid plasma synthesis. *Energy & Environmental Science* **2017**, *10* (11), 2432-2440, Article. DOI: <https://doi.org/10.1039/C7EE02626A>.

CURRICULUM VITAE

Sonia J Calero-Barney
Louisville KY. Ph. (305) 684-5946
sjcale01@louisville.edu [linkedin.com/in/sonia-calero-barney-a810b726](https://www.linkedin.com/in/sonia-calero-barney-a810b726)

Education

University of Louisville, PhD in Chemical Engineering, Summer 2022
Dissertation title: "Anion alloying of III-V semiconductors for Water Splitting"
Universidad de los Andes, MSc in Chemical Engineering, March 2014.
Universidad del Valle, BSc in Chemical Engineering, April 2010.

Research and Professional Experience

Graduate Fellow, Conn Center for Renewable Energy Research, University of Louisville, Louisville KY, Aug. 2019 – present

- Performed troubleshooting, maintenance, and modification of custom-built vacuum systems for crystal growth, including leak checking, selection and installation of Swagelok and VCR fittings, mass flow controllers, pressure gauges and pressure control valves, mechanical pumps, thermocouples, etc.
- Designed and conducted experiments for the growth of III-V semiconductor films such as GaP and GaN, with substitution of V-group elements, i.e., antimony or bismuth to produce ternary alloys ($\text{GaV}_x\text{N}_{1-x}$ and $\text{GaV}_y\text{P}_{1-y}$). These materials have great potential in solar energy conversion technologies (multi-junction solar cells and renewable hydrogen production).
- Developed models to predict gas-phase compositions, phase stability and growth rates of III-V alloys grown using halide and nitrogen plasma chemistries. This required compilation and estimation of thermochemical data sometimes non-existent in literature, particularly for novel $\text{GaV}_x\text{N}_{1-x}$ and $\text{GaV}_y\text{P}_{1-y}$ alloys.
- Correlated processing conditions with optical, crystallographic, morphological, and photo-electrochemical properties of III-V alloys which helped to determine processing condition that optimized material's properties.
- Trained new students from high school to graduate levels, in the usage of synthesis and characterization equipment as well as laboratory safety procedures. Developed Standard Operating Procedures for vacuum systems and Raman spectrometer.

R&D Packaging Engineer, Johnson & Johnson, Cali Colombia, Mar. 2014 – Dec. 2015

- Developed Change Control Plans for new packaging materials and suppliers. Involvement in projects with up to 500K USD savings per year.
- Designed qualifying plans to evaluate the performance of new packaging materials (rigid, flexible, paper-based) in filling lines, storage, transportation, and end-use.
- Collaborated with packaging materials suppliers to modify materials specifications with inclusion of additional attributes, variables, or acceptable quality limits to meet demands of internal J&J customers.
- Provided technical support in product filling lines to troubleshoot issues involving PET bottles, PP caps, labels, wrappers, folding boxes, corrugated shippers, polybags, tapes, and stickers, with the aid of statistical data analysis and problem-solving techniques to identify root causes. Overall Operation Effectiveness improved by 29.7% in automated corrugated filling machines and 9.2% in automated folding box filling lines.

Intern, Hawaii Natural Energy Institute, University of Hawaii at Manoa, Honolulu HI, Summer 2013

Synthesized zinc oxysulfide thin films by sputtering. Evaluated their optoelectronic properties for use in solar cells, as an alternative to cadmium sulfide films.

Graduate Research Assistant, Department of Chemical Engineering, Universidad de los Andes, Bogota Colombia, 2012 - 2013

Evaluated the effect of electrochemical proton intercalation on the photoelectrochemical performance of tungsten trioxide thin films and developed a method for morphological characterization of these films (porosity and surface area), based on the intercalation phenomenon.

Selected Publications

- **S. J. Calero-Barney**, A. N. Andriotis, M. Menon, M. K. Sunkara, "III-Nitride Alloy Nanowires Synthesized Through Plasma-Assisted Vapor Liquid Solid Growth", In preparation.
- **S. J. Calero-Barney**, A. N. Andriotis, M. Menon, M. K. Sunkara, "Plasma-Assisted Vapor Liquid Phase Epitaxy of dilute GaSbxN1-x and GaBiyN1-y alloys: confirmation of band gap reduction discontinuity," *Physical Review B* 105 (8), 085307, 2022
- **S. J. Calero-Barney**, W. Paxton, P. Ortiz, and M. K. Sunkara, "Gallium antimonide phosphide growth using Halide Vapor Phase Epitaxy," *Solar Energy Materials and Solar Cells*, Article vol. 209, p. 9, Jun 2020, Art no. 110440.
- Martinez-Garcia, H. B. Russell, W. Paxton, S. Ravipati, **S. Calero-Barney**, M. Menon, E. Richter, J. Young, T. Deutsch, M. K. Sunkara, "Unassisted water splitting using a GaSbxP1-x photoanode," *Advanced Energy Materials*, Article vol. 8, no. 16, p. 1703247, 2018.
- **S. J. Calero**, P. Ortiz, A. F. Onate, and M. T. Cortes, "Effect of proton intercalation on photo-activity of WO3 anodes for water splitting," *International Journal of Hydrogen Energy*, vol. 41, no. 9, pp. 4922-4930, Mar 2016.

Conference Presentations

- **S. Calero-Barney** and M. K. Sunkara, "Low-Cost Synthesis Methods for Single Crystal Quality III-V Alloys", MRS Spring Meeting, Honolulu, HI, May 8th – 13th 2022.
- **S. Calero-Barney** and M. K. Sunkara, "Halide Vapor Phase Epitaxy of III-V Semiconductors on Silicon Substrates", *AIChE Annual Meeting*, Orlando, FL, Nov. 10th - 15th 2019.
- **M. K. Sunkara**, H. Paxton, S. Calero-Barney, M. Menon, J. Young, and T. Deutsch, "Novel band-gap engineered III-V Alloys for Unassisted Water Photoelectrolysis," E. M. R. S. t. meeting, Ed., Nice, France, May 27th - 31st 2019.
- **M. K. Sunkara** and S. Calero, "Novel Band-Gap Engineered III-V Alloys for Unassisted Water Photoelectrolysis," in *233rd ECS meeting*, Seattle, WA, May 13th - 17th 2018.
- **S. Calero-Barney** and M. K. Sunkara, "Anion alloying of III-V semiconductors for renewable energy," *2021 AIChE Annual Meeting*, Boston, MA, Nov. 5th - 18th 2021 (Poster).
- **S. Calero-Barney et al.**, "Novel Band-Gap Engineered III-V Alloys for Unassisted Water Photoelectrolysis" in *231st ECS Meeting*, New Orleans, LA, 2017 (Poster).

Leadership and Professional Affiliations

- Since 2021, member of the American Institute of Chemical Engineers, AIChE.
- Since 2017, Graduate Student Representative, Student Affairs Committee, J. B. Speed School of Engineering, University of Louisville.
- Since 2016, peer reviewer for different journals including Scientific Reports, Journal of Materials Science and Colloids and Surfaces a-Physicochemical and Engineering Aspects. Publons profile ([Sonia Juliana Calero Barney | Publons](#)).

Honors and Awards

Winner and people's choice, Three Minute Thesis Competition (3MT), University of Louisville, Spring 2022.

Graduate Fellowship, Conn Center for Renewable Energy Research, 2019, 2010, 2021 & 2022.

Relevant coursework

Hands on Photovoltaic Experience at *NREL* (2018), Synergy of Experimental and Numerical Studies for Crystal Growth of Bulk Semiconductors at *Leibniz-Institut für Kristallzüchtung* (2020), Physical Electronics at *UofL* (2017), Materials Characterization at *UofL* (2018), Chemical Vapor Deposition at *UofL* (2017).

Relevant skills

Design of Experiments, Systematic Literature Review, Statistical Analysis, Matlab, Chemkin, Comsol, Origin Pro, MOCVD, Plasma-Assisted CVD, Halide Vapor Phase Epitaxy, Liquid Phase Epitaxy, Thermal Evaporation, Sputtering, Optical Emission Spectroscopy, Uv-Vis Spectroscopy, Scanning Electron Microscopy (SEM), X-ray Diffraction (XRD), DiffracEva, Raman and Photoluminescence Spectroscopy, Electrochemistry, Laboratory Safety and Waste Management.